Negative ion production in low temperature hydrogen plasmas

Gregory James Smith

Doctor of Philosophy

University of York

Physics

April 2021

Abstract

The production of negative ions in low temperature plasmas presents significant opportunities and challenges for technological applications and fundamental plasma physics. Negative hydrogen ions are of particular interest for applications including materials surface processing, mass spectrometry, and neutral beams. Negative ions in hydrogen plasma are produced via both volume and surface processes. The surface production of negative ions in hydrogen plasmas is important for the development of next-generation neutral beam heating systems, and in particular for decreasing the reliance on caesium. To address this challenge, the production of negative ions using doped diamond is investigated. Continuously and pulsed bias (-20 V or -130 V at 5 kHz), nitrogen doped micro-crystalline diamond films are introduced to a low pressure deuterium plasma (2 Pa, 26 W or 2 Pa, 130 W) and negative ion energy distribution functions are measured via mass spectrometry with respect to the surface temperature (30°C to 750°C) and dopant concentration. The results show that the use of nitrogen doping can enhance negative ion yield from diamond above that observed under similar conditions for un-doped diamond. A relatively low yield is observed using a pulsed bias compared to a dc bias, which suggests that a certain ratio of defects to preserved diamond bonds on the films can promote optimum conditions for negative ion formation. The volume production of negative ions is investigated in the context of inductively coupled plasmas, which for high power densities - and surface fluxes - are subject to significant spatial gradients in the neutral gas temperature and density. To meet this challenge, we build upon established simulation work in the context of low power density capacitively coupled plasmas to simulate negative ion production via 2D fluid-kinetic simulations with the Hybrid Plasma Equipment Model, which enables self-consistent calculation of gas heating for all of the vibrational levels of the ground electronic state. The simulations, which show good agreement with previously published experimental data (6-20 Pa, 300 W), are used to investigate the impact of gradients on the macroscopic plasma properties and the negative ion production. The results demonstrate that when thermal gradients are present in the plasma, atomic hydrogen and the vibrational states diffuse down the gradients, affecting their distribution within the plasma. However, it is observed that thermal gradients have only a small influence on negative ion density despite observed changes in the densities of the vibrational states in the bulk of the plasma. The results of this work are expected to be of interest for the fundamental understanding of low-temperature hydrogen plasmas and the development of negative ion sources.

Publications and conferences

This thesis has resulted in a number of publications in peer reviewed journals, as listed below. Some of the results presented in the chapter have been adapted from the material in these publications.

G. J. Smith, J. Ellis, R. Moussaoui, C. Pardanaud, C. Martin, J. Achard, R. Issaoui, T Gans, J. P. Dedrick, G. Cartry, *Enhancing surface production of negative ions using nitrogen doped diamond in a deuterium plasma* Journal of Physics D: Applied Physics **53** (2020) 465204 doi:10.1088/1361-6463/aba6b6

G. J. Smith, L. Tahri, J. Achard, R. Issaoui, T. Gans, J. P. Dedrick, G. Cartry, *Surface production of negative ions from pulse-biased nitrogen dopeddiamond within a low-pressure deuterium plasma* Journal of Physics D: Applied Physics (In review)

G. J. Smith, J. Ellis, T. Gans, J. Dedrick, J. Achard, R. Issaoui, S. Doyle, A. Gibson, P. Diomede, M. Kushner, L. Tahri, R. Moussoui, C. Paranaud, C. Martin, G. Cartry *Increasing the surface production of negative ions from nitrogen doped diamond in low pressure hydrogen plasmas*, Oral presentation at the Gaseous Electronics Conference, Virtual conference (2020)

G. J. Smith, J. Ellis, R. Moussoui, C. Paranaud, J. Achard, R. Issaoui, T. Gans, J. Dedrick, G. Cartry *Surface production of negative ions from nitrogen doped diamond in a deuterium plasma* Oral presentation at the Gaseous Electronics Conference, College Station (2019)

G. J. Smith, J. Ellis, R. Moussaoui, C. Paranaud, J. Achard, R. Issaoui, T. Gans, J. P. Dedrick, G. Cartry *Surface production of negative ions from nitrogen doped diamond in a deuterium plasma*, Poster prize winner at the Technological Plasma Workshop, Coventry (2018)

Contents

List of Tables

List of Figures

Acknowledgements

The work contained within this thesis, and the thesis itself, would not have been possible without the support of numerous individuals and groups from around the globe. It is difficult for me to comprehend how many hours people have spent supporting me during the completion of this PhD; whether that is in helping me to fix issues, teaching me concepts or techniques, assisting me with papers and presentations or just being available to chat about things. I don't think that just naming them here truly acknowledges how grateful I am, but I hope this gesture is a start.

I would like to first acknowledge Scott Doyle who wrote the python script Helena that has grown up with me these past few years, as well as providing uncountable bits of advice and support throughout the PhD. Secondly, I must thank my supervisor James Dedrick. He has spent too many late nights reading things I have sent him and multiple long afternoons chatting about my projects, I'm very grateful for the support and guidance he has given me the past 4 years. I also need to thank Timo Gans for numerous meetings and discussions about my project that never failed to further my progress. One of the topics in this thesis involved an international collaboration with Gilles Cartry from the PIIM group in Marseille. I am incredibly grateful of his support whilst I was in Marseille, and for him helping me feel part of the group whilst there.

I would like to thank the PhD students of the YPI, particularly those in my CDT cohort and the LTP group, especially Phil for putting up with my constant coffee break requests. The support of the YPI staff has been greatly appreciated over these past few years for being both great at their jobs and for being some of the friendliest people you can come across. The technical support of the YPI IT and laboratory staff is also greatly appreciated. I was not the ideal project student when it came to hardware and software, and I am grateful for their support in fixing both my understanding of technical concepts or my mistakes made when using equipment or IT systems.

Almost every aspect of this PhD involved feedback and support from an international group of people. By the end of the PhD, in a meeting with 7 people, no two were currently in the same country, which I think speaks volumes about the nature of research in the low

temperature plasma community. I would like to thank, Paola Diomede, Andrew Gibson, Vasco Guerra and Mark Kushner for providing me with numerous hours of feedback and assistance with my projects and with whom I hope to continue working with for as long as I am able to. I would also like to thank members of the PIIM group including: Cédric Paranaud, Céline Martin, Lenny Tahri, and Roba Moussaoui, as well as the input from Riadh Issaoui and Jocelyn Achard from LSPM.

Finally, I need to thank my friends and family. In particular I need to thank the York City Ultimate team, for helping me blow off steam and hurl a frisbee around without judgement, Tom Nicol for being the best spontaneous flat mate decision a guy can make, Richard as he is like a brother to me, Byron who may as well be a brother to me, my parents for being brave enough to ask how things are going and Heidi, for making me a better human bean.

Declaration

This thesis has not previously been accepted for any degree and is not being concurrently submitted in candidature for any degree other than Doctor of Philosophy of the University of York. This thesis is the result of my own investigations, except where otherwise stated. All other sources are acknowledged by explicit references.

A subset of this work discussed in this thesis has been presented at scientific conferences and has been, or will be, published in peer-reviewed journals. Full details of all prior published and presented work are listed in section the section titled Publications and conferences.

Numerical simulations using the hybrid plasma equipment model (HPEM) were set-up, run and analysed by the author. Permission to use HPEM was given by the creator of the code, Prof. Mark Kushner of the University of Michigan, US. Experiments were carried out by the author at the University of Marseille within the PIIM group, as supervised by Prof. Gilles Cartry. Raman measurements were carried out at the University of Marseille with the assistance of Dr. Cedric Paranaud and confocal measurements were provided by Prof. Celine Martin. Analysis and interpretation of these results was undertaken by the author.

The work presented herein was funded by the Engineering and Physical Sciences Research Council (EPSRC), grant reference number EP/L01663X/1.

Chapter 1

Introduction

This thesis was motivated by a desire to develop the understanding of negative ion production in low temperature hydrogen plasmas. Current challenges in the field include the development of new materials for enhancing the surface production of negative ions, and show how spatial gradients in the charged and neutral species can impact upon macroscopically observed plasma behaviour.

The introduction to this thesis is laid out so as to introduce the "surface" and "volume" challenges sequentially. The low temperature plasma state, with a focus on electronegative plasmas and hydrogen, is introduced in section 1.1. After this, the process of surface production of negative ions from metals and dielectrics is described in section 1.2 and a current challenge in the context of negative ion sources for magnetically confined fusion is explained. In section 1.3, the physics of volume production is introduced, followed by an explanation of current challenges and a path to addressing these. An overview of the thesis is given in section 1.4.

1.1 The low temperature plasma state

The plasma state is described as an ionized gas containing freely and randomly moving electrons and ions[1]. For this work a particular type of plasma, referred to as low temperature plasma, is considered. The use of the term low temperature refers to the fact that the electrons are not in thermal equilibrium with ions and neutrals, where electrons have energies of a few eV while ions and neutrals have an energy a factor 100 lower than this[1,2]. Typically, low temperature plasmas have a relatively small density of ions and electrons compared to the density of neutral species, with an ionisation fraction of less than 1%. The vast parameter space of electron temperature and density characteristic of natural and man-made plasmas is shown in figure 1.1.

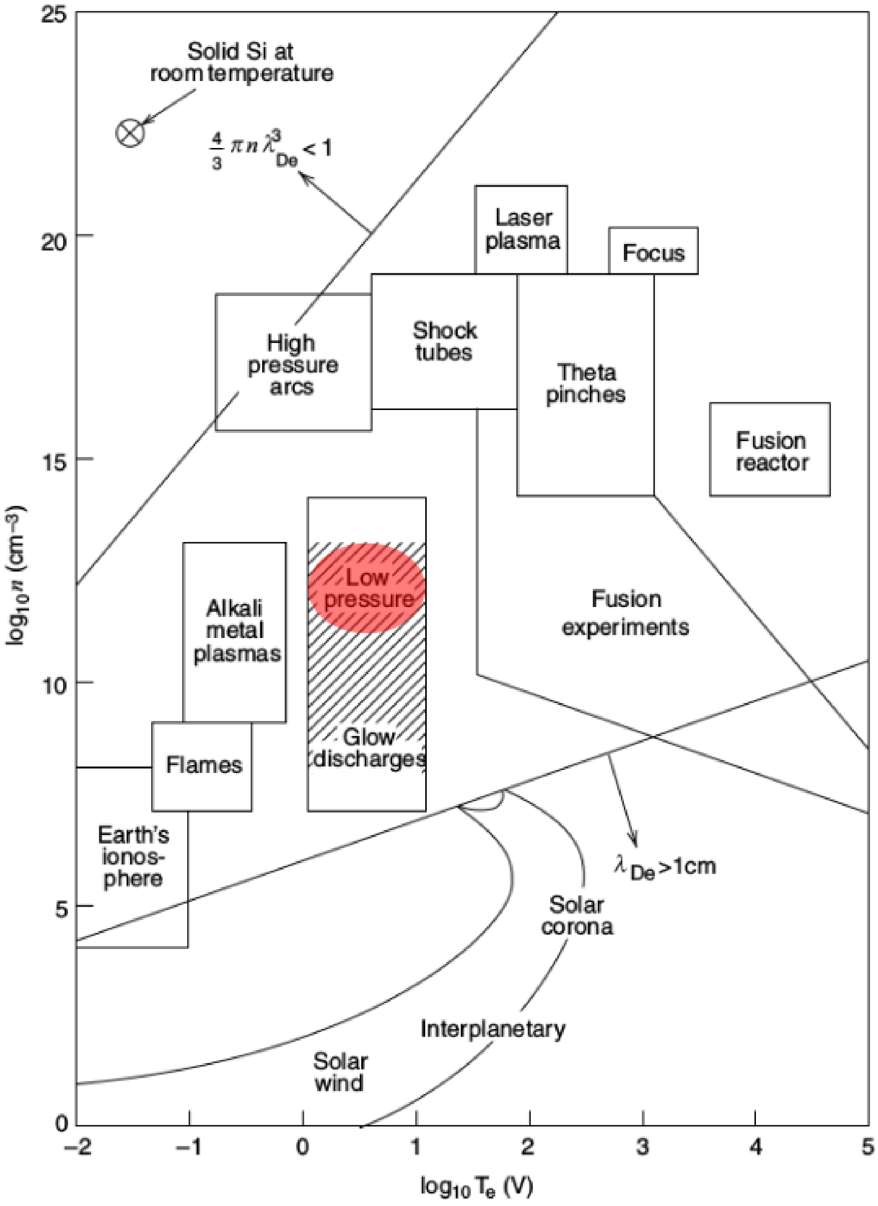

Figure 1.1: Parameter space of electron density and temperature that is spanned by natural and man-made plasmas. The value λ_{De} defines the Debye length, which is the characteristic length scale of the plasma. The envelope of electron temperature and density of particular interest to this thesis, low temperature plasmas at low pressure, is highlighted by the shaded region. Figure adapted from Ref. 2

The presence of charged particles enables a plasma to respond to externally applied electric and electromagnetic fields which has made them uniquely useful across many different technological applications[1,2]. For example, plasmas are useful as a means of generating chemically active species that can be used to change other materials directly[2–7], or as the source of useful species such as ions, photons, excited species, free radicals or hot gas that can be used in other secondary applications[3,6,8–10].

1.1.1 Electronegative plasmas

In principle, any type of gas can be used to generate a plasma so long as sufficient power is coupled to generate ionisation. The choice of gas depends on the particular application the plasma is to be used for[2]. It is possible to use gas that can form compounds, molecules or atoms that have a negative charge, or for dust particles to accumulate in the plasma that become negatively charged[1]. In some cases the influence of negative species within the plasma is significant, meaning that the macroscopic properties of the plasma are changed[1,2,11]. This type of plasma is typically referred to as an electronegative plasma or an electronegative discharge.

A low temperature, electropositive plasma has approximately equal densities of electrons and positively charged ions. As electrons are much lighter than ions, they have a larger thermal velocity. Electrons close to the walls and surfaces immersed in the reactor are therefore likely to reach them before the ions, after which they will be lost from the plasma. In order for the plasma to exist at steady state, an electron deficient region forms which prevents further loss of electrons through the formation of a positive potential. This near-surface region over which the positive potential acts is known as a plasma sheath[1,2].

In electronegative plasmas, the addition of negatively charged, high mass species changes the formation of the plasma sheath and therefore the behaviour of the plasma. The negative ions have a mass comparable to positive ions, which combined with their identical charge to the electron means that they are confined by the sheath to the centre of a plasma, and cannot conventionally leave the plasma bulk unless external fields extract them[1]. This increases the electron temperature within the plasma which in turn drives changes in the other properties[1,2]. Therefore, the analytical principles that are applicable to electronegative plasmas are distinct from those of their electropositive counterparts[1,2,11–13].

Electronegative plasmas are most commonly formed from the halogen elements such as chlorine, either as a pure halogen plasma or by the addition of them as an admixture[1,2]. The most common application of these types of electronegative plasmas are in plasma-surface processing, such as etching and deposition of materials. For example, chlorine can be added to plasmas that are used for thin film etching of copper[14]. Electronegative plasmas can also have more novel uses, such as the formation of ion-ion plasma. For example, SF_6 has been used to form an electronegative plasma from which negative ion flux can be extracted while minimising that for electrons[15–17]. Other non-halogen elements, such as oxygen or hydrogen, can also be used to form electronegative plasmas, finding applications in, for example, the production of ion beams[18,19].

1.1.2 Hydrogen plasmas

Hydrogen plasmas are of interest for a wide variety of technological applications, including: microelectronics[14], environmental studies, aerospace[20,21], Chemical Vapour Deposition, and surface processing. They can also be used as a source of protons[22]. The fact that it can form a stable negative ion has led to the development of many technologies that seek to extract them for applications away from the plasma. Hydrogen plasmas as a source of negative ions have been used in applications such as particle acceleration[18,23–26], neutron generation[27,28], mass spectrometry[29–32], nano-electronics manufacturing[33], and neutral beam heating for magnetic confinement fusion (MCF)[34–37].

Alongside the development of hydrogen plasmas for technological applications, the fundamental physics of it have also been studied[38–50]. Compared to other types of electronegative plasmas, hydrogen plasma is acknowledged as being relatively "simple". It is typically composed of dissociated hydrogen atoms, electrons, three types of positive ions (H^+, H_2^+, H_3^+), the negative atomic ion, and the hydrogen molecule[51]. This relatively low number of species belies a complexity that arises because the hydrogen molecule can occupy a large number of quantum states, as shown in figure 1.2.

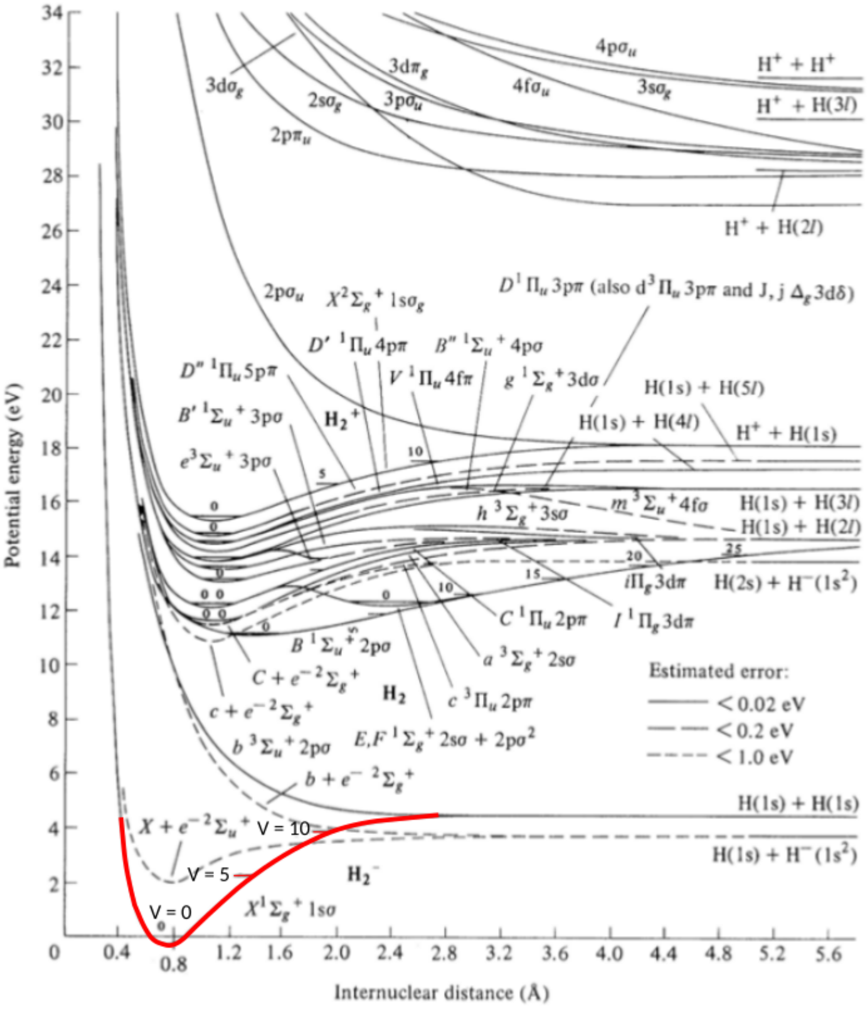

Figure 1.2: A potential energy curve diagram showing the energy of a selection of excited states of hydrogen. The vibrational energy levels $v = 0$, $v = 5$, and $v = 10$ of the hydrogen molecule are highlighted. Figure adapted from Ref. [2]

The interactions of these ro-vibrational states with each other has been studied for many years[52–60].

The technological applications that utilise hydrogen plasma require an understanding of the kinetic and spatial distribution of each neutral, excited and charged species[61,62]. This requires an understanding of the production and distribution of negative ions. Applications that extract negative ions from a hydrogen plasma also require an understanding of the processes that lead to negative ion formation.

1.2 Surface production of negative ions

The surface production of negative ions occurs via the interaction of plasma species with plasma-facing materials. This process is highly dependent on the nature of the surface in contact with the plasma. Plasma-facing surfaces can typically be separated into two groups, metallic surfaces and dielectric surfaces.

1.2.1 Production of negative ions from metallic surfaces

Figure 1.3 illustrates the key processes that occur when a metal surface interacts with a hydrogen atom.

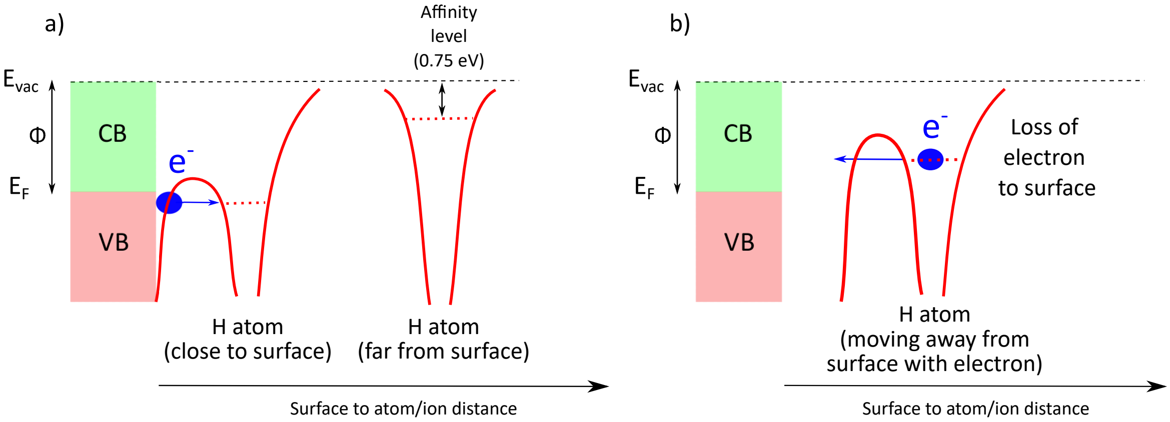

Figure 1.3: Schematic of electron affinity for a hydrogen atom approaching a metallic surface. (a) The atom at a large distance has an affinity level of 0.75 eV, but when close to the metallic surface the affinity level is downshifted, which allows an electron to tunnel from the valance band (VB) to the hydrogen atom. (b) As the hydrogen atom, with electron attached, moves away from the surface, the electron can tunnel back to empty states in the conduction band (CB) of the metal surface. E_{vac} represents the vacuum energy level, E_{f} the Fermi level and Φ the work function of the metal surface. Figure adapted from Ref. 63

Generally, for atoms approaching a surface, the affinity level of the atom is gradually downshifted until it overlaps with the valence band of the material. Electrons can then tunnel from the valence band of the surface to the approaching atom and form a negative ion, which is known as the resonant charge transfer (RCT) process, as summarised in Ref. 64 and depicted in figure 1.3 (a). For a metal, the conduction band is situated on top of the valence band. When a newly created ion begins to leave the surface, the probability of electron loss through tunnelling back to the conduction band is high due to the resonance between the affinity level of the negative ion and the empty states of the conduction band, as shown in figure 1.3 (b). This means that most metals produce negligible negative ions through surface ionisation[65]. However, metals with a low work function can be used to enhance negative ion production. A low work function increases the distance at which the resonance between the affinity level of the new ion and the empty conduction states occurs, reducing the probability that the electron tunnels back to the surface[64,65].

1.2.2 Production of negative ions from dielectric surfaces

In contrast to metals, where the conduction band lies on top of the valence band, the band gap of dielectrics suppresses the tunnelling of electrons from a newly created negative ion back to the surface of the material. This is shown in figure 1.4.

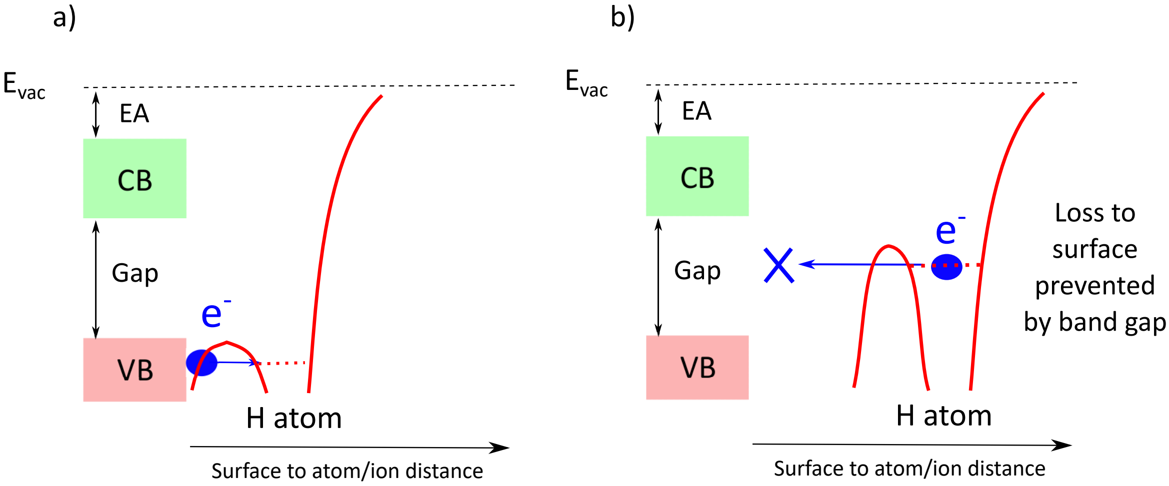

Figure 1.4: Schematic of electron affinity for a hydrogen atom approaching a dielectric surface. (a) The affinity level of the atom is downshifted such that electrons can tunnel from the surface to the approaching atom, but the atom must be significantly closer to the surface than for a metal surface because the valance band (VB) is at a lower energy level. (b) As the hydrogen atom with attached electron moves away from the surface, the electron is prevented from tunnelling back to the dielectric surface due to the band gap, until it is too far away from the surface for the electron to be in resonance with the conduction band (CB). E_{vac} represents the vacuum energy level and EA the electron-affinity. Figure adapted from Ref. 63

In figure 1.4 (a), in a similar manner as for a metal surface in figure 1.3 (a), the hydrogen atom approaches the dielectric surface and an electron can tunnel from the valence band of the surface of the material. However, as shown in figure 1.4 (b), as the hydrogen atom with attached electron moves away from the surface, the band gap prevents the electron from tunnelling back to the surface. This means that a new negative ion can travel a larger distance away from the surface before it reaches a point where its affinity level is in resonance with the empty states of the conduction band. The increased distance of the ion from the surface reduces the probability that the electron associated with the new negative ion will tunnel into the empty states of the conduction band, thereby increasing the negative ion yield[63,66].

1.2.3 Surface production of negative ions for neutral beam heating source: state-of-the-art

Negative ions for use in neutral beams for magnetic confined fusion are produced primarily through surface production processes[34]. This is achieved through the generation of a hydrogen plasma in an expanding inductively coupled plasma (ICP) driver, and extraction of negative ions through a series of grids in combination with a transverse magnetic field to minimise co-extracted electrons. Negative ions produced by surface interaction processes in close proximity to the grid are then extracted using electrostatic biasing[67,68]. High power (∼60 kW) and low pressure (∼0.3 Pa) ICP sources are used to minimise the collision of hydrogen species with the negative hydrogen ions which may cause their neutralisation and a reduction in the overall device efficiency[34]. Figure 1.5 shows a recently developed neutral beam source.

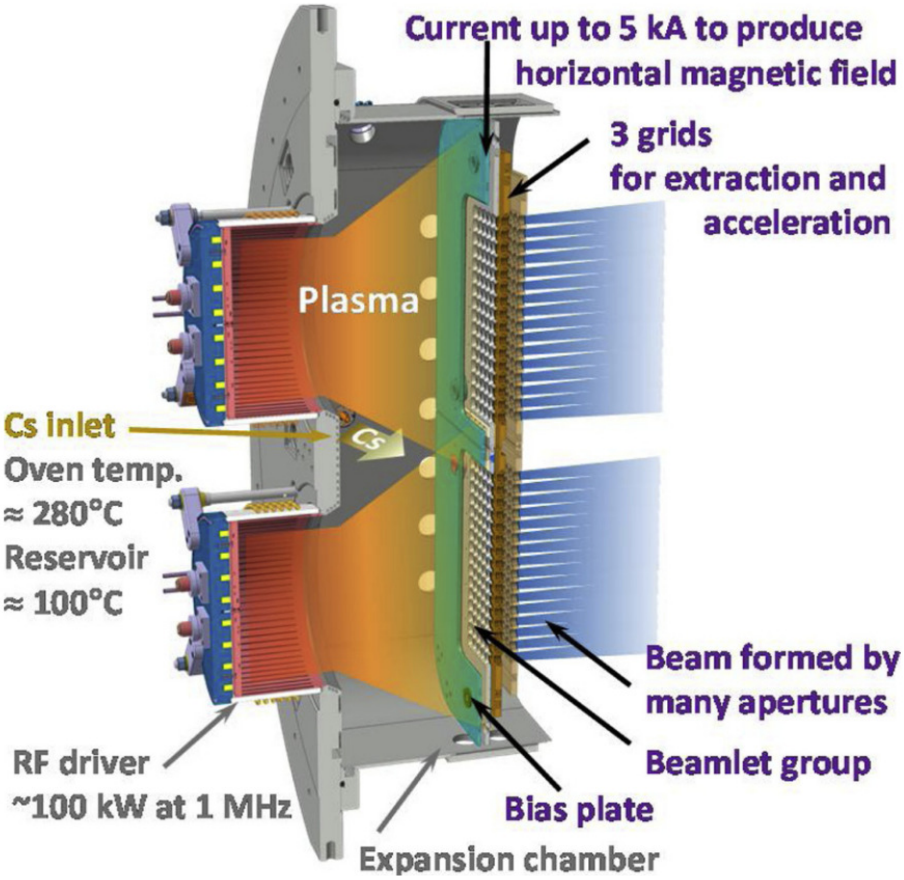

Figure 1.5: Diagram of the ELISE negative ion source developed for neutral beam heating with the major components labelled. Figure from Ref. 69

Caesium is added to the hydrogen plasma as this has been shown to greatly enhance the production of negative ions[19,70,71]. The mechanism for this increase has been demonstrated to be due to the caesium forming a low work function layer on the surfaces in contact with the plasma. The addition of caesium has since been critical for the successful deployment of negative ion sources for fusion, in particular for the negative ion source for the ITER project[72–74].

1.2.4 Current challenges: alternative materials to low work function alkali metals

A challenge for the next generation of negative ion sources is to remove the reliance on caesium. It is necessary to enhance the production of negative ions, but introduces significant engineering complexities. These include having to develop methods to control the amount of caesium being introduced to the neutral beam source during its operation so as to maintain a coating of caesium within the device, as well as limiting caesium pollution of the external components[75]. A quick calculation of the amount of caesium being introduced to the device during its operation (20 mg per hour) suggests that a substantial 1 kg of caesium is to be injected into the negative ion source every 6 years[75]. Further to this, extensive work is necessary to ensure acceptable performance of the device during its operation[69,75]. This has led to a desire for alternative plasma-facing materials to be investigated[63,75].

Currently there are numerous materials under investigation that include highly oriented pyrolitic graphite (HOPG)[63,76–78], novel electrides[79], LaB_6, MoLa[80], as well as those that have dielectric properties such as diamond-like-carbon (DLC) and diamond[76–78,81–86]. Novel electrides are of interest due to their low work functions[79]. However, durability and susceptibility to contamination may limit their effectiveness and work is ongoing to investigate how these materials behave when exposed to plasmas like those found in neutral beam sources[87,88]. Low work function metal surfaces such as MoLa and LaB_6 have previously been shown to be effective negative ion producing materials compared to other metals such as stainless steel[80], but their effectiveness cannot be easily enhanced further as they are limited by the inherent physical properties of the metal.

As previously introduced in section 1.2.2, one category of materials that has been postulated as being potentially suitable for high negative ion yields is dielectrics[66,89,90]. Of particular interest is diamond[63]. It is possible to grow diamond with specific physical and electronic properties[91–93]. This is an attractive proposition as it would then be possible to optimise negative ion production through careful selection of a particular surface property or use insights from fundamental studies to develop alternative materials based upon the favourable properties of diamond, some of which are listed below.

- It is a dielectric with a large band gap (5.5 eV)[94] that suppresses the destruction of negative ions as they leave the surface of the material.
- It can be grown to have 'designer' properties such as the preferential growth of a particular crystal face to alter the electronic structure of its surface[94].
- When it is being grown, dopants can be introduced to change its effective work function and electron affinity[95–98].
- It can have a negative electron affinity when the surface is hydrogen terminated[94],

which reduces its effective work function by decreasing the energy gap between the valence band and the vacuum level. This is thought to have a positive influence on negative ion production[63].

- When heated to 450°C, diamond has previously been shown to produce five times more negative ions compared to other forms of carbon e.g. graphite[81].

As a means of increasing the production of negative ions, previous work with diamond has investigated using single, nano- and micro-crystalline diamond and also *p*-type doping of micro-crystalline diamond (MCD) using boron[76]. The addition of boron to diamond has previously been demonstrated to increase the negative ion production, and it is of interest to investigate other dopants which may further increase this.

The *n*-type doping of diamond using nitrogen has not previously been studied in this context and it can potentially increase negative ion production for two reasons. Firstly, previous studies of the electronic properties of nitrogen doped diamond have demonstrated that nitrogen doping creates a deep donor level in the band gap of the diamond at 1.7 eV[99]. This decreases the effective work function to approximately 3.1 eV[100], which is lower than boron doped diamond (3.9 eV)[100] and un-doped diamond (∼4.5 eV, with hydrogenated surface and negative electron affinity)[101]. Secondly, it is thought that having the aforementioned deep donor level of electrons close to the vacuum level could increase the negative ion production by creating a source of electrons close to the vacuum level[19]. It is therefore of interest to investigate the properties of nitrogen doped diamond as a material for enhancing the surface production of negative ions.

1.3 Volume production of negative ions

In section 1.1, many examples were given of technological applications of hydrogen plasma. The development of these applications require an understanding of both surface production processes and volume production processes[24,73,102].

Away from the near-surface region in a hydrogen plasma, negative ions can be produced within the bulk of the plasma by a process called volume production[19,103]. The formation of a negative ion in the plasma can occur when a hydrogen molecule dissociates during a collision with an electron resulting in the formation of a neutral atom and a negative atomic ion. This type of collision is referred to as dissociative electron attachment.

$$\mathrm{e} \quad + \quad \mathrm{H_2(vib.} = 0 \text{ - } 14) \quad \rightarrow \quad \mathrm{H^-} \quad + \quad \mathrm{H} \tag{1.1}$$

where H_2(vib.) is a vibrationally excited hydrogen molecule.

As introduced in section 1.1, the hydrogen molecule has many ro-vibrational quantum states[51]. Of particular importance for negative ion formation in hydrogen is the vibrational states, as distinct from the rotational states. It has been observed that the higher the vibrational energy of the hydrogen molecule, the lower the threshold energy an electron requires to cause the dissociation of the hydrogen molecule. This also increases the collision cross section of the hydrogen molecule[19]. A lower threshold and larger collision cross section means that the likelihood of the hydrogen molecule forming a negative ion after experiencing an electron collision increases with increasing vibrational energy levels. Therefore, the production of highly excited vibrational states is of significance when considering negative ion formation within the bulk.

One of the main processes that leads to the excitation of a hydrogen molecule is through collisions with energetic electrons[51]. There are two main processes through which an electron collision can create a vibrationally excited molecule. The first type of collision provides energy to vibrate the hydrogen molecule directly. This is called an inelastic vibrational excitation reaction, that is otherwise referred to as an eV reaction[104].

$$\mathrm{e} \quad + \quad \mathrm{H_2} \quad \rightarrow \quad \mathrm{H_2(vib.)} \quad + \quad \mathrm{e} \tag{1.2}$$

The other type of electron collision proceeds in two steps, where the initial electron collision electronically excites the hydrogen molecule, which then spontaneously relaxes into a vibrationally excited state through the emission of a photon.

$$\mathrm{e} \quad + \quad \mathrm{H_2} \quad \rightarrow e + \mathrm{H_2}(\mathrm{B}^1\Sigma_u^+, \mathrm{C}^1\Pi_u) \rightarrow \quad \mathrm{H_2(vib.)} \quad + \quad \mathrm{e} \; + \; h\nu \tag{1.3}$$

This process is called the electron impact resonant vibrational excitation process, or the EV process[104]. These vibrationally excited states are stable due to the lack of a permanent dipole on the hydrogen molecule, and so can exist in the plasma for some time[51].

Once a vibrationally excited state exists, the vibrational energy can be shared between the molecules through collisions. There are three types of collisions that can occur[52,105,106]:

- Vibrational-Vibrational (V-V) reactions, which describe the exchange of vibrational energy between the molecules with little to no exchange of kinetic energy.
- Vibrational-Translational (V-T) reactions, where the vibrational energy of the colliding molecules is converted into translational (or kinetic) energy.
- Vibrational-Translational reaction, except one of the colliding species is a neutral hydrogen atom. This last type of collision involves the neutral hydrogen atom either giving or taking vibrational energy from a hydrogen molecule during a collision at the expense of some translational energy. This has been referred to as an "atomic V-T reaction" in this work.

Each of these reactions distribute the vibrational energy within the plasma between the vibrationally excited states of the plasma[105,106].

1.3.1 Current challenges: spatial variations in inductively coupled plasmas

A type of plasma that is of particular interest is the inductively coupled plasma. This type of plasma is typically formed by utilising a coil of wire either wrapped around the plasma reactor (spiral geometry), or formed into a spiral placed against the side of the reactor (planar geometry)[1,2]. The induced current produced by the coil or antenna exists in close proximity to where the coil or antenna is positioned[2]. The majority of the power from the coil is therefore deposited in a localised region within the plasma, which results in the formation of spatial gradients in species densities and the temperature of the neutral gas, as shown in figure 1.6.

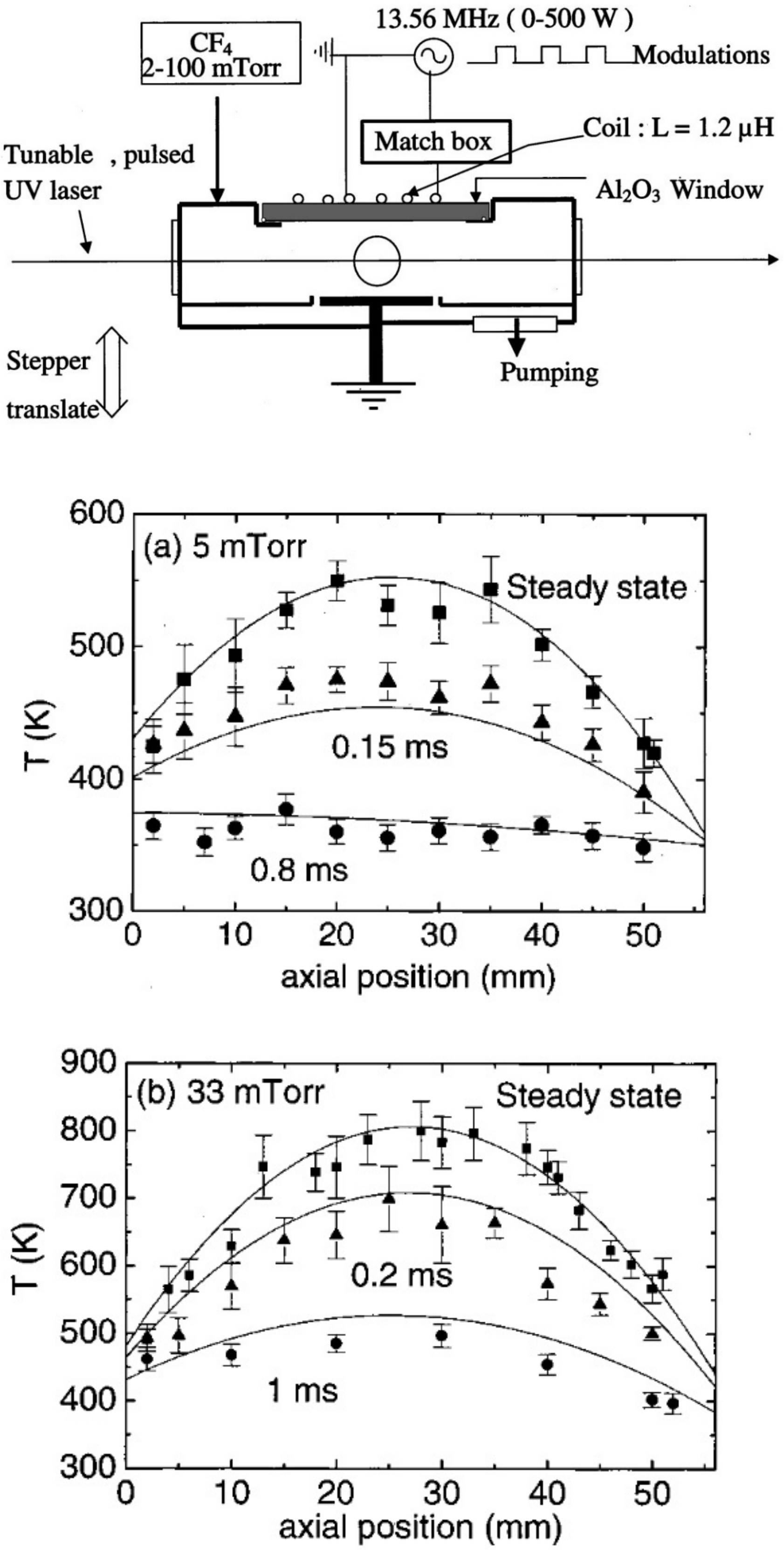

Figure 1.6: Schematic of a planar inductively coupled discharge with measurements of gas temperature taken within the plasma volume. The gas temperature is observed to have a peak in the centre of the discharge volume which decreases towards the edge of the plasma. Figure adapted from Ref. 107

These gradients become more severe as the power density (and ion flux) is increased, creating a trade-off between spatial plasma uniformity and process time[1,2].

Early work on hydrogen plasma modelling was mainly focused on building the understanding of the chemical kinetics[52–54,108,109]. It was through this work that the importance of the vibrational states and the interactions between them was established. This work mainly focused on the properties of a spatially uniform plasma. In more recent work, efforts have been made to increase the operational envelope[48,110], and link the features of these more complete plasma chemistry sets to spatial distributions by coupling the output of the 0D chemistry models into spatially dependent models for the electromagnetic field[111–113].

In progressing towards the development of spatially resolved models of hydrogen plasmas, reductions in the plasma chemistry have often been required to reduce computational expense. One example of this has been through the simplification of the vibrational kinetics. Such an approximation has been useful for developing an understanding of complex technological plasmas such as the negative ion sources for fusion[114–119], negative ion sources for particle accelerators[120,121], development of microdischarges[122], and for surface processing[123].

Where a more complete chemistry is incorporated, a reduction of the number of dimensions has often been utilised. Early work utilised a 1D kinetic model to study electron dynamics during collisions with ions and neutrals[124,125]. This work has continued, with the creation of a hybrid particle-in-cell (PIC) model[60,126–131], which has subsequently been experimentally benchmarked[132,133].

Recently, the incorporation of a reaction set that includes vibrational interactions has been carried out within a simplified 2D simulation framework using COMSOL, a multiphysics simulation platform[134]. However, an assumption that is made in this and other models is that the neutral species in the plasma have a uniform gas temperature[134,135]. While valid at low power densities, for increasing power densities which are typical for ICPs, as shown in figure 1.6, spatial gradients in the neutral gas can be substantial. This changes ionisation and chemical reaction rates. It is therefore of significant interest to develop our simulation capability to include:

- 2 dimensions
- Self consistent and spatially resolved evaluation of the neutral-species temperatures
- gas temperature dependent rates for the V-V and V-T reactions
- enthalpy changes for each reaction.

This capability would enable the study of how the spatially dependent plasma parameters impact the distribution of H_2 vibrational states, which in turn influence the production and distribution of negative ions[136,137].

1.4 Thesis outline

The layout of the thesis is as follows:

- Chapter 2 investigates the surface production of negative ions from diamond. Negative ion yield measurements with a continuous surface bias of diamond samples are undertaken. The results demonstrate that the introduction of nitrogen doping into the diamond films can increase negative ion production from the diamond.

- Chapter 3 extends the work of chapter 2, presenting results for negative ion yield from nitrogen doped diamond using a pulsed sample bias to minimise the creation of surface defects from positive-ion bombardment. The results suggest that the use of a pulsed bias prevents defects forming on the surface. However, the negative ion yield is lower than a continuous bias, which suggests the formation of defects plays a role in the formation of negative ions.

- Chapter 4 introduces a hydrogen plasma numerical simulation that has been developed to study the role of spatially resolved gas heating on negative ion production in the plasma bulk. The results of the simulations are compared to experimental measurements, showing reasonably good qualitative and quantitative agreement.

- Chapter 5 presents the results from the simulations within a planar inductively coupled plasma reactor. The impact of self consistently determining the spatially resolved gas temperature, as distinct from treating it as being isothermal, is investigated in relation to negative ion production. The results show that the distribution of vibrational states is impacted by the use of a spatially resolved gas temperature, which in turn changes the distribution of negative ions.

- Chapter 6 summarises the findings of the work and discusses next steps.

Chapter 2

Surface production of negative ions using nitrogen doped diamond

The development of alternative materials to caesium is of interest in applications such as ion beam sources, including those used for neutral beam heating. This chapter describes how the addition of nitrogen doping to diamond changes negative ion production upon application of a continuous negative bias. A low pressure and power helicon plasma source (26 W and 2 Pa) operating in capacitive mode is used to generate a deuterium plasma. Nitrogen doped diamond samples are immersed in the deuterium plasma and biased with a dc-voltage. Negative ions produced at the surface are measured via mass spectrometry to determine the negative ion yield. The application of a low-amplitude (-20 V) dc bias voltage in combination with nitrogen doping - where relative dopant concentration is determined via Raman spectroscopy - is found to increase the yield of negative ions relative to un-doped diamond films.

2.1 Technique to measure surface production of negative ions

Negative ions produced through surface interactions within hydrogen plasmas are difficult to measure because, following the plasma potential, they drift to the centre of the plasma where they are neutralised through collisions[19,51]. Laser photo-detachment can be utilised to measure the negative ions within the bulk of the plasma, but this method does not distinguish between negative ions produced through volume production processes or surface production processes[80]. To meet this challenge, a technique has been developed by the PIIM group in Marseille that can measure negative ions produced by surfaces exclusively. This technique utilises a negatively biased surface to accelerate positive ions from the plasma to the sample surface for the production of negative ions. The same bias voltage acts to direct negative ions produced at the surface through the sheath and plasma bulk to be measured by a mass spectrometer[63]. The experimental setup is shown in figure 3.1.

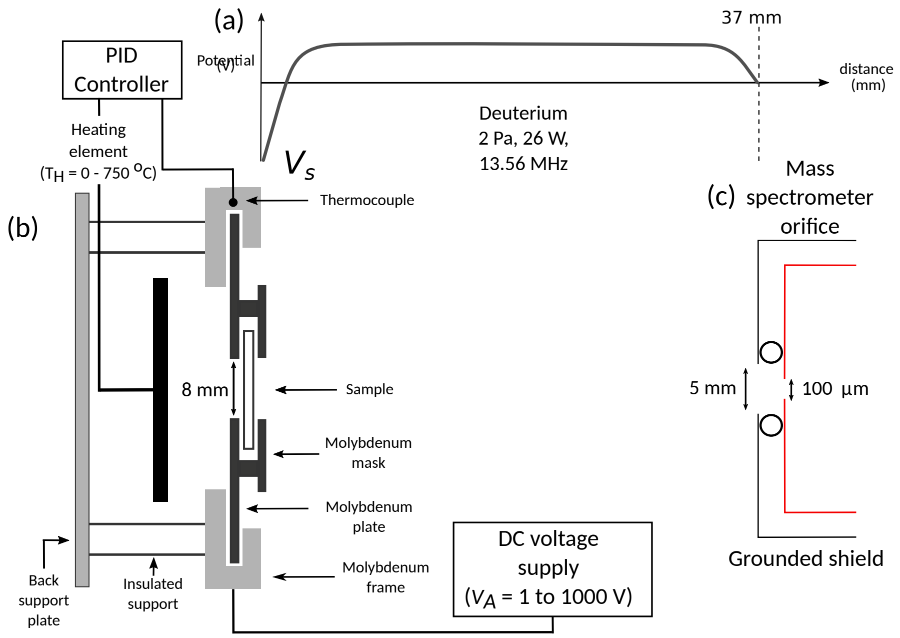

Figure 2.1: Schematic of the experimental setup. (a) Representative plasma parameters and potential profile between the biased sample surface at V_S and the mass spectrometer, 37 mm away. (b) Sample holder with heating element and thermocouple. (c) Mass spectrometer showing the external grounded shield and internal extractor orifice.

2.1.1 Description of the plasma source

A deuterium plasma, figure 2.1 (a), is produced via a helicon source operated in capacitive mode (2 Pa, 26 W), which then expands into a diffusion chamber[138]. The pressure of the diffusion chamber, as measured by a Baratron gauge (MKS), is regulated via a mass flow controller (7.6 sccm, BROOKS 5850TR) in combination with a 150 mm diameter Riber gate valve installed in front of a turbo molecular pump (Alcatel ATP400). To reduce experimental drifts, the experiment source chamber and lower spherical diffusion chamber have a base pressure of 10^{-5} Pa, which is lower than the base pressure of a previous setup of 10^{-4} Pa[138].

The relatively low power coupled to the plasma source results in plasma densities of approximately 10^{14} m^{-3} in the spherical diffusion chamber[138]. The choice of power and pressure was for similarity with previous work[83]. The positive ion composition of the deuterium plasma is measured by the mass spectrometer, described below, to be (84 ± 2) % D_3^+ ions, (14 ± 2) % D_2^+ ions and (1.1 ± 0.2) % D^+ ions. The measurement uncertainty represents the day-to-day variation of the measured plasma composition, however the actual error in the plasma composition due to the internal settings of the mass spectrometer may be higher[139]. As the dominant ion in the reactor is D_3^+, the momentum transfer collision of D_3^+ with neutral hydrogen is taken to be the dominant collision process. Taking the density of the neutral gas to be approximately $4\times10^{20} m^{-3}$, the mean free path of the D_3^+ ion-neutral collisions is approximately 2.5 mm. The mean free path for the negative ion-neutral collisions has been calculated to be approximately 37 mm[81,140]. The negative ion mean free path is the distance between the sample and the mass spectrometer, this means the loss of negative ions in the gap between the mass spectrometer and the sample is minimised. The mean free path of the positive ions is comparable to the width of the sheath in front of the sample. This means that, on average, a positive ion should undergo no collisions when crossing the sheath in front of the sample. As the pressure and the distance is the same for all of the samples, collisions within the sheath that reduce the positive ion energy before colliding with the sample surface, or the detachment of electrons from negative ions in the volume of the plasma before reaching the mass spectrometer, is expected to be similar for all samples. This means that negative ion yield and NIEDFs can be used to compare between samples.

The production of negative ions through a surface interaction requires a non-zero amount of energy (i.e the work function or material ionisation energy) to be given to an incoming particle in order to extract and capture an electron from the surface of the material. The energy in the described experiment comes from the positive ions kinetic energy. Alternative production processes that may produce detectable negative ions in this experimental setup include electron attachment of a molecule on the surface of a sample or a dissociative attachment reaction occurring within the sheath in front of the sample[19]. There cases are considered to be unlikely as, in the first case, a source of energy is necessary in order to extract an electron from the material. In the latter case, a dissociative attachment reaction requires an electron to collide with a hydrogen molecule. Within the sheath there are very few electrons meaning this reaction process is unlikely to occur. It is therefore reasonable to suggest that the main process of negative ion formation is through positive ion bombardment of sample surfaces. Previous work has demonstrated through an *a postori* simulation technique that the measured negative ion energy distribution matches extremely well with experimental measurements without the inclusion of the previously explored processes[85]. This supports the theory that positive ion bombardment is the dominant process of negative ion formation from carbon materials.

2.1.2 Temperature controlled sample holder

The sample holder is shown in figure 2.1 (b). It is attached to a dc-voltage source (Equipment Scientific Alimentation de Laboratoire CN7C) that can negatively bias the frame that holds the diamond sample. The voltage applied to the sample is defined as V_A, which is distinct from the voltage at the sample surface, V_S. The sample is positioned 37 mm away from, and perpendicular to, the plane of the mass spectrometer orifice. This is the closest distance that the sample can be placed in front of the mass spectrometer orifice, and is assumed to be sufficiently small to achieve minimal negative ion signal loss. It has previously been demonstrated that this distance has negligible effect on the shape of the negative ion distributions measured by the mass spectrometer[76,82].

The angular dependence of the NIEDFs for carbon materials has previously been shown to be similar[82,84,85]. Therefore, a single measurement can be used to compare between samples. A misalignment of the sample surface normal to the mass spectrometer would produce spurious results, so to prevent this, the alignment is regularly checked by rotating the sample and maximising the negative ion signal.

As shown in figure 2.1 (b), a tungsten heating element is built into the sample holder, which is used to heat the back of the sample. The heating element is controlled by a PID controller (designed and built by AXESS tech) using a K-type thermocouple inside the frame of the sample holder. By fixing a second thermocouple to the surface of the sample, its temperature is calibrated against the temperature measured by the PID. The heating element behind the sample increases the temperature of the sample's surface up to (750±20)°C.

2.1.3 Mass spectrometry for the measurement of negative ions

The mass spectrometer used in this experiment is a HIDEN EQP which is a commercial device that incorporates an electrostatic analysis technique and mass filter. A low background gas pressure is required, which is attained by separating it from the main plasma chamber by a small orifice with a diameter of 100 µm and differentially pumping it with a dedicated turbo molecular pump. A grounded screen is positioned above the mass spectrometer orifice to reduce radio-frequency (RF) fluctuations from the plasma source (not shown in figure 2.1)[84,138]. The mass spectrometer is controlled using MACsoft software on a dedicated PC.

The negative ions that enter the mass spectrometer are focused into an ion beam by the internal electrostatic lenses. The internal electrostatic lenses of the mass spectrometer are tuned for each specific sample surface biases and plasma condition in order to maximise negative ion signal[141].

The mass spectrometer is composed of a grounded shield around a polariseable orifice. It was found in the simulations of the plasma using the ONIX code that an orifice potential of 0 V at 2 Pa is optimal for producing a planar sheath in front of the orifice. A planar sheath is necessary for the analysis of the negative ion energy distributions using previously established techniques[85,138].

Positive ions impacting the samples are assumed to dissociate during impact[63,142], splitting the energy of the ion into its component particles (ie. for $D_3{}^+$, 3 deuterium nuclei). This means that because the plasma is predominantly composed of $D_3{}^+$ ions, the modal energy of the ions striking the sample's surface is $E_M = \mathrm{e}(V_S + V_p)/3$, where V_p is the plasma potential, giving approximately 11 eV per particle at $V_S = -20$ V and 48 eV at $V_S = -130$ V. We define these conditions as "low energy" ion bombardment and "high energy" ion bombardment, respectively.

The choice of -130 V is made to align with previously published work, whilst -20 V is chosen as this is the lower limit of what can be reasonably used to ensure effective self-extraction of negative ions from the sample surface into the mass spectrometer[76,82].

2.1.4 Procedure for measurement of negative ion energy distribution functions (NIEDFs)

Measurements were undertaken using the following method.

- The plasma was brought to steady state as determined by measurements of the positive ion energy distributions using the mass spectrometer.
- A bias of either $V_A = -20$ V or $V_A = -130$ V was applied to the sample.
- Negative ions produced following positive ion bombardment accelerate through V_S, cross the plasma volume and enter the mass spectrometer where the NIEDF was measured for sample temperatures between 30°C and 750°C in increments of 50°C.
- In order to compare the negative ion production yields for distinct material samples, the positive ion current was measured to the sample surface at 30°C for $V_A = -20$ V and $V_A = -130$ V, using a copper electrode in the place of a sample which was insulated from the sample frame[82]. This method of measurement could not be used at high temperatures due to a temperature sensitive insulator used to isolate the copper electrode from the sample holder frame. Instead, in order to roughly monitor changes in the positive ion flux onto the sample, the positive ion current to the entire sample holder was measured using an ammeter connected to the frame of the sample holder. This showed that there was a thermal drift in the positive ion current to the entire sample holder of approximately 5% irrespective of sample at both −20 V and −130 V applied biases.
- The negative ion counts for each sample were integrated with respect to energy and then divided by the positive ion current measured separately to give the relative negative ion yield for the sample. The possible small changes with temperature to the isolated sample were not taken into account[82]. This is given in arbitrary units as the mass spectrometer is not calibrated to count an absolute number of negative ions.

2.1.5 Description of the negative ion energy distribution function

The mass spectrometer measures the energy distribution of the negative ions coming from the sample surface. This can be used to infer the production processes that lead to their formation on the samples.

There are two situations that can occur during a positive ion collision with the surface of a sample that causes a negative ion to be formed. The first is that the positive ion undergoes a collision or multiple collisions with the surface of the sample. The positive ion is converted to a negative ion whilst it still possess some kinetic energy and so leaves the surface with a non-zero kinetic energy. The other case is that the positive ion loses all of its energy in a collision with the surface of a sample and a negative ion is produced at rest on the surface (i.e. $E_k = 0$ eV). In the latter case, the negative ion will be accelerated from the surface with an energy equal to the plasma potential *(V_p)* plus the negative bias at the surface of the sample, V_S.

If is now assumed that the negative ion crosses the plasma with no loss of kinetic energy, which is equivalent to the electron charge multiplied by the plasma potential plus the surface bias of the sample $E_k = \mathrm{e}(V_p + V_S)$, and is at an angle that allows it to enter the mass spectrometer, the negative ion must lose energy equivalent to the plasma potential in front of the mass spectrometer, $\mathrm{e}\,V_p$. Therefore negative ions formed at rest on a sample surface, $E_k = 0$ eV, will be measured with energy equivalent to the bias applied to the sample surface, $e\,V_S$.

In some cases a positive ion collision will produce negative ions with a non-zero initial energy (i.e. $E_k > 0$). This means that when measured by the mass spectrometer they have an energy of $E_k + \mathrm{e}(V_p + V_S)$. The resulting negative ion energy distribution function (NIEDF) can then be used to infer the negative ion production processes on the sample surface.

The relatively low pressure of the plasma means there are few collisions between negative ions and neutrals[138,139]. Any collisions that do occur would predominantly be detachment collisions with deuterium molecules, which would neutralise the negative ions, thus preventing measurement of negative ions that have undergone collisions[36,138,139]. The plasma potential in front of the mass spectrometer prevents negative ions generated through volume production processes from entering, therefore the energy of any negative ions that are measured must have been accelerated away from the sample surface[138,139].

Once a measurement of the negative ions from a sample surface has been completed, the measured NIEDF is put into terms of E_k, the kinetic energy of the negative ion when it was formed. This is possible because the total negative ion energy upon entering the mass spectrometer, E, is a conserved quantity:[138]

$$E = E_k - eV_S \tag{2.1}$$

The NIEDFs presented in this work have had the applied voltage, V_A, added to the measured negative ion energy distribution to show the kinetic energy the negative ions possessed on formation.

The applied voltage, V_A, is used instead of the surface voltage, V_S, because the surface voltage can be influenced by the conductivity of the sample and no direct measurement of the surface voltage is possible.

The typical distribution of negative ions from carbon surfaces measured using the technique described above features a peak in the number of negative ions formed almost at rest, with a tail that extends to higher energies. This can be observed in an example NIEDF in figure 2.2.

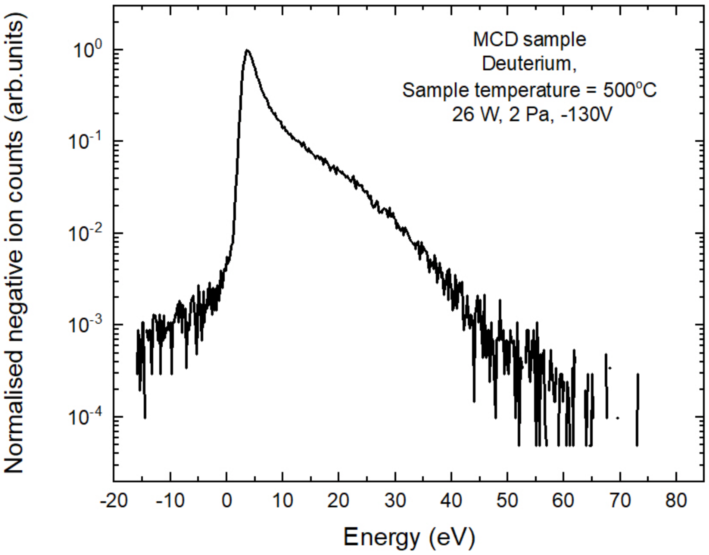

Figure 2.2: Example NIEDF from a micro-crystalline diamond (MCD) sample with a sample bias of -130 V, at a sample temperature of 500K and plasma power of 26 W.

From previous studies, negative ion energy distributions have been compared to simulations that account for the trajectories of negative ions between the sample surface and mass spectrometer[84]. This means that an understanding of the processes that lead to the observed negative ion energy distribution function can be used to determine the production processes.

2.2 Determining the negative ion yield

The negative ion yield is used as a means to compare the production of negative ions between samples, applied voltages and biasing techniques. This is defined as:

$$\alpha = \frac{1}{I} \int N_{D^-}(E)\ \mathrm{d}E \tag{2.2}$$

where N_{H^-} is the number of negative ion counts detected by the mass spectrometer, which are integrated with respect to incident ion energy, E. I is the positive ion current to the sample. As only a proportion of the negative ions that are produced by the sample surface are collected by the mass spectrometer, the negative ion yield is a relative measurement that can be used to compare between samples. Previous work has demonstrated that there is little difference in the angular distribution of negative ions between carbon samples under similar conditions[84,138]. This means that it is possible to compare relative negative ion yield from carbon materials using a fixed sample angle, though negative yield comparisons to other types of materials at this same angle cannot be carried out.

2.2.1 Measuring the positive ion current

To measure the positive ion current, an electrically isolated copper electrode was inserted into the sample holder in the place of a sample. This electrode was isolated from the rest of the sample holder through the use of Kapton tape. The molybdenum bracket, used to affix samples to the sample holder, acted as a guard ring on the electrode to reduce edge effects interfering with the measurement of the positive ion current. The electrode and sample holder were electrically connected in parallel to reduce differences in sheath expansion from affecting the positive ion current measurement.

2.3 Sample preparation

2.3.1 Micro-crystalline boron doped diamond and micro-crystalline diamond

MCD and MCBDD samples were prepared for the study by a collaborator, Laboratoire des Sciences des Procédés (LSPM). The samples were prepared in a bell jar reactor using plasma enhanced chemical vapour deposition (PECVD), as described in Ref. 143. The boron doped samples used in this study are comparable to the samples used in previous works where the gas phase doping level used is high (1000 ppm) to ensure a fully conductive diamond layer[76].

2.3.2 Micro-crystalline nitrogen doped diamond

The nitrogen doped diamond films were similarly prepared by the LSPM group using a similar PECVD technique to the MCD and MCBDD. The PECVD process utilised a bell jar reactor with a pressure of 200 mbar, microwave power at 3 kW, substrate temperature of 850°C, background hydrogen gas mixture with a methane concentration of 5%. The ratio of nitrogen in the gas mixture was set as a means to vary the concentration of nitrogen in the MCNDD film. Each film was deposited on to a (100) orientated silicon wafer.

2.4 Characterisation of the diamond samples

A laser confocal microscope (S neox, Sensofar) was used to observe the diamond surface morphology as shown in figure 2.3.

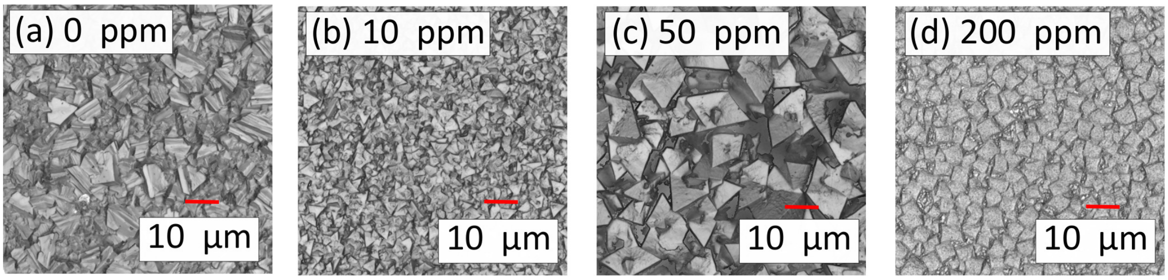

Figure 2.3: Confocal microscopy images of the diamond films grown with gas phase concentrations of (a) 0 ppm (b) 10 ppm (c) 50 ppm and (d) 200 ppm. The diamond crystals change in shape and size between the 4 gas phase dopant concentrations, from a mixture of (111) and (100) faces at 0 ppm and 10 ppm to predominantly (111) faces at 50 ppm, and then to predominantly (100) crystal faces at 200 ppm.

From visual inspection, the crystal grains are observed to have grown to exhibit (111) crystal faces, (100) crystal faces, or a mixture of both, dependent on the concentration of nitrogen dopant introduced in the gas phase during sample growth[144]. As the gas phase nitrogen concentration is increased from 0 ppm to 50 ppm the crystals are observed to exhibit an increased proportion of (111) faces, with predominantly (111) faces observed at 50 ppm. As distinct from these, the crystal grains of the diamond film with 200 ppm gas phase doping displays predominantly (100) faces. The diamond films grown with 200 ppm nitrogen concentration in the gas phase are different to the other samples, due to large crystals interspersed with regions of what appear to be much smaller crystals with a less pronounced crystal orientation. The size of the crystals for the 0 ppm sample, figure 2.3 (a), are approximately 10 µm, whilst the 10 ppm sample, figure 2.3 (b), has a much smaller average crystal size, at approximately 1 µm. The 50 ppm sample, figure 2.3 (c), has a crystal size similar to the 0 ppm sample, at approximately 10 µm. The 200 ppm sample, figure 2.3 (d), as previously described, appears to have a distribution of large crystals separated by smaller crystals, here the average crystal size of the larger crystals is approximately 5 µm.

A brief optical microscopic inspection of the samples prior to taking Raman measurements showed relatively uniform crystal distribution across the surface of all the samples and allowed for precise targeting of a dominant crystal near to the centre of the sample to be the subject of the Raman measurement. A quantitative comparison between Raman spectra has not been carried out as this requires the measurement of the polarisation of the Raman emission and a good understanding of the grain orientation[145].

Figure 2.4 shows the Raman spectra from samples of nitrogen doped diamond with gas phase nitrogen doping of 0 ppm to 200 ppm.

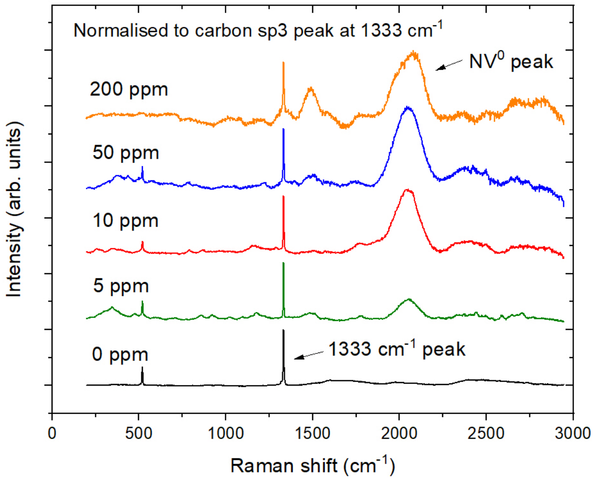

Figure 2.4: Raman spectra of nitrogen doped diamond samples taken at the centre of a dominant crystal face. The spectra are presented with the background subtracted (in order to aid clarity and comparison between samples) and normalised to the carbon sp3 peak, observed here at 1333 cm^{-1}. The laser wavelength used for the measurements is 514 nm.

The spectra in figure 2.4 have been presented with the background fluorescence removed and normalised to the 1333 cm^{-1} peak, which can be attributed to sp3 bonded carbon (the diamond bond of carbon)[96,146]. The normalisation to this peak is justified due to the transparency of the diamond films such that the measurement is integrated across the sample thickness. The normalised spectra can therefore enable a comparison between samples that accounts for any change in the thickness of the MCNDD film[146].

The broad peak centred at 2100 cm^{-1} observed in figure 2.4 can be attributed to nitrogen vacancy centres (NV^0) that have been introduced into the diamond[147]. This broad peak appears, not due to vibrational modes, but due to the electronic signature attributed to nitrogen vacancy centres and in reality lies at an energy level of 2.15 eV. As Stokes Raman spectroscopy is energy loss spectroscopy, this peak appears arbitrarily at 2100 cm^{-1} when using a 514 nm laser. Using another laser to perform the Raman spectroscopy results in a change in the wavenumber of this peak[148].

As the measurement configuration is the same for all samples, a relative comparison of the number of nitrogen centres in the diamond can be made using the broad 2100 cm^{-1} peak. This can then be used to infer relative nitrogen concentration[149]. As shown in figure 2.4, the ratio of the NV^0 peak to the peak centred at 1333 cm^{-1} increases with increasing gas phase dopant concentration, for samples 0 ppm to 50 ppm (200 ppm will be discussed below). This is consistent with previous work, which showed a similar increase in the magnitude of the NV^0 characteristic peak with an increase in the gas phase nitrogen doping[150].

In figure 2.4, the Raman spectrum of the 200 ppm nitrogen doped diamond has a peak at 1500 cm^{-1} that has a much higher intensity than the other samples. This peak is of particular interest as it is associated with the sp2 bond of carbon that has previously been associated to graphite-like bonds[146]. The ratio of the peaks at 1333 cm^{-1} and 1500 cm^{-1} implies that there is a higher ratio of graphite in the 200 ppm diamond film compared to the other samples[76,151,152]. The 200 ppm nitrogen doped diamond sample also exhibits a NV^0 centre peak at 2100 cm^{-1}, which is slightly lower than the 50 ppm sample, suggesting a reduction in the number of nitrogen vacancies, and therefore, a reduction in the concentration of nitrogen in the diamond.

The observed increase in intensity of the NV^0 peaks, increasing from 0 ppm to 50 ppm, may be attributed to both the increase in nitrogen introduced in the gas phase and by a change in the crystal face from a mix of (100) and (111), figure 2.3 (a) and (b), to a primarily (111) face for which impurity incorporation is higher than that for (100) crystals, figure 2.3 (c). This is consistent with the results of previous work[150,153,154]. This same process may then account for the slightly lower 2100 cm^{-1} peak for the 200 ppm sample compared to the 50 ppm samples despite a fourfold increase in the nitrogen gas phase content. This decrease could be attributed to the change in the crystal orientation (see figure 2.3 (c) and (d)), from a (111) dominant crystal surface for the 50 ppm sample to predominantly (100) crystal orientation for the 200 ppm sample.

The surface characterisation of the samples show that the incorporation of nitrogen into the PECVD process has multiple effects on the diamond produced, aside from only substitutional or interstitial incorporation of nitrogen into the diamond lattice. For these samples, separating the difference in negative ion yield due to the influence of the crystal face or the nitrogen content in the diamond is not possible because of the interrelated nature the presence of nitrogen in the gas phase has with the crystal face orientation and the measurable number of nitrogen vacancy centres. This is an active area of research[155]. However for this study, as nitrogen doping is the main influencing factor that generates the differences between the samples, it is reasonable to suggest that it is possible to associate the nitrogen gas phase doping with the negative ion yield and this is how the samples will be defined in the next section.

2.5 Comparing negative ion yield with increasing concentration of nitrogen doping

Figure 2.5 presents the negative ion yield from MCNDD for different dopant concentrations, as measured in the gas phase during sample preparation.

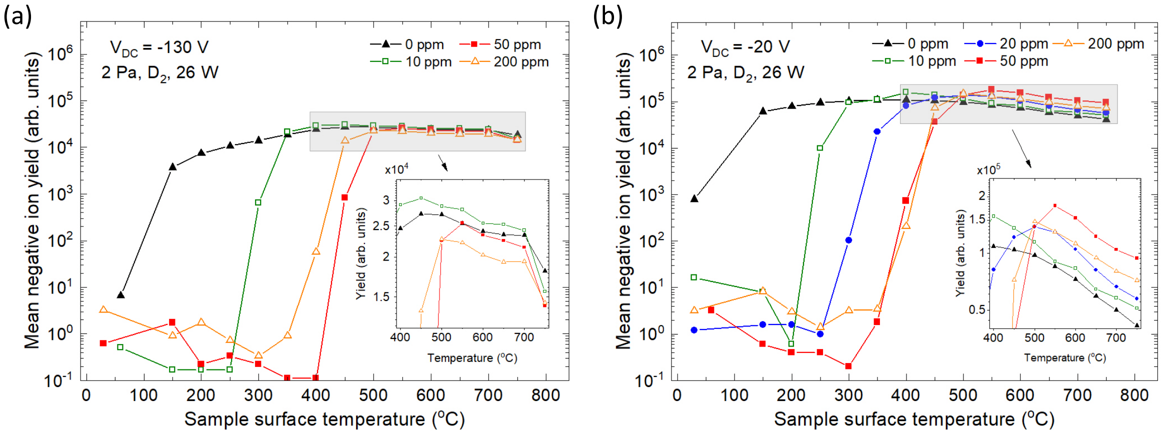

Figure 2.5: Negative ion yield plotted with respect to sample temperature for micro-crystalline nitrogen doped diamond (MCNDD) of doping concentration between 0 ppm and 200 ppm for (a) $V_A = -130$ V and (b) $V_A = -20$ V. Low pressure deuterium plasma operated at 2 Pa and 26 W. Insets for both (a) and (b) depict the highlighted regions' negative ion yield for temperatures between 400°C and 750°C. Solid lines have been added to guide the eye.

In both figures 2.5 (a) and (b) the yield profile for MCNDD has a distinct shape. For example, at 50 ppm, the measured yield is practically zero between a temperature of 30°C and 400°C. At 450°C, the yield rapidly increases by several orders of magnitude to a maximum at 550°C. This transition is similar for all nitrogen doped samples with the transition occurring at temperatures ranging from 250°C to 450°C. This is somewhat unlike MCD which produces measurable negative ions for all temperatures. The trend for MCD is a gradual increase to a maximum yield at a temperature of 450°C (−130 V, "high energy" bombardment) or 400°C (−20 V, low energy bombardment), there is then a decrease in yield from this maximum yield as the temperature is increased further to the maximum temperature of 750°C. It can also be observed that between ∼30°C and ∼150°C, MCD does undergo a transition, though this is smaller than that seen for MCNDD.

It is important to note that the negative ion yield measured using the described technique relies on a conductive sample surface. A non-conductive sample does not allow negative ions to be accelerated to the mass spectrometer at an energy which the mass spectrometer is tuned for. The magnitude of the transitions seen in figure 2.5 is a feature of this experimental technique which inadvertently highlights the temperature at which samples become conductive, such that $V_A = V_S$.

The difference in trends between MCNDD samples and the un-doped diamond can be attributed to the differences in conductivity between MCNDD and MCD. Previous work with MCD has shown that it has poor conductivity close to room temperature, which explains the increase in yield occurring between 30°C and 150°C[63]. Regarding MCNDD, the temperature at which the sharp increase in yield occurs appears to be dependent on the nitrogen doping of the diamond sample. The results of previous work suggest that the level of interstitial nitrogen doping influences the conductivity of diamond[98,156,157] and this sharp increase is consistent with increasing nitrogen dopant concentration and its influence on the conductivity of the diamond, supporting the argument that the nitrogen incorporated into the diamond increases as gas phase nitrogen is increased during its production. The low conductivity of MCNDD is associated with a distortion of the carbon lattice that produces a deep donor level. The nitrogen dopant forms a lone-pair on the nitrogen atom and a dangling bond with one of the carbon atoms of the lattice surrounding it. This means that it has a low conductivity at room temperature[158].

An exception to this trend is the results for 200 ppm in both figure 2.5 (a) and (b). These results do not exhibit a significant increase in the sample temperature at which the film becomes conductive relative to the 50 ppm MCNDD sample. This can be explained by considering figure 2.4. The nitrogen content measured using Raman spectroscopy suggests a nitrogen content that is similar for 200 ppm and 50 ppm MCNDD samples meaning, in the absence of other influences, a similar conductivity for these two samples could reasonably be expected.

The maximum yield from each sample occurs at temperatures between 400°C and 550°C, which is highlighted in the insets of figures 2.5 (a) and (b). For the 0 ppm and 10 ppm samples, the maximum yield occurs at 400°C, whilst for 20 ppm (and 200 ppm) it occurs at 500°C and for 50 ppm, at 550°C. As mentioned previously, a conductive sample surface is necessary to hold a DC surface bias which is necessary for the acceleration of negative ions into the mass spectrometer. The trend of increasing temperature for maximum yield as dopant increases (excluding 200 ppm) could be related to the maximum yield in these experimental conditions being restricted by the conductivity of the samples. For example, the maximum yield for MCD and MCNDD (10 ppm) is at the peak of a gradual increase and decrease in yield as temperature is increased from ∼30°C to ∼400°C and then from ∼400°C to ∼750°C respectively. This is most clearly observed in figure 2.5 (b) for the 10 ppm sample. This sample is distinct from the other MCNDD samples as the 10 ppm sample exhibits an increase in yield as the temperature is increased (due to a change in conductivity) then a further smaller increase up to a maximum negative ion yield at ∼400°C. The yield then gradually decreases as the temperature is increased further. The other MCNDD samples also undergo an increase in yield due to a change in conductivity, but no further gradual increase in yield is observed as temperature is increased.

It could therefore be reasonable to suggest that the peak yield conditions are not observed due to a lack of conductivity for samples with more than 20 ppm gas phase nitrogen doping. The trends observed for the 0 ppm and 10 ppm samples suggest that a temperature of approximately 400°C may be the temperature at which these MCNDD with more than 20 ppm gas phase doping produce the highest yield. A technique to measure negative ions that does not require a conductive surface would be necessary to explore this further.

In figure 2.5 (a), the effect of the nitrogen doping on the maximum yield is not readily observed when a bias voltage $V_A = -130$ V is applied to the sample. This is unlike figure 2.5 (b) in which a bias voltage of $V_A = -20$ V is used. In this data there is an observed difference between the nitrogen doped and non-doped diamond. The yield in figure 2.5 (a) for the MCNDD samples and MCD samples is also lower than the yields from all of the samples in figure 2.5 (b). A higher bombardment energy as a result of the high magnitude bias is associated with an increase in sp2 bond formation in diamond[85]. It is reasonable to suggest that the reduction in yield for the higher magnitude bias creates more sp2 defects which decreases the yield. Additionally, if the yield is not changing with the addition of nitrogen to the diamond, it is also reasonable to suggest that the nitrogen doped diamond may be more susceptible to defect formation due to high energy bombardment which would result in a surface state that does not enhance the negative ion yield through nitrogen doping.

The apparent influence of nitrogen doping on the measured negative ion yield is observed in figure 2.5 (b) where a sample bias voltage $V_A = -20$ V is applied. When comparing the yield at temperatures above 550°C, i.e. when all of the MCNDD films are conductive, it is observed that the negative ion yield is higher at similar temperatures, when increasing nitrogen dopant concentration for the 0 ppm to 50 ppm cases. The mechanism for such an increase in yield is not immediately clear and future work will be necessary to identify the specific cause of this increase. For example, it could be solely due to interstitial nitrogen, or a change of crystal orientation or a combination of both. In any case, the increase is correlated to the amount of nitrogen dopant with the exception of the result observed for 200 ppm gas phase doping, which produces a comparatively lower yield compared to the 50 ppm case. Should interstitial nitrogen content be the main cause of an increase in negative ion yield, this result can be explained by the Raman measurements shown in figure 2.4. The Raman measurement suggests that the diamond has a similar amount of nitrogen doping when comparing the 2100 cm^{-1} peak for the 50 ppm and 200 ppm samples. However the Raman measurement also suggests that the 200 ppm MCNDD sample has more carbon sp2 bonds (graphite-like) than the 50 ppm sample. The reduction in yield observed for the MCNDD (200 ppm) sample compared to MCNDD (50 ppm) sample is therefore consistent with previous work, which observed that an increased number of sp2 bonds is less favourable to negative ion production[76,82]. This work suggests that this is still the case with nitrogen doped diamond samples.

2.6 NIEDF comparison between MCD, MCBDD and MCNDD

NIEDFs for MCBDD and MCNDD are presented in figure 2.6 to compare negative ion production processes between MCBDD, a previously studied material[63], and the MCNDD samples. In this figure the NIEDFs are normalised to the modal negative ion energy at temperatures where MCBDD and MCNDD samples are conductive.

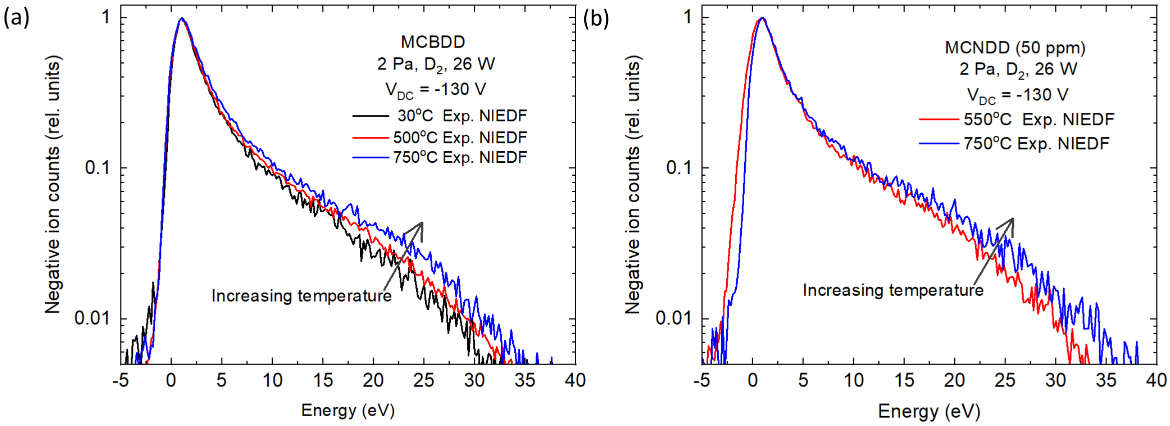

Figure 2.6: NIEDFs for: (a) micro-crystalline boron doped diamond (MCBDD) at 30°C, 500°C and 750°C, (b) micro-crystalline nitrogen doped diamond (MCNDD) at 550°C and 750°C. Increases in sample temperature lead to a decrease in the number of low energy negative ions, which results in an increase in the height of the tail of high energy negative ions when the distribution is normalised. Low pressure deuterium plasma operated at 2 Pa and 26 W.

The distribution of negative ions in the NIEDFs have previously been shown to be useful for determining the negative ion production mechanisms involved when using carbon samples[138]. There are two production processes that are considered to be responsible for negative ion formation from carbon: backscattering and sputtering. Backscattering produces negative ions when an incoming positive ion is reflected off the deuterated carbon lattice of the samples. During such a collision, the positive ion captures two electrons to produce a negative ion[78]. As distinct from this, sputtering relies on the ejection of adsorbed deuterium from the carbon lattice. During this ejection it takes an extra electron from the surface producing a negative ion[78].

When considering a normalised NIEDF, a reduction in the proportional magnitude of the NIEDF peak at low energies will result in an increase in the apparent proportion of negative ions at high energies. The NIEDFs in figure 2.6 (a), show that for MCBDD the proportion of high energy ions increases as the surface temperature increases. This is because the main contribution to the measured yield is low energy ions, which are predominantly created through the sputtering process, as distinct from backscattering, due to the acceptance angle of the mass spectrometer[63,138]. Previous work has confirmed this interpretation through comparison of experimental results with SRIM simulations[85].

At a surface bias of $V_S = -20$ V, i.e. the “low energy” bombardment condition described in section 2.1.3, the high energy tail observed in the NIEDFs in figure 2.6 is not produced. Without a high energy tail, the normalised NIEDF shapes are not strongly dependent on the deuterium surface content[82], and comparison of the ratio of sputtered to backscattered particles cannot be readily inferred using this approach. For this reason, only results with a surface bias of $V_S = -130$ V are presented.

Comparing figure 2.6 (a) to figure 2.6 (b), which presents NIEDFs for MCNDD at 550°C and 750°C, i.e. temperatures at which the sample is conductive, it is observed that MCNDD displays a similar increase in the proportion of high energy negative ions as the sample's surface temperature increases. This implies that MCNDD has similar negative ion production properties to MCBDD.

The trends for MCNDD and MCD observed in figure 2.5 and discussed in the previous section can be explored in the context of figure 2.6. Figure 2.5 shows that the yield for MCD increases up to sample temperatures of ∼400°C and decreases as its temperature is increased further. This is similar to the trends observed for samples of MCNDD when they are conductive. The increase and then decrease in yield as temperature is increased, from ∼30°C to ∼400°C and then from ∼400°C to ∼750°C respectively, can be attributed to two processes that combine to generate the observed trend in figure 2.5. The first process is the removal of defects on the sample surface. The heating of the sample results in an enhancement of the etching of sp2 bonds created by the bombarding positive ions resulting in a surface which results in a higher ratio of sp3 bonds[76]. The increased proportion of diamond bonds on the surface increases the negative ion yield, as explored in previous work through Raman spectroscopy[63,76,81,82]. The second process is the previously discussed decrease in the sputtering contribution to the negative ion yield due to out-gassing of deuterium from the sample surface, as observed in the measurements of figure 2.6. As temperature is increased, the influence of each of these processes on the measured negative ion yield is observed to vary significantly. At temperatures below ∼400°C, the reduction in defects increases the yield, whilst the outgassing does not cause a significant decrease in the sputtering contribution. At temperatures above ∼400°C, the decrease in sputtering contribution reduces the yield by a greater extent than the reduction in defects caused by the elevated temperature, causing a reduction in the measured negative ion yield[76].

For the samples of nitrogen doped diamond with more than 20 ppm nitrogen added in the gas phase, the MCNDD film is not conductive at temperatures where the previously mentioned reduction in the defects can increase yield, i.e. between 30°C and 400°C. A more thorough exploration of the resulting interplay between the reduction of defects and the decreasing sputtering contribution is beyond the scope of this work. However, figure 2.6 (b) suggests that the decrease in yield due to a decrease in the sputtering contribution is consistent with current understanding of the behaviour of negative ion formation on micro-crystalline doped diamond.

2.7 Comparing negative ion yield between different types of diamond doping

The negative ion yield with respect to sample surface temperature of the MCD, MCBDD and MCNDD samples is shown in figure 2.7, with high energy ion bombardment ($V_A = -130$ V) shown in figure 2.7 (a) and low energy bombardment ($V_A = -20$ V) shown in figure 2.7 (b). 50 ppm MCNDD is chosen as a comparison to MCD and MCBDD as this produced the highest relative negative ion yield of all the nitrogen doped diamond samples, as shown in figure 2.5.

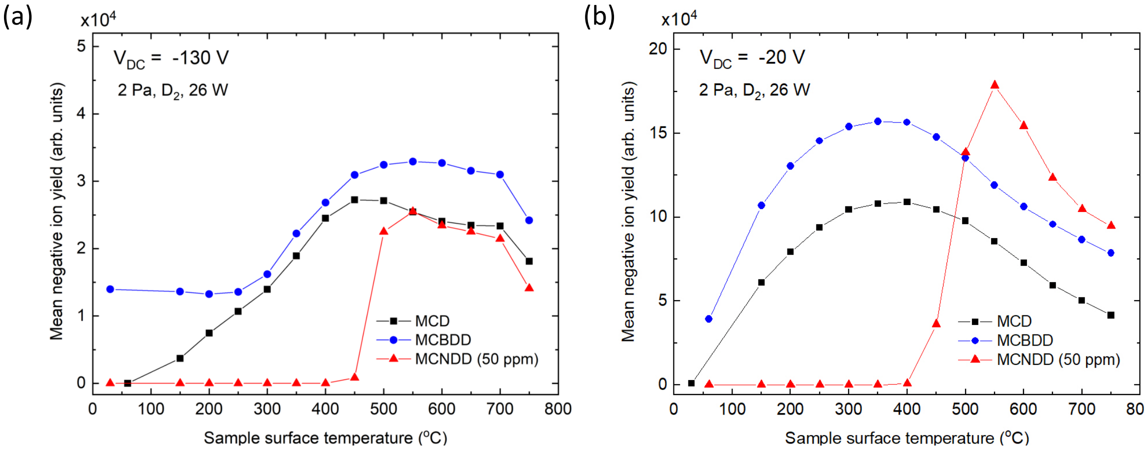

Figure 2.7: Negative ion yield with respect to film surface temperature for micro-crystalline diamond (MCD), micro-crystalline boron doped diamond (MCBDD) and micro-crystalline nitrogen doped diamond (MCNDD) for (a) $V_A = -130$ V and (b) $V_A = -20$ V. Low pressure deuterium plasma operated at 2 Pa and 26 W. Solid lines have been added to guide the eye.

In figure 2.7 (a), $V_A = -130$ V, the trends for MCD and MCBDD are similar, with an increase in yield by a factor of 6 from 150°C to 450°C observed for MCD and a factor of 2 observed for MCBDD from 150°C to 550°C. The yield then decreases gradually as temperature is increased further. These results are consistent with previous work using MCD and MCBDD[63]. The negative ion yield from MCNDD at sample temperatures below 400°C is effectively zero. After 400°C there is a rapid increase in yield by several orders of magnitude up to 550°C, as discussed in section 2.4. After 550°C, the trend agrees with MCD and MCBDD. In the high energy bombardment regime, the yield from MCNDD is found to be lower than MCBDD and comparable to MCD. This suggests that the higher positive ion bombardment energy is having a larger influence on MCNDD than MCBDD, though a mechanism for such a difference is beyond the scope of this study.

In figure 2.7 (b) for $V_A = -20$ V, the trends for MCD and MCBDD are also observed to be qualitatively similar, showing an increase in yield by a factor of 2 and a factor 1.5 from 150°C to 400°C respectively, and a gradual decrease in yield above 400°C, which has been discussed in section 2.4[63,82]. Figure 2.7 (b) has a similar trend as figure 2.7 (a) where the yield from MCNDD at temperatures below 400°C is effectively zero. The yield increases by several orders of magnitude between 400°C to 550°C, after which it decreases gradually. At temperatures above 550°C the general trend of decreasing yield is consistent with both MCD and MCBDD, and agrees with current understanding of these diamond films as discussed in the previous section. Of particular interest is that the yield for MCNDD in this low energy ion bombardment condition is observed to be higher than MCD, and also higher than the previously best performing type of diamond, MCBDD[63]. At 550°C, the maximum yield observed, MCNDD has a higher negative ion yield than MCD and MCBDD by a factor of 2 and 1.5, respectively. The higher yield observed when using MCBDD compared to MCNDD at temperatures below 550°C would suggest that for practical purposes, MCBDD would be preferable to MCNDD as the negative ion yield is observed to be highest at a lower temperature. However, if negative ions can be produced in the absence of conductivity, then it is possible that the negative ion yield from MCNDD at low energies would be higher than MCBDD from 30°C to 550°C. Therefore it is of interest to continue studying MCNDD and suggests that controlled addition of nitrogen during the growth of diamond using the PECVD process could be an avenue for increasing the negative ion yield from diamond.

2.8 Chapter summary

The results from this chapter demonstrate that the introduction of nitrogen doping to diamond can enhance the production of negative ions by a factor of 2 relative to un-doped diamond, achieved via the application of low energy positive ion bombardment to the surface. The amount of nitrogen doping in the samples is correlated to an increase in the negative ion yield, but only when a low-energy positive ion bombardment is used. This result suggests that the yield is sensitive to the energy of the ion bombardment and that reducing the formation of defects on the surface could lead to further increases to the yield.

Chapter 3

Pulsed sample biasing of nitrogen doped diamond for negative ion production with reduced surface defects

It was observed in the previous chapter that the production of negative ions from diamond can be enhanced through the introduction of nitrogen doping. However, the use of high-energy positive ion bombardment reduced the effect of the nitrogen doping which has been associated with the production of defects. In this chapter, a new higher density plasma source is used to increase the plasma density, whilst a pulsed sample bias has been utilised to lower the positive ion flux onto the surface. This reduction of the flux is useful to study the influence of the surface state of materials on the production of negative ions as the surface is expected to be preserved. However, a pulsed bias will lower the overall number of negative ions formed, which is an important consideration in the context of applications that require a large total current of negative ions. A comparison between nitrogen doped diamond and non-doped diamond is made and this demonstrates that the negative ion yield is higher for nitrogen doped diamond than non-doped diamond for all positive ion energies.

3.1 Experimental setup

The experimental setup that is used in this study is different to that used in the previous chapter. A higher density, inductively coupled plasma source is utilised, as well as synchronisation equipment necessary for the application of a pulsed bias to the samples. This is shown in figure 3.1, and described in detail below.

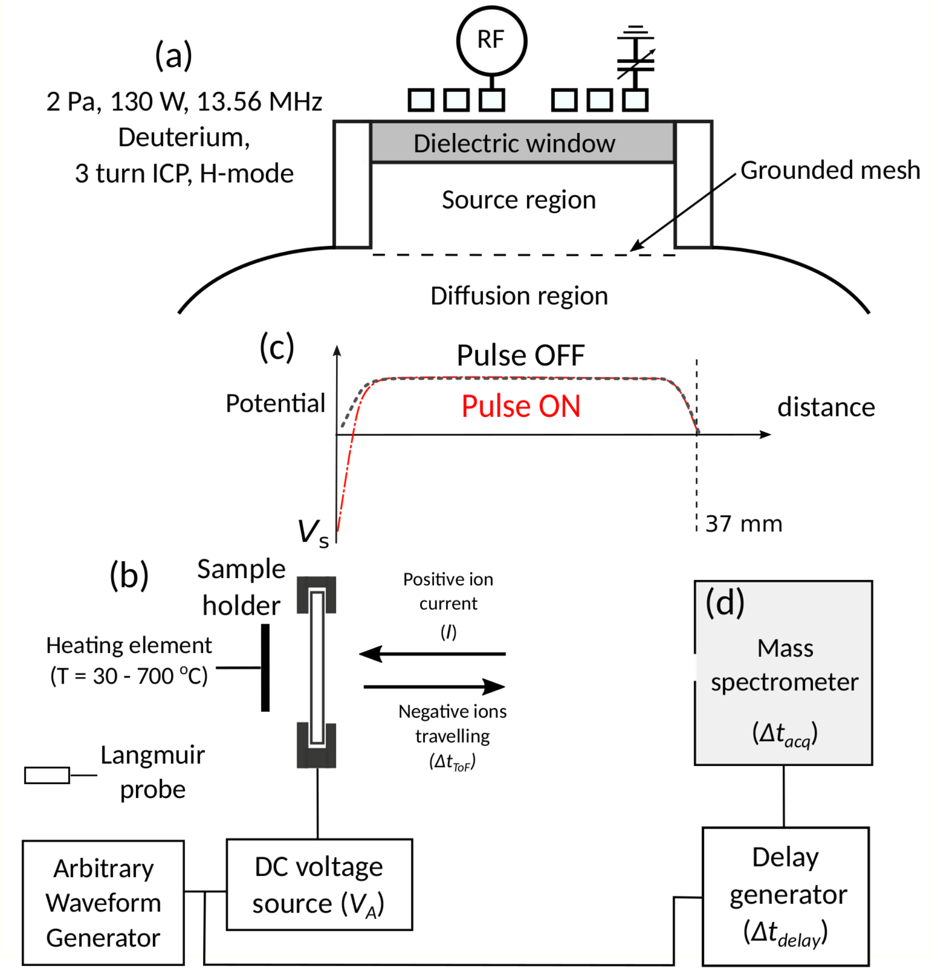

Figure 3.1: Schematic of the experimental setup. (a) Plasma source and diffusion chamber. (b) Sample holder with tungsten heating element and a Langmuir probe positioned behind the sample holder. (c) Representative plasma potential between the sample holder and the mass spectrometer. (d) Mass spectrometer and delay generator for measurements of the negative ion energy distribution function (NIEDF) with respect to time within the sample bias pulse.

3.1.1 Plasma source and diffusion chamber

The reactor consists of a cylindrical plasma source (100 mm height and 150 mm diameter), which is separated from a spherical diffusion chamber (200 mm diameter) by a grounded mesh (285 µm spacing, hole size 200 µm). The grid reduces radio-frequency (RF) plasma potential fluctuations in the diffusion chamber, which would otherwise alter the shape of the negative ion energy distribution functions (NIEDFs) measured by the mass spectrometer[76].

A low-pressure inductively coupled deuterium plasma was generated using an RF power generator (Huttinger PFG 1600 RF) attached to a matchbox (Huttinger PFM 3000 A). Power is coupled to the plasma through a 3 turn copper coil positioned on top of a dielectric ceramic window (150 mm diameter). The effective power coupled to the plasma was 130 W as measured by the generator.

The pressure in the diffusion chamber was maintained at 2 Pa as measured using a Baratron gauge (MKS) using a mass flow controller (7.6 sccm, BROOKS 5850TR) and a 150 mm diameter Riber gate valve installed in front of a turbo molecular pump (Alcatel ATP400). These experimental conditions were selected to reduce the ion bombardment of the samples between application of negative bias and so limit their degradation during the course of the experiment.

3.1.2 Deuterium plasma characteristics

Measurements of the deuterium plasma potential, electron temperature and density were made using a Langmuir probe (Smart probe from Scientific Systems)[159] within the diffusion chamber as shown in figure 3.1. It was not possible in this experimental campaign to position the Langmuir probe in front of the sample, meaning measurements were made in a position close to the centre of the diffusion chamber to give a representative indication of the plasma properties within the chamber.

The Langmuir probe was RF compensated, with a cylindrical tungsten probe tip of length 6.5 mm and 110 µm radius. The tip was cleaned prior to each measurement by biasing it with a high positive voltage to heat the probe tip and vaporise any impurities. Measurements were undertaken to determine the representative values of the electron density, $(2.5 \pm 0.5)\times10^{9}$ cm^{-3}, electron temperature, (0.6 ± 0.5) eV, and the plasma potential, (2.6 ± 0.1) V which suggest that the sheath width adjacent to the sample surface is roughly 1 mm and 2 mm for sample biases of -20 V and -130 V, respectively[2].

3.1.3 Sample temperature control

Figure 3.1 (b) shows a schematic of the temperature controlled sample holder. This was described in detail in the previous chapter 2. The procedure for checking alignment of the samples to the mass spectrometer is repeated in these experiments.

The temperature of the sample surface was determined by comparing the temperature measured using the PID with the temperature measured by a thermocouple attached to the front of a calibration sample. This is expected to introduce an uncertainty of ±20°C for all temperature measurements.

3.1.4 Measurement of negative ion energy distribution functions

Figure 3.1 (c) shows a plasma potential profile that can be reasonably expected in the space between the sample surface and the mass spectrometer. When a bias (V_A) is applied to the sample, the voltage on the sample surface (V_S) decreases, accelerating positive ions onto the sample surface. Negative ions that are produced due to the positive ion bombardment are accelerated by the negative bias such that they then cross the 37 mm gap separating the sample surface and the mass spectrometer. The mass spectrometer is then used to measure an NIEDF[139].

The relatively low gas pressure of the plasma limits ion-neutral collisions within the diffusion chamber[138]. Any collisions that occur between the negative ions produced at the sample surface and the background gas are assumed to cause detachment, resulting in the destruction of the negative ion[36,139]. The negative ions formed through volume production processes are prevented from entering the mass spectrometer due to the plasma potential in front of the mass spectrometer orifice. This means that only negative ions created through surface production on the sample surface are measured[138,139].

The mass spectrometer is shown in figure 3.1 (d). This was used to measure the ratio of the positive ions that make up the deuterium plasma, giving a ratio of (92.6 ± 3.4)% D_3^+ ions, (0.25 ± 0.04)% D_2^+ ions and (7.2 ± 3.5)% D^+ ions, where the uncertainty corresponds to the day-to-day variance during the experimental campaign. The measurement uncertainty of the plasma composition due to the influence of the internal settings of the mass spectrometer may be higher[139].

In a similar manner to chapter 2 the influence of positive ion energy on the negative ion yield when using a pulsed bias is compared. Two positive ion bombardment energies are considered. A "high-energy" bombardment regime using an applied bias of -130 V, and a "low-energy" regime using a bias of -20 V. The plasma is measured as being primarily composed of D_3^+ ions, resulting in a positive ion energy bombardment of 44 eV/nucleon and 8 eV/nucleon for a negative bias of -130 V and -20 V respectively[138]. The Langmuir probe measurements in section 3.1.2 suggest that the sheath width is smaller than the ions and neutrals mean free path. It is therefore reasonable to suggest that the positive ions undergo minimal collisions when passing through the sheath.

As previously described in chapter 2, the positive ions bombard the sample surface to produce negative ions. These are then detected by the mass spectrometer, producing an NIEDF. Once the measurement has been completed, the NIEDF can be shifted to account for the energy the negative ions possessed when they were formed. This is possible because the total negative ion energy, according to equation 2.1, is conserved[138].

3.1.5 Micro-crystalline diamond samples

Micro-crystalline diamond (MCD) films were prepared using plasma enhanced chemical vapour deposition (PECVD) as described in Ref. 143. New nitrogen doped diamond films were produced using a similar PECVD technique to the MCD samples and reported on in chapter 2[86]. The PECVD process utilised a bell jar reactor with a pressure of 200 mbar, microwave power at 3 kW, a substrate temperature of 850°C, and a background hydrogen gas mixture with a methane concentration of 5%. The ratio of nitrogen in the gas mixture was set as a means to vary the concentration of nitrogen in the MCNDD film. Each film was deposited on to a (100) oriented silicon wafer.

In chapter 2, the nitrogen introduced in the gas phase was correlated to the nitrogen content in the samples via Raman spectroscopy[86] which has been confirmed again for this study.

The gas phase content of the MCNDD sample used in this study was 50 ppm. In chapter 2, it was observed that this concentration of doping resulted in the highest negative ion yield[86].

3.1.6 Negative ion yield using pulsed and continuous substrate biasing

The negative ion yield is used as a means to compare the production of negative ions between samples, applied voltages and biasing techniques. This has been previously defined in chapter 2, section 2.2.

3.1.6.1 Electrical conditions for pulsed sample biasing

As described in section 3.1.4, a surface bias is required to accelerate positive ions towards the sample surface. Pulsed biasing was undertaken to generate the necessary electric field at the surface of non-conductive samples, as shown in figure 3.2.

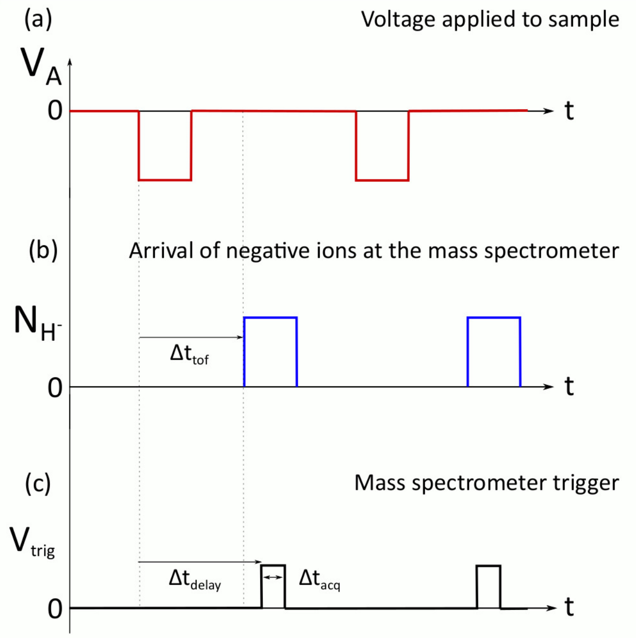

Figure 3.2: Timing diagram for an NIEDF measurement for pulsed bias operation. (a) Voltage applied to the sample (V_A) generates an electric field that causes positive ion bombardment and accelerates newly created negative ions towards the mass spectrometer. (b) Negative ions travel from the sample to the mass spectrometer detector, arriving after a flight time, Δt_{tof}. (c) Measurement trigger voltage pulse (V_{trig}) sent from delay generator, shown in figure 3.1, initiates a measurement of length Δt_{acq} by the mass spectrometer.

In figure 3.2 (a), a negative bias is applied to the sample (V_A) through the use of a waveform generator and DC voltage source, shown previously in figure 3.1 (b). The negative voltage on the sample surface accelerates positive ions towards the sample and negative ions towards the mass spectrometer. The time of flight (Δt_{tof}) for these negative ions is shown in figure 3.2 (b) and was measured to be approximately 14.5 µs or 15.5 µs when operating with "high" and "low" energy positive ion bombardment, respectively. The delay generator, shown in figure 3.1 sends a trigger to the mass spectrometer after time $\Delta t_{\mathrm{delay}}$, for a duration corresponding to Δt_{acq}. The time $\Delta t_{\mathrm{delay}}$ accounts for the time of flight (Δt_{tof}) of the negative ions from the samples to the mass spectrometer detector and is adjusted so that a NIEDF measurement, with a duration of Δt_{acq}, is acquired within the negative ion pulse arriving at the mass spectrometer as shown in figure 3.2 (c).

The creation of negative ions on an insulating surface through positive ion bombardment causes the accumulation of positive charge on the sample surface[83]. The build up of positive charge changes the voltage on the surface (V_S) over the duration of the pulse, and therefore alters the energy that the negative ions possess when they are measured by the mass spectrometer[83]. If the pulse cycle is too high, the positive ion charge that is built up during the "on" phase of the pulse will not dissipate before the next pulse[83]. Therefore a sufficiently small duty cycle is utilised to allow for the positive charge to dissipate between pulses. To determine the rate of positive charge build up, a series of NIEDFs were taken with increasing $\Delta t_{\mathrm{delay}}$ where the sample was biased using a square waveform pulse at a frequency of 1 kHz, an amplitude of negative -130 V and duration of 32 µs (3.2% duty cycle). The NIEDFs, shown in figure 3.3, are generated using an insulating un-heated MCD sample with measurement duration ($\Delta \mathrm{t}_{\mathrm{acq}}$) of 2 µs.

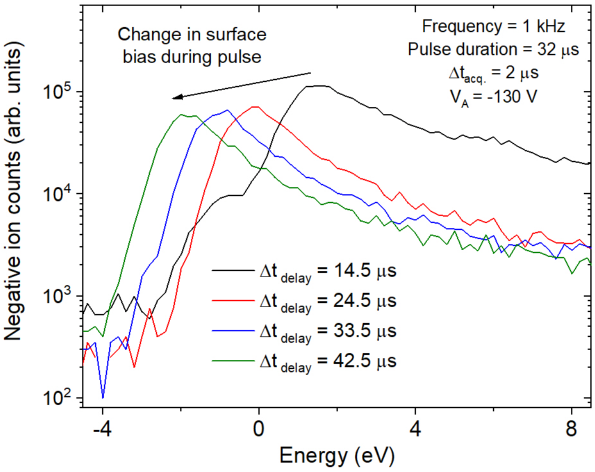

Figure 3.3: NIEDFs measured for pulsed-bias operation of an un-heated MCD sample with respect to the delay time between the application of the bias voltage and negative-ion measurement trigger, $\Delta t_{\mathrm{delay}}$. Bias voltages are applied at 1 kHz with a duration of 32 µs and applied voltage of -130 V. Low pressure deuterium plasma is operated at 2 Pa and 130 W.

In figure 3.3, increasing $\Delta t_{\mathrm{delay}}$ results in a shift in the peak of the NIEDF towards lower ion energies. This is because as $\Delta t_{\mathrm{delay}}$ increases, the surface bias V_S starts to increase due to a build up of positive charge on the non-conductive surface. The value V_S, when using a conductive sample, can be assumed to be equivalent to V_A. Therefore, in equation 2.2, V_S can be substituted with V_A and the NIEDFs for a conductive sample can be presented in terms of E_k by rearranging equation 2.1[139]. The sample in figure 3.3 is non-conductive, which means that V_S and V_A become increasingly divergent, with V_S increasing over the duration of the applied pulse. This results in the observed shift in figure 3.3 where the negative ion energy peak moves in response to an increase in Δt_{delay}[83].

Changes in V_S during Δt_{acq} resulting in a "smeared" NIEDF are avoided by utilising a short Δt_{acq}. Figure 3.3 demonstrates that a change in the surface voltage of 0.1 V µs^{-1} can be expected for insulating samples when using a duty cycle of 3.2%. Δt_{acq} was chosen to be 2 µs due to this being the longest time over which a change in the surface voltage on an insulating sample would be below the resolution of the mass spectrometer, thus maximising the negative ion signal, while minimising the shift in the surface voltage during the acquisition.

The pulse condition that was chosen for this work was a square waveform with a 5 kHz frequency and 6 µs duration (duty cycle 3%), which was selected to minimise the accumulation of positive charge on an insulating surface and therefore enable a reasonable comparison with samples that are conductive.

3.1.7 Measurement of the positive ion current bias

The positive ion current is again determined using a copper electrode inserted into the sample holder in place of a diamond sample, as described in chapter 2.

3.1.7.1 Continuous bias operation

The current drawn from the plasma was measured using an ammeter. This was done without any heating applied to the electrode because the Kapton tape is thermally sensitive. Variations in the current to the sample due to increases in its temperature are expected to be approximately 5 %, as determined from separate measurements of the current to the sample holder[86].

The current to the sample at an applied voltage of -20 V was 14.5 µA, at -130 V the current increased to 18 µA. The expected sheath width is approximately 1 mm or 2 mm, as determined using Langmuir probe measurements described in section 3.1.2 for a -20 V and -130 V bias voltage respectively. This is much smaller than the size of the sample holder, which has a side length of 3 cm. Therefore the sheath is expected to be approximately planar across the surface of the sample.

3.1.7.2 Pulsed bias operation

In pulsed bias operation, the instantaneous positive ion current was determined using the same setup as described previously in section 2.2.1, with a copper electrode inserted into the sample holder in place of a sample. To achieve the measurement of a time resolved sample current, a homemade device based on a fast trans-impedance circuit was used to convert the positive ion current from the sample into a voltage trace that is observed on an oscilloscope (Teledyne LeCroy Wavesurfer 4mXs-B). The current within a pulse was first measured with the plasma on, and then with the plasma off to account for leakage currents through the parasitic capacitance of the cables. The "real" sample current was obtained by subtracting the plasma off measurement from the plasma on measurement. A conversion factor was then applied to determine the current from the measured voltage. Representative measurements of the applied voltage and positive ion current to the sample, and corresponding time-resolved negative ion yield, are shown in figure 3.4.

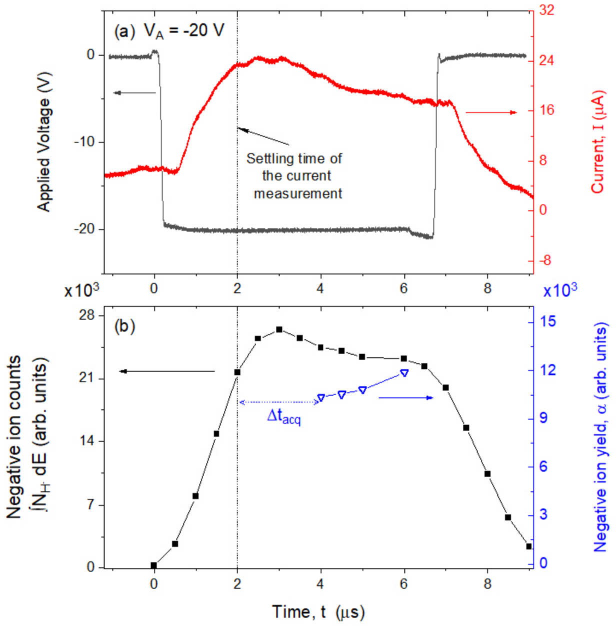

Figure 3.4: (a) Voltage applied to sample holder and copper electrode with corresponding positive ion current. (b) Negative ion counts measured with incrementally increasing Δt_{delay} for a Δt_{acq} of 2 µs. In (b), Δt_{acq} is shown for the first data point of the negative ion yield measurement at t = 4 µs. Low pressure deuterium plasma is operated at 2 Pa and 130 W. Solid lines have been added to guide the eye.

Figure 3.4 (a) shows the time-resolved applied voltage and positive ion current. The voltage that is applied to the sample is measured to be -20 V with little observed change during the application of the bias.

The settling time of the electrical measurement setup is determined to be 2 µs by replacing the electrode with a resistor outside of the plasma chamber and applying a voltage to the circuitry. This means that current measured between the application of the bias in figure 3.4 at 0 µs and 2 µs is considered to be unreliable due to the rapid change of the system at $t = 0$ µs. When the bias is removed from the system at $t = 6$ µs, the system does not respond promptly, causing a brief increase in the applied bias. This means that the period of time where the positive ion current can be reliably interpreted is between t = 2 µs and t = 6 µs, as shown in figure 3.4. During this interval, the current is observed to decrease over the duration of the pulse. A higher positive ion current going into the sample during the first few micro-seconds of a pulsed bias is consistent with observations that the current decreases over a time to a similar value observed when using a continuous sample bias. Therefore, the higher current observed when using a pulsed bias compared to a continuous bias is considered to be due to local changes in the plasma as a result of the periodic changes in the voltage of the sample and sample holder.

Figure 3.4 (b) shows the time-resolved negative ion counts detected during the bias pulse and the corresponding negative-ion yield, as determined with equation 2.2, for MCD at 550°C. This temperature is chosen because previously in chapter 3, a temperature of 550°C produced the highest number of negative ions, whilst also ensuring that the sample is fully conductive[86].

Starting at t = -1 µs, the negative ion counts increase over the duration of the pulse, reaching a peak that roughly aligns with the measured peak in the positive ion current, shown in figure 3.4 (a). After this peak the counts decrease by 3×10^3 over the duration of the pulse, before decaying to zero after t = 6 µs. The measurement of the negative ion counts takes place over an acquisition window, Δt_{acq} = 2 µs, whilst in figure 3.4 (a) it is observed that the current changes by approximately 5 µA over the course of Δt_{acq}. An average of the current during the measurement period Δt_{acq} is therefore used to determine the negative ion yield to minimise error that may be introduced by any misalignment of the count measurements to the current measurement.

To compare the relative ion yield between samples, a consistent temporal position in the negative ion pulse is chosen; at 3 µs encompassing a Δt_{acq} window between 2 µs and 4 µs, as shown in figure 3.4 (b). This period was chosen as it is the earliest point in time that the current can be determined, thus minimising the build up of positive ions on the surface of the samples.

3.2 Negative ion yield: comparison of MCD and MCNDD for pulsed and continuous biasing

Figure 3.5 shows the negative ion yield measured using MCD and MCNDD for “high-energy” and “low-energy” positive ion bombardment conditions in continuous and pulsed sample bias operation.

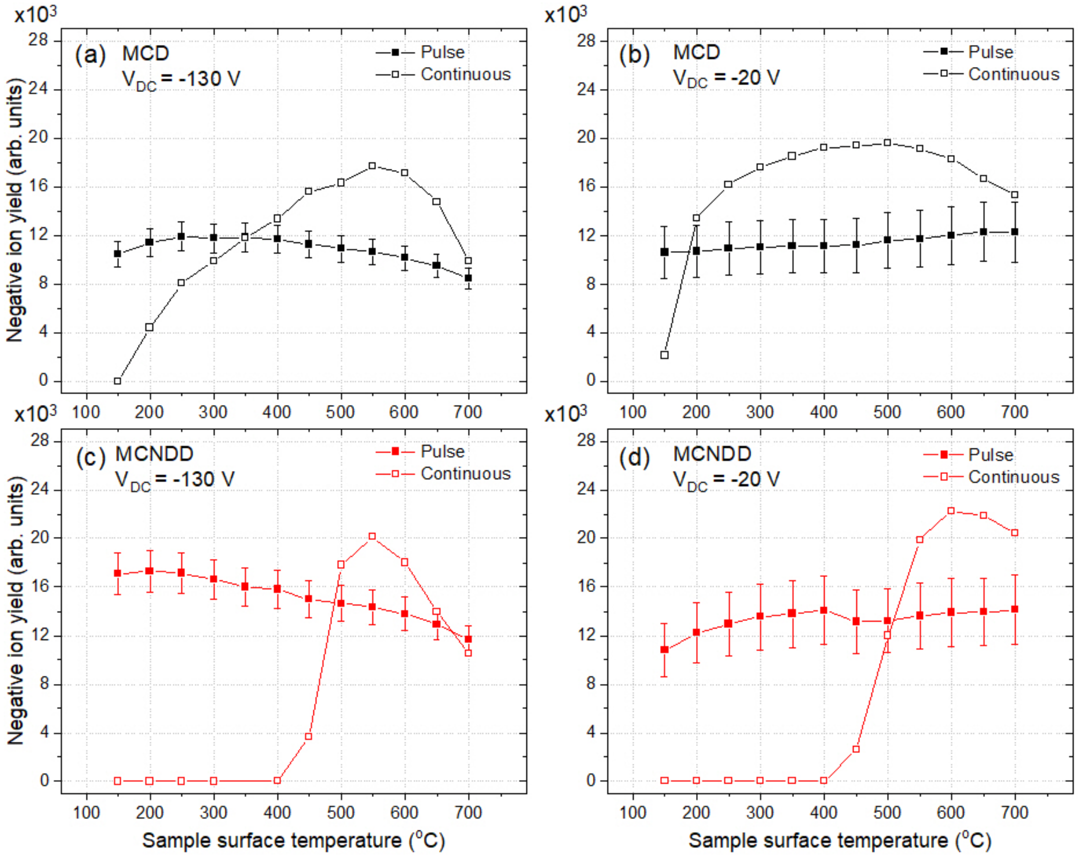

Figure 3.5: Negative ion yield with respect to temperature of the sample surface for continuous and pulsed biased operation. (a) MCD with a bias of −130 V (b) MCD with a bias of −20 V (c) MCNDD with a bias of −130 V (d) MCNDD with a bias of −20 V. Uncertainty bars of 10% and 20% have been included for the pulsed bias yield measurements at -130 V and -20 V respectively to account for the uncertainty in the current measurements in each respective case. Low pressure deuterium plasma is operated at 2 Pa and 130 W. Solid lines are included as a visual guide.

Uncertainty bars have been included in the pulsed bias case to account for the change in the current during the 2 µs acquisition interval, Δt_{acq}.

3.2.1 Negative ion yield for continuous bias operation

In figure 3.5 (a) the negative ion yield for MCD is observed to increase up to 17.6×10^3 as the sample temperature is increased from 150°C to 550°C when using a -130 V continuous sample bias. This is then followed by a decrease in the yield from 17.6×10^3 to 9.8×10^3 as the temperature is increased from 550°C to 700°C.

In figure 3.5 (b) when using a -20 V bias, the trend of increasing yield with increasing sample temperature is similar to that observed in figure 3.5 (a), it increases from 2×10^3 to 20×10^3 as the temperature increases from 150°C to 500°C, and then decreases to a yield of 15×10^3 from a sample temperature of 500°C to 700°C.

The negative ion yield from MCNDD samples is shown in figures 3.5 (c) and (d). When using a continuous sample bias, at sample temperatures below 400°C the yield from MCNDD cannot be measured due to the poor conductivity of the sample. Once the MCNDD sample temperature reaches 400°C, negative ions are measured and a peak in the negative ion yield of 20×10^3 at 550°C is observed in figure 3.5 (c) when using a sample bias of -130 V. Similarly, a negative ion yield of 22×10^3 at 600°C is observed in figure 3.5 (d) when using a sample bias of -20 V. The changes in the negative ion yield when using a continuous sample bias for MCNDD and MCD at temperatures above 550°C are similar to results of previous work[86]. The peak negative ion yield from MCNDD is about 10% higher than MCD for a -20V bias, which is also consistent with previous work[86].

Differences between the samples and biasing methods can be observed in figure 3.5 and the corresponding NIEDFs, which are used to determine the negative ion counts coming from the samples. The distribution of negative ions in the NIEDFs have previously been shown to be useful for determining the negative ion production mechanisms involved when using carbon samples in chapter 2.

Of the two production processes, sputtering is temperature dependent because it relies on the presence of adsorbed deuterium on and within the sub-surface lattice of the diamond samples. Increasing the sample temperature reduces the adsorption of deuterium and encourages out-gassing into the diamond lattice, thus reducing the amount of sputtering that can occur[76,78,138].

Changes in the proportion of negative ions produced by the two production processes can be observed by considering the NIEDFs produced by samples at different temperatures. Figure 3.6 shows the NIEDFs for MCD at temperatures of 250°C, 400°C, 600°C and 700°C.

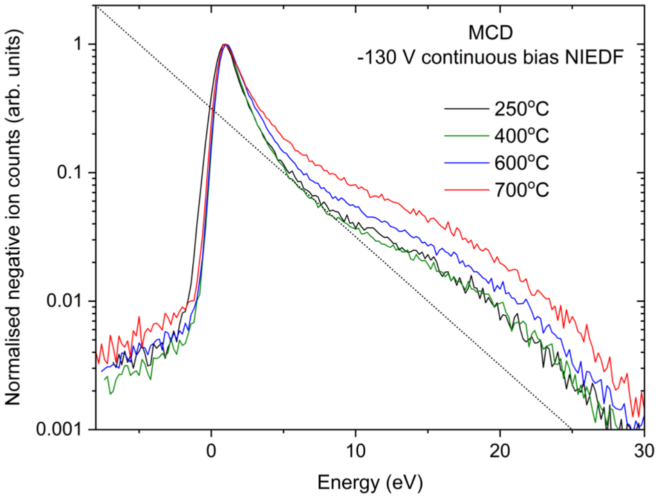

Figure 3.6: NIEDF measurements for MCD at sample temperatures of 250°C, 400°C, 600°C and 700°C using a bias of -130 V, applied continuously. Dotted reference line added to guide the eye. Low pressure deuterium plasma is operated at 2 Pa and 130 W.

In figure 3.6, the NIEDFs shown have been normalised to the peak negative ion counts.

In previous work, it was observed that the proportion of negative ions produced through sputtering processes was higher at lower negative ion energies than at higher energies[160]. This means that, due to the normalisation of the NIEDFs, a change in the tail height can be used to infer the relative proportion of backscattering compared to sputtering, which in turn is used to infer the amount of sub-surface deuterium that is in the samples[76,85,160]. It is observed that the tail of the NIEDFs in figure 3.6 rises as sample temperature is increased. When combined with observations in figure 3.5 (a) and (c) that show a decrease in the negative ion yield at temperatures above 550°C for both MCD and MCNDD, it demonstrates that a reduction in the adsorbed deuterium within the sample decreases the negative ion yield from the samples. This observation is consistent with previous work[76,86,160]. A similar comparison cannot be carried out using the NIEDFs produced using a -20 V bias as the NIEDFs in this case do not have a high energy tail. However, it is reasonable to suggest that a similar process occurs when using a -20 V bias as the negative ion yield decreases in a similar manner when using a continuous sample bias past a sample temperature of 500°C and 600°C for MCD and MCNDD respectively.

As shown in figure 3.5 (a) and (b), when applying a continuous bias to MCD, the negative ion yield increases as the temperature of the sample is increased from 150°C to 550°C. This is consistent with previous work and has been attributed to a coupled process of defect formation, where the diamond sp3 bonds are turned to sp2 bonds by the bombarding positive ions from the plasma, and then the preferential etching away of these newly created sp2 bonds[76,82,161]. Surfaces that are composed mostly of sp2 bonds have previously been associated with a reduction in the negative ion yield. Therefore the creation of these bonds has previously been expected to decrease negative ion yield if too many exist on a diamond surface[76]. By increasing the temperature of the samples, the rate at which the sp2 bonds are etched away will be increased resulting in a reduction in the number of defects on the surface at higher sample temperatures, and thus a higher negative ion yield from samples that are heated[76,82,161]. This process is observed to cause a peak in the negative ion yield at a temperature of approximately 550°C for MCD, before the higher temperature of the samples causes a reduction in the sputtering contribution.

Previous work has demonstrated that a higher positive ion energy is associated with an increase in the amount of defects on the sample surface[76,82]. This is observed in figure 3.5 (a) and (b) when comparing the negative ion yield between a sample bias of -130 V and -20 V, respectively. A "high-energy" positive ion bombardment will produce more defects. At lower sample temperatures, when using a"high-energy" positive ion bombardment, the defects are not etched away and so a lower negative ion yield is observed due to a larger proportion of sp2 bonds. Increasing the temperature of the sample will increase the negative ion yield as the defect bonds are etched away more rapidly. This results in a lower negative ion yield from MCD at temperatures between 150°C and 550°C when using a "high-energy" (V_A = -130 V) positive ion bombardment compared to a "low-energy" (V_A = -20 V) positive ion bombardment across the same temperature range. This also means that a higher peak negative ion yield for a low energy positive ion bombardment can be expected, as the number of defects is reduced when using a "low-energy" positive ion bombardment. This is observed in figure 3.5 (b) at 500°C which is higher that the peak in the negative ion yield at 550°C in figure 3.5 (a).

In figure 3.5 (c) and (d), the negative ion yield from MCNDD is observed to decrease with respect to sample temperature at a similar rate to MCD at applied biases of -130 V and -20 V. A similar comparison to MCD cannot be made at temperatures below 550°C as addition of nitrogen doping lowers the conductivity of the diamond such that the negative ion yield cannot be measured at sample temperatures below 550°C.

3.2.2 Negative ion yield for pulsed bias operation

In figure 3.5 (a), the negative ion yield from MCD when using a pulsed sample bias of -130 V increases as the sample temperature is increased from 150°C to 250°C by 1.4×10^3 and then decreases as the sample temperature increases from 250°C to 700°C by 3.4×10^3. This is unlike the trend observed in figure 3.5 (b), where the negative ion yield, when using a pulsed bias of -20 V, increases as sample temperature is increased from 150°C to 700°C by 1.7×10^3.

The negative ion yield from MCNDD using a pulsed sample bias is shown in figures 3.5 (c) and (d) for -130 V and -20 V sample bias voltages, respectively. Using a pulsed bias, negative ions are produced at temperatures lower than 450°C, compared to when operating with a continuous sample bias. In figure 3.5 (c), the negative ion yield is shown to decrease by 5.4×10^3 as the sample temperature is increased from 150°C to 700°C. In contrast to this, in figure 3.5 (d) it is observed that the negative ion yield increases by 3.4×10^3 as sample temperatures are increased from 150°C to 400°C when using a pulsed sample bias of -20 V.

In figure 3.5 (a) and (b) when using a pulsed sample bias, it is observed that there is a comparatively small change in the negative ion yield as sample temperature is increased, which is in contrast to the large change in negative ion yield observed when using a continuous sample bias between sample temperatures of 150°C to 500°C. As described in section 3.2.1, the negative ion yield from diamond is influenced by the number of sp2 defects formed by bombarding positive ions. As the sample temperature is increased, sp2 defects are etched at an increased rate. This means that the negative ion yield from a sample is expected to increase as the sample temperature is increased, as is observed when using a continuous bias. When using a pulsed -130 V sample bias, as shown in figure 3.5 (a), the negative ion yield peaks at a lower sample temperature compared to when using a continuous sample bias, at 250°C, and then decreases as the sample temperature is increased. When using a pulsed sample bias case, if little to no defects are formed on the sample surface, the influence of temperature on the negative ion yield due to preferential etching will be reduced and only a decrease in the sputtering contribution will be observed. As there is a comparatively small change in the negative ion yield observed when using a pulsed sample bias compared to a continuous sample bias at -130 V, it can be confirmed that the sample surface is being preserved when using this technique, and that the pulsed sample bias measurements are representative of an almost "pristine" sample surface[83].

By using a pulsed sample bias, it is possible to compare the negative ion yield from the pristine surface states of MCNDD and MCD at temperatures between 150°C and 700°C, as well as generate and measure negative ions in spite of the low conductivity of MCNDD at temperatures below 400°C. The negative ion yield from MCNDD is observed to be, on average, higher than MCD by 28% at -130V and 14% at -20V across the compared temperatures. This supports previous work that observed that negative ion yield from diamond is enhanced when nitrogen doping is added to diamond samples and suggests that the surface state of MCNDD is conducive to enhanced negative ion yield.

A series of NIEDFs when using a pulsed sample bias of -130 V and a MCD sample are shown in figure 3.7 for sample temperatures of 250°C, 400°C, 600°C and 700°C.

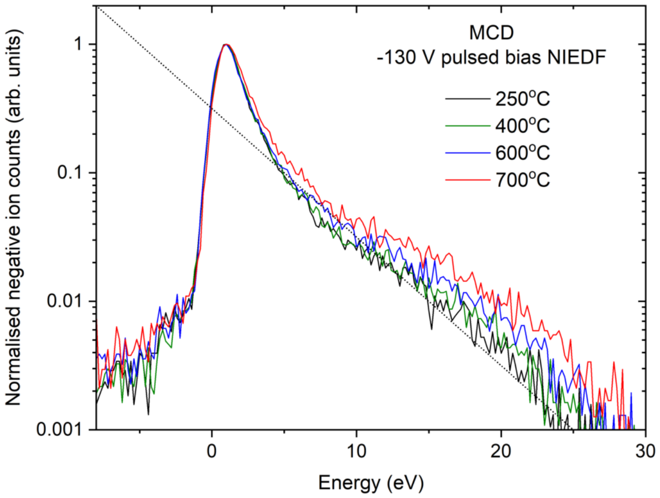

Figure 3.7: NIEDF measurements for MCD at sample temperatures of 250°C, 400°C, 600°C and 700°C using a pulsed bias of -130 V. Dotted reference line added to guide the eye. Low pressure deuterium plasma is operated at 2 Pa and 130 W.

It can be observed in figure 3.7 that there is a smaller change in the tail height when compared to figure 3.6, suggesting a smaller change in the sputtering contribution to the negative ion yield as the sample temperature is increased over the same range of temperatures.

The negative ion yield in figure 3.5 (a) when applying a pulsed bias is observed to decrease as the temperature of the MCD sample is increased from 200°C to 700°C. This observation is consistent with the observed changes in the tail height in figure 3.7. There is an increase in the tail height as the sample temperature is increased suggesting a similar decrease in the sputtering contribution that reduces the negative ion yield from the sample as sample temperature is increased.

Using the dotted reference lines in figures 3.6 and figure 3.7 as a guide, we qualitatively compare the tail heights for pulsed and continuous sample biasing. By comparing the tail heights in these figures, it is observed that the amount of sputtering from a pulsed sample bias appears to be larger than that observed when using a continuous sample bias. This is consistent with previous work which suggested that a non-continuous flux of positive ions allows for the re-adsorbtion of deuterium lost through the sputtering process when the sample bias is being applied that would otherwise be depleted when utilising a continuous sample bias[83]. It can also be observed that the increase in the tail height between a sample temperature of 600°C and 700°C, is much larger in figure 3.6 than in figure 3.7. This agrees with the larger decrease in the negative ion yield observed in figure 3.5 (a) between 600°C and 700°C when using a continuous sample bias compared to when using a pulsed sample bias.

For the same reason as the continuous sample biasing case, it is not possible to compare the NIEDFs for -20 V pulsed sample biasing to determine the sputtering contribution due to the lack of a high energy tail in the NIEDF. This means that the sputtering contribution from these samples is inferred by considering the NIEDFs using a -130 V bias and the trends observed in figure 3.5. As sample temperatures are increased, a decrease in the sputtering contribution can be expected as the adsorbed deuterium is out-gassed from the samples[76]. This is observed to be the case for MCD and MCNDD in figure 3.5 (a) and (c) when using a -130 V pulsed sample bias. It is observed that the negative ion yield from MCD decreases as the sample temperature is increased from 150°C to 700°C by 28% and by 41% for MCNDD over a similar temperature scale. This is in contrast to the observations in figure 3.5 (b) and (d) for MCD and MCNDD when using a -20 V pulsed sample bias. It is observed that the negative ion yield increases by 13% over a similar temperature range for MCD and by 24% for MCNDD. Previous work has suggested that the deuterium content of the samples is comparable at similar sample temperatures[76,86]. Therefore the increase in the negative ion yield as the sample temperature is increased suggests that when utilising both a "low" positive ion energy and a pulsed sample bias, the contribution of sputtering to the overall negative ion yield is reduced or even absent.

To explain the mechanism for a reduced sputtering contribution with a "low-energy" pulsed positive ion bombardment, it is worth considering previous work and differences in the negative ion yield at sample temperatures above 500°C when using a continuous sample bias. Previous studies have determined that the threshold energy for the sputtering of hydrogen from carbon occurs at approximately 15 eV[82]. As previously described in section 3.1.2, the sheath of the plasma in front of the samples can reasonably be expected to be collision-less. Therefore, the modal energy (E_M) of the dominant positive ion, ${D_3}^+$, upon impact with the sample surface will have an energy of approximately 8 eV when using a -20 V bias, as

$E_M = \mathrm{e}(V_S + V_p)/3$[82]. This is below the calculated threshold for sputtering, suggesting that only a small amount of sputtering can occur when using a -20 V bias, where the lighter positive ions (D_2^+ and D^+) are able to exceed the threshold energy. An issue with this interpretation is that in figure 3.5 (b), when utilising a continuous sample bias of -20 V, the negative ion yield is observed to decrease as sample temperature is increased from 500°C to 700°C which is consistent with a reduction in the sputtering contribution from the samples, despite the positive ion energy being below the threshold for sputtering to occur. The difference between these two cases is the type of sample biasing being used. Therefore, this observation suggests that the use of a -20 V pulsed sample bias reduces the contribution of sputtering to the negative ion yield and is possibly linked to defect formation caused by a continuous positive ion bombardment.

It is interesting to note that the negative ion yield observed when using a -20 V pulsed sample bias for MCD and MCNDD (figure 3.5 (b) and figure 3.5 (d), respectively) is similar at similar sample temperatures, compared to MCD and MCNDD when using a -130 V pulsed sample bias (figure 3.5 (a) and figure 3.5 (c), respectively). This suggests that the when using a pulsed sample bias, the surface state of the samples is similar despite the differences in the applied voltages. This further supports the argument that the pulsed bias preserves the surface state of the samples.

3.2.3 Comparing the negative ion yield between pulsed and continuous bias operation

In figure 3.5 (a) and (b), when using a -130 V and -20 V continuous sample bias respectively with MCD, the negative ion yield is observed to be almost 1.6 times higher than that observed from a similar sample when applying a -130 V pulsed sample bias at a sample temperature of 550°C. Similarly for MCNDD, in figure 3.5 (c) and (d), the negative ion yield is observed to be 1.4 times higher when using a continuous bias compared to when applying a pulsed sample bias at a sample temperature of 550°C. In addition to this, the differences between the pulsed and continuous sample bias appears to be consistent between all of the samples. This suggests that a similar mechanism for negative ion formation exists between each of the samples.

Previous work observed that a pulsed bias produced a higher number of negative ion counts (N_{H^-}) from diamond samples and attributed this to a preserved surface state[83]. This was based on the assumption that a pristine surface state composed primarily of sp3 is an ideal surface state for negative ion production from diamond, as discussed in section 3.2.1. However, in the previous work a measurement of the positive ion current within the pulse was not available in order to confirm that negative ion yield is higher with a pristine surface[83].

The observation of a lower negative ion yield when using a pulsed sample bias compared to a continuous one means it is reasonable to suggest that there is a change in the surface state of the samples that occurs as a result of the positive ion bombardment. This is because, as the pulse bias duty cycle is increased, the time the bias is applied to the sample will increase and will eventually be equivalent to a continuous sample bias, meaning the yield must increase as the pulse duration is increased. There are two proposed mechanisms that could be responsible for a change in the surface state of the sample and therefore a change in the negative ion yield. One is a change in the adsorbed deuterium which is responsible for sputtering from the samples, and the other is an increase in the number of sp2 bonds created on the sample surface that the pulsed sample bias reduces.

As described previously, the deuterium content of the samples is higher when using a pulsed sample bias, as observed when comparing the tail heights in figures 3.6 and figure 3.7. If the deuterium content of the sample is reduced, the negative ion yield is expected to be reduced[76]. Therefore, if it is observed that there is a decrease in the sputtering contribution when using a continuous sample bias compared to a pulsed sample bias, it suggests that the sputtering contribution is changing when going between a pulsed and continuous sample biasing and this is unlikely to be responsible for higher negative ion yield observed when using a continuous bias.

The alternative explanation is that the negative ion yield is higher when using a continuous sample bias due to the bombardment of the sample surfaces creating sp2 defect bonds. Previous work has shown that a surface composed entirely of sp2 bonds is detrimental to negative ion yield[76], meaning techniques to preserve the surface of diamond and minimise the number of sp2 bonds has been of interest[83]. However, in this study the evidence suggests that some degree of defect formation is important for increasing the negative ion yield from diamond. As a result of this observation, the optimum sp2 to sp3 ratio is expected to be at a sample temperature between 450°C and 550°C when using a continuous sample bias. When using a lower sample temperature the sp2 to sp3 ratio is expected to be higher, whilst using pulsed bias the sp2 to sp3 ratio is expected to be lower. In-situ time-resolved measurements of the sample surface state transitioning away from a “pristine” surface during plasma exposure remains the subject of future work.

3.3 Chapter Summary

The results in this chapter demonstrate that nitrogen doped diamond, in combination with the application of pulsed negative voltage biasing, can enhance negative ion yield for both high-energy and low-energy ion bombardment of the surface. The results also demonstrate that the use of pulsed biasing reduces the negative ion yield from diamond compared to a continuous bias, which was unexpected, and highlights the significance of surface defect formation for the surface production of negative ions. An identified drawback to the practical utilisation of a pulsed bias for negative ion production is that the overall number of negative ions is dependent on the duty cycle of the pulse. However, the benefit of using a pulsed bias as a means to preserve the surface state of samples and remove temperature thresholds from insulating materials makes it attractive for investigating materials that may enhance the surface production of negative ions.

Chapter 4

A plasma chemistry set for the simulation of negative ion production: spatial gradients, vibrational kinetics and gas heating

In chapters 2 and 3, the production of negative ions through the use of surface interaction processes has been studied. To develop a more complete understanding of negative ion production it is also useful to consider processes in the bulk of a plasma. In this chapter, an established reaction set, a reaction originally developed for the study of low power density CCPs in 1D is developed to enable the study of ICPs in 2D. The reaction set has been incorporated into the Hybrid Plasma Equipment Model (HPEM) with the addition of enthalpy and gas temperature dependent rates for all of the V-V and V-T reactions. This enables the simulation of gas temperature dependent negative ion production, accounting for the effects of spatial gradients and the kinetics of H_2 vibrational states.

4.1 Introduction to hybrid modelling

In this work, a hybrid model is employed to gain insight into the physics of low-temperature hydrogen plasmas. Prior to a detailed explanation of its operation, the background and motivation for its application is briefly described below.

The simulation of low temperature plasmas is challenging due to the range and disparate scales of the physical processes that must be accounted for[162–165]. A simulation must account for processes that occur at pico-second time scales up to processes that develop on the order of 10s of seconds[2,163,166]. To further complicate matters, technological plasma reactors operate in diverse configurations, power densities and gas mixtures. This means that a "general" multipurpose simulation of a low temperature plasma is challenging. Typically models are developed that are tailored to study different types of problems in specific circumstances.

Particle-In-Cell (PIC) simulations, which self consistently determine the plasma condition at steady state are considered the “gold standard” of plasma models. In a PIC model the motion of individual, or more commonly macro-particles, are considered kinetically[42,167–170]. However, the huge computational expense required to self-consistently simulate a technological plasma source, incorporating multiple dimensions, realistic charged and neutral densities, and usually complex plasma chemistry, often makes the PIC method impracticable.

There are several alternative numerical techniques to the PIC simulation described below, which can be utilised that approximate and simplify the physics of such systems, whilst still producing meaningful physical results.

4.1.1 Global modelling

Global models use particle and energy balance equations to calculate the evolution of a plasma, which is treated as being spatially uniform.[1,171–175]. Setting the initial conditions of the system and allowing it to develop in time allows global models to simulate temporal behaviour. In some cases, the use of a global model can be used to interpret spatial properties in a flowing plasma through choice of a series of gas flow rates corresponding to a series of spatial locations[176].

Of relevance to this work is that global models models enable the use of extensive reaction sets. These extensive reaction sets can be used to determine the relative importance of different reaction pathways[177]. The identification of reactions that are not important under certain conditions can then be used to benefit more spatially resolved models by reducing the number of reactions.

4.1.2 Fluid modelling

Fluid models are distinct from global models due to the ability to investigate spatial properties of a plasma. These models treat the plasma in a macroscopic manner, by taking moments of the Boltzmann equation[178–181]. This method allows the species densities, temperatures and fluxes to be calculated via conservation equations for mass, momentum and energy. In many of these models the electron energy distribution functions are determined either prior to their use within the Boltzmann equations or during the simulation in an iterative manner[163,182]. The given or calculated distributions are then used to derive the electron reaction rates and transport coefficients.

The use of a multi-dimensional fluid model is attractive due to a reduction in the computational resources compared to a fully kinetic model. However, the use of a fluid model means that kinetic effects are not included. The distribution of energy for species in fluid models is approximated as being Maxwellian, which implies that the system is collisional. For decreasing pressure and reductions in electron-neutral and ion-neutral collision frequencies, e.g. upon rarefication of the neutral gas, this assumption decreases in validity and the simulations become unable to capture collisionless effects, which include non-Maxwellian electron energy distributions[181]. Fluid models should therefore only be applied with consideration of the system collisionality.

4.1.3 Hybrid modelling

Hybrid models try to balance the disadvantages of fluid models and kinetic models against their advantages in order to achieve a compromise between computational resource and accuracy[163,169,183]. The overarching principle of hybrid modelling is to separate processes that are active and treat these processes using a distinct physical model. A method that is commonly implemented in hybrid models is to separate species within a plasma into two, where one set of species is assumed to be behaving in a collisional manner, whilst the other set has collisionless behaviour. An example of this method in action would be to model the production of secondary electrons from surfaces exposed to a plasma kinetically, as the electrons produced in this manner typically have non-thermal beam-like energies, and the rest of the plasma species using a fluid model[184]. Care must be taken when using this type of model to determine which type of numerical method is to be used, but when implemented well, hybrid models can be used to capture a much wider range of physical processes than fluid models, as well as reduce computational expense relative to the PIC approach.

4.2 The Hybrid Plasma Equipment Model

The Hybrid Plasma Equipment Model (HPEM) is a modular 2D fluid/Monte-Carlo simulation code that has been developed by Prof. Mark Kushner as part of the Computational Plasma Science and Engineering Group at the University of Michigan. This model employs a 2D geometry with both fluid and Monte-Carlo solvers. It has a modular design that expands the range of physics that can be modelled within its framework to include processes such as etching and photon emission. A comprehensive description of HPEM is given in Ref 163. The simulation has been employed as compiled directly from the source.

A simplified diagram of the hybrid plasma equipment model is shown in figure 4.1.

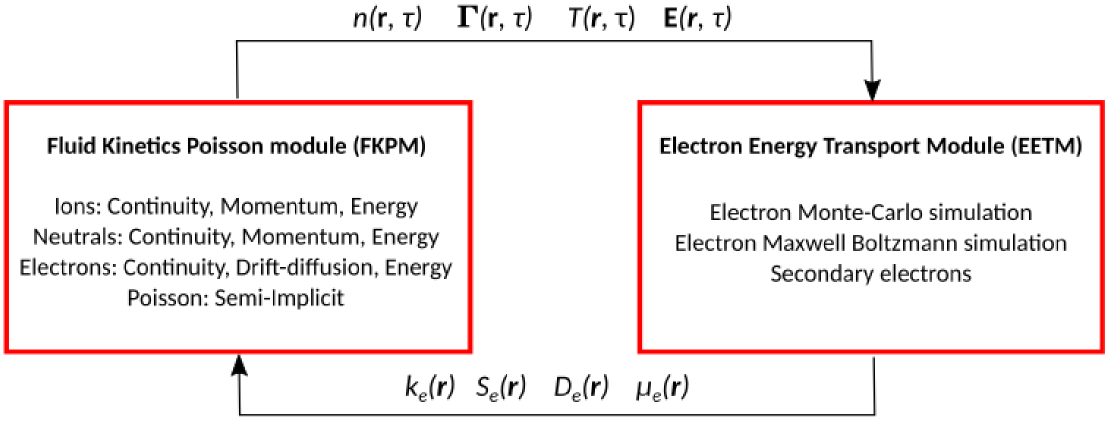

Figure 4.1: Overview of the interaction of two main solving routines, the Fluid Kinetic Particle Module (FKPM) and the Electron Energy Transport Module (EETM) within the HPEM and the exchange of information between them. The variables that are passed from the FKPM to the EETM are the spatial and temporally resolved species distributions $n(\mathbf{r},\tau)$, species fluxes $\mathbf{\Gamma}(\mathbf{r},\tau)$, temperatures $T(\mathbf{r},\tau)$, electrostatic potentials $\phi_{\mathrm{rf}}(\mathbf{r},\tau)$ and electric field strengths $\mathbf{E}(\mathbf{r},\tau)$. The variables passed from the EETM to the FKPM are the time averaged electron mobility $\mu_{\mathrm{e}}(\mathbf{r})$, diffusion coefficient $D_{\mathrm{e}}(\mathbf{r})$, electron reaction rates $k_{\mathrm{e}}(\mathbf{r})$ and source functions $S_{\mathrm{e}}(\mathbf{r})$

In this work the, modules use a rectilinear simulation mesh within which the equations used to calculate the distribution of species densities, flux and fields are solved. The mesh is constructed such that the electrostatic potentials and magnetic field strengths are resolved at the vertices of the cells, whilst the particle fluxes and electric fields are solved at the midpoints between the vertices.

The Fluid Kinetic Poisson Module (FKPM) encapsulates the fluid components of the simulation. It uses moments of the Boltzmann equation to determine the charged and neutral continuity equations as well as the electron drift diffusion equation. The electric field as a result of the distribution of the species is calculated semi-implicitly by Poisson's equation where the potential of a given cell in the simulation is using the potential in the cell at the moment the calculation is carried out, plus an incremental prediction.

The prediction uses implicit electrons and predictor-corrector ions to account for changes in these densities over the jump between iterations, where the divergence of the charged particle flux is solved using the principle of charge continuity. The spatially and temporally resolved species distributions $n(\mathbf{r},\tau)$, fluxes $\mathbf{\Gamma}(\mathbf{r},\tau)$, temperature $T(\mathbf{r},\tau)$, electrostatic potentials $\phi_{\mathrm{rf}}(\mathbf{r},\tau)$ and electric field strength $\mathbf{E}(\mathbf{r},\tau)$ are then passed to the EETM.

The EETM in this work utilises a Monte-Carlo algorithm to resolve the spatial distribution of the time averaged electron mobility $\mu_{\mathrm{e}}(\mathbf{r})$, diffusion coefficient $D_{\mathrm{e}}(\mathbf{r})$, electron reaction rates $k_{\mathrm{e}}(\mathbf{r})$ and source functions $S_{\mathrm{e}}(\mathbf{r})$.

The collisions for the electrons within the Monte-Carlo algorithm are treated stochastically, with the collision rates of the electrons interpolated from the energy and cross sections defined in the plasma chemistry set. The time between collisions is determined using a collision-frequency model based upon the calculated collision rate with the stochastic component. The electron collisions can either occur (a real collision) or not occur (a null collision) based upon a random “dice roll” for each of the simulated collisions determined by the collision-frequency calculation. If a real collision occurs, the type of collision is determined by another random number and normalised form of the collision cross-sections[163]. The process is repeated for a number of cycles within the code (typically 5 RF cycles) and angularly resolved electron energy distribution functions (EEDFs) are determined. The resulting electron mobility, transport and reaction rates are computed from the mean temperature of the EEDFs which are passed back to the FKPM. The simulation then proceeds by looping through these modules until the change in the distributions between two iterations is considered to be effectively zero, after which point the simulation has converged.

4.2.1 HPEM governing equations

The method of calculation employed by the HPEM for solving particle distributions requires the understanding of how particle mobility and diffusion coefficients are calculated. Equations for the electron diffusion and mobility are given respectively by equations 4.1 and 4.2:

$$D_e = \frac{k_b \hat{T}_e \mu_e}{e} \tag{4.1}$$

with

$$\mu_e = \frac{\upsilon_{ed}}{eE} \tag{4.2}$$

where $\hat{T}_e$ is the mean electron temperature, υ_{ed} and E are the scalar values of the electron drift velocity and electric field, respectively. The ion mobility and diffusion coefficients are calculated in a similar manner, with mean ion temperature and ion specific charge $Z_i e$.

The flux and temperature of species within the model are calculated using three moments of the Boltzmann equation as shown in equation 4.3.

$$\frac{\delta f(\epsilon)}{\delta t} + \mathbf{v} \cdot \nabla f(\epsilon) - \frac{Z_s e}{m_s}[\mathbf{E} + \mathbf{v} \times \mathbf{B}] \cdot \nabla_{\mathbf{v}} f(\epsilon) = |\frac{\delta f(\epsilon)}{\delta t}|_{coll} \tag{4.3}$$

where $\mathbf{v} = (\upsilon_{\mathrm{x}}, \upsilon_{\mathrm{y}}, \upsilon_{\mathrm{z}})$ is the 3D velocity vector, $\mathbf{E}$ and $\mathbf{B}$ are the electric and magnetic field vectors in real space (x, y, z) respectively. Z_{s} and m_{s} represent the specific charge and atomic mass of the species s, respectively.

In this form the Boltzmann equation is used to determine the evolution of the particle energy distribution function in a seven dimensional geometry with three spatial vectors, three velocity vectors and with respect to time. The exact treatment of the continuity of each species in the simulation is dependent on the type of species being considered. In the case of the conservation of mass, the treatment is similar for all species and is given by equation 4.4:

$$\frac{\delta n_s}{\delta t} = -\nabla \cdot \Gamma_s + S_s \tag{4.4}$$

where the flux of a particular species is Γ_s and S_s is the particle source function. The electron flux Γ_e and collisional energy transfer come from the second and third terms of the Boltzmann equation. This gives the momentum conservation of electrons via drift diffusion as:

$$\mathbf{\Gamma}_e = -n_e \mu_e \mathbf{E} - D_e \nabla_e \tag{4.5}$$

with D_e and μ_e defined previously.

The ion and neutral momentum equation is given as:

$$\frac{\delta \Gamma_i}{\delta t} = -\frac{1}{m_i}\nabla(n_i k_b T_i) - \nabla \cdot (n_i v_i^2) + \frac{q_i n_i}{m_i}\mathbf{E} - \nabla \cdot \bar{\bar{v}}_i - \sum_j \frac{m_j}{m_i + m_j} n_i n_j (v_i - v_j) \upsilon_{ij} \tag{4.6}$$

where n_i, T_i, m_i and v_i are species density, mean temperature, mass and velocity for the ith (or jth) species respectively. $\bar{\bar{v}}_\mathrm{i}$ is the viscosity tensor for species i, υ_ij is the collision frequency between species i and j, $\mathbf{E}$ is the electric field strength and k_b is the Boltzmann constant.

The energy continuity equation is given as:

$$\begin{aligned}\frac{\delta n_i c_i T_i}{\delta t} &= \nabla \cdot \kappa_i \nabla T_i - P_i \nabla \cdot v_i - \nabla \cdot (n_i \bar{v}_i \epsilon_i) \\ &\quad + \frac{n_i q_i^2}{m_i \upsilon_i} E_s^2 + \frac{n_i q_i^2 \upsilon_i}{m_i(\upsilon_i^2 + \omega^2)} E_\Theta^2 \\ &\quad + \sum_j 3 \frac{m_j}{m_i + m_j} n_i n_j \upsilon_{ij} k_b (T_j - T_i) \\ &\quad \pm \sum_j n_i n_j k_{\Delta H_{ij}} \Delta H \pm \sum_j 3 n_i n_j k_{ij} k_b T_j\end{aligned} \tag{4.7}$$

where c_i is the specific heat capacity, κ_i is the species conductivity, P_i is the partial pressure and $\epsilon = c_\mathrm{i} T_\mathrm{i}$ is the specific energy of species i. The change in the enthalpy for an exothermic or endothermic reaction ΔH and the rate coefficient for a change in enthalpy is given as $k_{\Delta H_{ij}}$. For neutral species the electric field term is neglected, whilst for ions the viscosity is neglected due to the comparatively lower densities relative to the neutral particles. This equation is necessary for enabling a self-consistent calculation of the temperature of the heavy particle species within the simulation domain.

The simulation of ions impacting surfaces assumes that they lose their kinetic and any remaining potential energy to the material surfaces after Auger neutralisation[185]. The exchange of thermal energy of species with surface is carried out using a temperature "jump" approach, across the computational cell next to the surface. This approach is outlined in Ref. 163. The gradient of the temperature jump is proportional to the gradient of the temperature between the surface and the plasma species, multiplied by the thermal accommodation coefficient. Thus, if the thermal accommodation coefficient is small, the temperature exchange is small, and if it is large, the exchange is much higher. This has implications for accurately modelling gas temperature dependent plasma processes[186]. The thermal accommodation coefficient varies depending on the surface condition, the type of gas species used, and the flow of the gas across its surface. A value of 0.4 is used in the simulation domain for all surfaces to minimise the influence of surfaces on the plasma.

The equations defined above are close through the use of the semi-implicit Poisson equation, which updates the electric potential of the system[163]:

$$\nabla\phi = -\frac{1}{\epsilon_0}\sum_{s}^{n_s}(eZ_s n_s - \nabla\cdot\Gamma_s) + (en_e - \nabla\cdot\Gamma_e) \tag{4.8}$$

where the charged species are as defined previously.

4.3 Development of the plasma chemistry reaction set

A reaction chemistry set, based upon that previously established in Ref. 187 for the study of a 1D CCP is developed for use in the HPEM for the study of higher power density ICPs. The reaction set includes 16 neutral species (H_2, H_2(vib = 1-14), and H), 4 types of ions (H^+ H_2^+ H_3^+ and H^-) as well as the electrons.

The reaction set presented in this work has been developed further from what is already established in the literature in the context of 1D kinetic simulations of hydrogen plasmas at low pressures[135]. The development includes a conversion of energy dependent ion-neutral collision cross sections into Arrhenius forms suitable for the HPEM code, the calculation of gas temperature dependent reaction rates for V-V, V-T and V-T atomic reactions followed by their conversion into the Arrhenius form required for HPEM, the inputting of all electron impact reaction rates into the supporting files for HPEM, the inclusion of enthalpy changes for each reaction in the reaction set, and an update to all of the references for each reaction given in previously published work which has fixed some broken links.

4.3.1 Heavy particle reactions

Twelve heavy particle ion-neutral reactions are incorporated into HPEM from the cross section data of Ref. 187, with updates made to include gas temperature dependent reaction rates to two of the reactions. A requirement for the incorporation of these types of reactions into HPEM is the use of a form of the Arrhenius equation:

$$K(T) \;=\; A\,\left(\frac{T}{298}\right)^{n}\,\exp\left(\frac{-E_{\mathrm{act.}}}{T}\right) \tag{4.9}$$

where A is the Arrhenius parameter in units of cm^3 s^{-1}, n is a dimensionless scaling parameter and $E_{\mathrm{act.}}$ is the activation energy of the reaction in units of Kelvin.

In order to determine the reaction rates, such that a Arrhenius equation can be fit to the data, a process of detailed balance is carried out. The range of pressures of interest are from 2.6 Pa to 26.6 Pa (15 mTorr to 200 mTorr). The Knudsen number, as determined from equation[188,189]:

$$K_n = \frac{\lambda_{mfp}}{L} = \frac{1}{n_{H_2}\sigma(\epsilon)_{H_2}L} \tag{4.10}$$

where λ_{mfp} is the mean free path of the neutral species, L is the smallest length within the plasma volume, n_{H_2} is the density of the hydrogen, and $\sigma(\epsilon)_{H_2}$ is the kinetic diameter of the hydrogen molecule, taken to be 2.75Å[190]. The Knudsen number is estimated to be between 0.5 and 0.01 for the pressure range of interest. A value above 1 for the Knudsen number would suggest that the gas is substantially rarefied. As $\mathrm{K_n} < 1$, it is therefore reasonable to consider the energy distribution of each heavy particle reactant to be reasonably described by a Maxwellian distribution:

$$f_{\mathrm{m}} \;=\; \left(\frac{m_{\mathrm{R}}}{2\pi kT}\right)^{\frac{3}{2}}\exp\left(-\frac{m_{\mathrm{R}}\upsilon_{\mathrm{R}}^2}{2kT}\right) \tag{4.11}$$

which is then used to calculate the gas temperature dependent reaction rate using equation:

$$K_{\mathrm{AB}}(T) \;=\; \langle\sigma_{\mathrm{AB}}\;\upsilon_{\mathrm{R}}\rangle \;=\; \int_0^{\infty}\; f_{\mathrm{m}}\upsilon_{\mathrm{R}}\sigma_{\mathrm{AB}}(\upsilon_{\mathrm{R}})4\pi\upsilon_{\mathrm{R}}^2\mathrm{d}\upsilon_{\mathrm{R}} \tag{4.12}$$

where K_{AB} is the reaction rate between particles A and B, υ_R is the particle velocity, $\sigma_{AB}(\upsilon_R)$ is the cross section in terms of particle velocity, m_{R} is the reduced collisional mass, and T is the gas temperature[2].

The Arrhenius equation is fit using an unweighted least squares fitting routine. Each reaction and the parameters within the Arrhenius equation are shown in table 4.1.

Table 4.1: Heavy particle reactions with associated values parameters for the Arrhenius equation applied within HPEM. Reaction rate coefficient is cm^3s^{-1} for 2-body reactions.

No.	Reaction	Reaction process	A (cm^3s^{-1})	n	$E_{act.}$ (K)	ΔH_f (eV)	Ref.
1	$H_3^+ + H_2 \rightarrow H_2 + H_3^+$	H_3^+/H_2 Elastic scattering	2.07×10^{-9}	-0.01	0	0	191
2	$H_3^+ + H_2 \rightarrow H^+ + H_2 + H_2$	H_3^+ ionic conversion	6.14×10^{-13}	0.65	39257	-4.43	140
3	$H_3^+ + H_2 \rightarrow H_2^+ + H + H + H$	H_3^+ ionic conversion	6.66×10^{-12}	0.33	72782	-10.8	140
4	$H_2 + H^+ \rightarrow H^+ + H_2$	H_2/H^+ Momentum transfer	3.61×10^{-9}	0.04	0	0	140
5	$H^+ + H \rightarrow H^+ + H$	H/H^+ charge exchange collision	2.44×10^{-9}	0.39	0	0	126,192
6	$H_2^+ + H_2 \rightarrow H_3^+ + H(fast)$	H_3^+ production from H_2	2.33×10^{-9}	0	0	1.76	140
7	$H_2^+ + H_2 \rightarrow H_2^+ + H_2$	H_2^+ charge exchange from slow H_2^+	5.26×10^{-12}	1.39	0	0	140
8	$H^- + H_2 \rightarrow H^- + H_2$	Momentum transfer of H^- with H_2	1.15×10^{-9}	0.09	0	0	140
9	$H^- + H_2 \rightarrow H_2 + H + e$	Detachment of H^- with H_2	7.27×10^{-12}	1.27	15638	0	140
10	$H^- + H \rightarrow H^- + H$	Charge exchange of H^- with H	1.53×10^{-8}	0.33	0	0	126,192
11	$H^- + H \rightarrow H_2 + e$	Detachment of H^- with H	1.746×10^{-9}	-0.022	403	0	51
12	$H^- + H_3^+ \rightarrow H_2 + H_2$	Neutralisation of H^- with H_2^+	2.0×10^{-7}	-0.5	0	12.9	52,193

The fit to the Arrhenius equation for each calculated reaction rate is performed between gas temperatures of 200 K and 3000 K, except for reaction number 2 and 3 in table 4.1. These were fit between 250 K and 9000 K on account of a higher threshold temperature. The coefficients in the Arrhenius equation are then used in the FKPM to determine the rates for the produced species.

No cross section data was available for reaction number 12, so the Arrehenius reaction rate fit was calculated using a suggested rate equation from Ref. 52.

4.3.2 Heavy particle vibrational reactions

This work considers mono-quantum exchange of vibrational energy between hydrogen molecules via Vibrational-Vibrational (V-V) and Vibrational-Translational (V-T) interactions as well as multi-quantum exchange of energy via reactive and non-reactive atomic V-T processes. The reaction set accounts for the neutral-gas temperature when calculating the reaction rates, which builds upon the work of Ref. 187 where the background gas temperature is isothermal and the V-V and V-T reaction had a fixed reaction rate.

The V-V reaction is defined as:

$$\mathrm{H}_2(\upsilon) \ + \ \mathrm{H}_2(\omega \ + \ 1) \rightarrow \mathrm{H}_2(\upsilon \ + \ 1) \ + \ \mathrm{H}_2(\omega) \tag{4.13}$$

where υ and ω are the vibrational states of the interacting hydrogen molecules.

The reaction rates for the V-V reactions have been calculated using equation[52]:

$$\begin{aligned} K^{\upsilon,\upsilon+1}_{\omega+1,\omega} \ = \ k^{0,1}_{1,0} \ \cdot \ (\upsilon+1) \ \cdot \ (\omega+1) \ \cdot \ \left[\frac{3}{2} \ - \ \frac{1}{2}\exp(-\delta_{\mathrm{VV}}(\upsilon-\omega)\right] \\ \times \ \exp(-\Delta_1(\upsilon-\omega) \ - \ \Delta_2(\upsilon-\omega)^2), \ (\upsilon \ > \ \omega) \end{aligned} \tag{4.14}$$

where

$$\begin{aligned} K^{0,1}_{1,0} \ &= \ 4.23 \ \times \ 10^{-15}\left(\frac{300}{T}\right)^{\frac{1}{3}} \ \mathrm{cm}^{-3}\mathrm{s}^{-1} \\ \delta \ &= \ 0.21\left(\frac{T}{300}\right)^{\frac{1}{2}} \\ \Delta_1 \ &= \ 0.236\left(\frac{T}{300}\right)^{\frac{1}{4}} \\ \Delta_2 \ &= \ 0.0572\left(\frac{300}{T}\right)^{\frac{1}{3}} \end{aligned} \tag{4.15}$$

As these reactions are directional for the case where $\upsilon \ > \ \omega$, the principle of detailed balance is carried out using equation:

$$K^{\upsilon,\upsilon+1}_{\omega+1,\omega} \;=\; k^{\upsilon+1,\upsilon}_{\omega,\omega+1}\; exp\left(\frac{2E_I}{kT_g}\;(\omega-\upsilon)\right) \tag{4.16}$$

where $K^{\upsilon,\upsilon+1}_{\omega+1,\omega}$ is the reaction rate and T is the gas temperature. In a similar manner to the heavy particle reactions described in section 4.3.1, the calculated reaction rates for these reactions have then been fit using an unweighted least squared fitting routine to equation 4.9 between gas temperatures of 300 K and 1200 K.

The V-T reactions are defined as:

$$\mathrm{H_2}(\upsilon) \;+\; \mathrm{H_2} \rightarrow \mathrm{H_2}(\upsilon \;-\; 1) \;+\; \mathrm{H_2} \tag{4.17}$$

for the forward reaction and

$$\mathrm{H_2}(\upsilon) \;+\; \mathrm{H_2} \rightarrow \mathrm{H_2}(\upsilon \;+\; 1) \;+\; \mathrm{H_2} \tag{4.18}$$

for the reverse reaction.

The reaction rates for the V-T reactions are similarly calculated using equations from 52:

$$\begin{aligned} K^{\mathrm{H_2}(\omega)}_{\upsilon,\upsilon-1} &= 7.47 \;\times\; 10^{-12}\,\sqrt{T}\,\exp\left(-93.87\;T^{-\frac{1}{3}}\right)\upsilon \\ &\times\, \exp\left[\delta_{\mathrm{VT}}(\upsilon \;-\; 1) \;+\; \delta'_{\mathrm{VT}}\upsilon\right]\;\; \mathrm{cm^{-3}s^{-1}} \end{aligned} \tag{4.19}$$

where

$$\delta_{VT} \;=\; 0.97\,\left(\frac{300}{T}\right)^{-\frac{1}{3}}, \qquad \delta'_{VT} \;=\; 0.287\left(\frac{300}{T}\right)^{-\frac{1}{2}} \tag{4.20}$$

The equation is similarly directional, such that the vibrational state of the products is lower than the reactants, meaning that the principle of detailed balance is again applied in order to calculate the reverse reaction rate as given by equation:

$$K_{\text{v-1, v}} \;=\; k_{\text{v, v-1}}\; exp\left(-\frac{E_I}{kT_g}\;(1 \;-\; 2\chi_e\upsilon)\right) \tag{4.21}$$

where χ_e is the first anharmonic constant, equal to 0.027568[54,194]. The exchange of energy between vibrational states can also occur through collisions with neutral atomic hydrogen.

$$\mathrm{H_2}(\upsilon) \;+\; \mathrm{H} \rightarrow \mathrm{H_2}(\upsilon \;+\; 1) \;+\; \mathrm{H} \tag{4.22}$$

This reaction can occur through two reaction pathways, defined as reactive or non-reactive, both have been added to the reaction set. Multi-quantum exchanges are also accounted for. Cross sectional data for these reactions is taken from Ref. 53 and unweighted least square fits of the reaction rates to the Arrhenius equation 4.9 is carried out.

The V-V, V-T and V-T atomic reactions are listed in an abbreviated form in table 4.2.

Table 4.2: Heavy particle vibrational reactions (V-V), (V-T) and (atomic V-T). Reaction rates are calculated for each case using listed equations.

No.	Reaction	Reaction process	Equation	Ref.
13 - 26	$H_2(\upsilon) + H_2 \rightarrow H_2(\upsilon - 1) + H_2$	Mono-quantum $H_2(\upsilon)/H_2$ V-T exchange	4.19	54
27 - 40	$H_2(\upsilon - 1) + H_2 \rightarrow H_2(\upsilon) + H_2$	Mono-quantum $H_2(\upsilon)/H_2$ V-T exchange	4.19 and 4.21	54
41 - 236	$H_2(\upsilon) + H_2(\omega + 1) \rightarrow H_2(\upsilon + 1) + H_2(\omega)$	Mono-quantum $H_2(\upsilon)/H_2$ V-V exchange	eqn. 4.14 ($\omega > \upsilon$) 4.14 and 4.16 ($\omega \leq \upsilon$)	54
237 - 295	$H_2(\upsilon) + H \rightarrow H_2(\omega) + H$	Multi-quantum $H_2(\upsilon)/H$ V-T exchange non-reactive	-	53
296 - 354	$H_2(\upsilon) + H \rightarrow H_2(\omega) + H$	Multi-quantum $H_2(\upsilon)/H$ V-T exchange reactive	-	53

4.3.3 Electron impact reactions

This work includes: elastic scattering, inelastic scattering, superelastic scattering, electron impact dissociation, electron impact dissociation with ionisation, dissociative attachment and direct ionisation. These processes are shown in tables 4.3, 4.4, 4.5, and 4.6.

Table 4.3: Non-vibrational electron impact reactions.
Reaction rates calculated in the FKPM module within HPEM from cross sections in associated references.

No.	Reaction	Reaction process	Δ H (eV)	Ref.
355	$e + H_2 \rightarrow H_2 + e$	Elastic scattering (energy dependent anisotropic scattering)	0.0	[195,196]
356	$e + H_2(\upsilon) \rightarrow H_2(\upsilon) + e$	Elastic scattering (energy dependent anisotropic scattering)	0.0	[195,196]
357	$e + H \rightarrow H + e$	Elastic scattering from atomic hydrogen	0.0	[197,198]
358	$e + H_2 \rightarrow H^+ + H + 2e$	Ionisation through dissociation	0.0	[51]
359	$e + H \rightarrow H^+ + 2e$	Atomic ionisation	0.0	[199]
360	$e + H_2 \rightarrow H_2^+ + 2e$	Direct impact ionisation	0.0	[200]
361	$e + H_2 \rightarrow H + H(n = 2) + e$	Dissociation to excited atoms via Lyman [1]	0.0	[201]
362	$e + H_2 \rightarrow H + H(n = 3) + e$	Dissociation to excited atoms via Balmer [2]	0.0	[201]
363	$e + H_2 \rightarrow H + H + e$ (via $b^3\Sigma_u^+$)	H_2X dissociation through triplet states	4.38	[201]
364	$e + H_2 \rightarrow H + H + e$ (via $c^3\Pi_u$)	H_2X dissociation through triplet states	0.0	[201]
365	$e + H_2 \rightarrow H + H + e$ (via $a^3\Sigma_g^+$)	H_2X dissociation through triplet states	0.0	[201]
366	$e + H_2 \rightarrow H + H + e$ (via $d^3\Pi_u$)	H_2X dissociation through triplet states	0.0	[201]

---

[1] H(n = 2-3) density not resolved
[2] H(n = 2-3) density not resolved

Table 4.4: eV reactions υ to ω. Inelasitc and superelastic electron collisions for excitation of hydrogen moelcules to vibrational states $\upsilon \leq 5$.

No.	Reaction	Reaction process	Δ H (eV)	Ref.
367	$e + H_2(\upsilon = 0) \rightarrow H_2(\omega = 1) + e$	eV Process (excitation)	0.0	200
368	$e + H_2(\upsilon = 0) \rightarrow H_2(\omega = 2) + e$	eV Process (excitation)	0.0	200
369	$e + H_2(\upsilon = 0) \rightarrow H_2(\omega = 3) + e$	eV Process (excitation)	0.0	200
340	$e + H_2(\upsilon = 0) \rightarrow H_2(\omega = 4) + e$	eV Process (excitation)	0.0	202
341	$e + H_2(\upsilon = 0) \rightarrow H_2(\omega = 5) + e$	eV Process (excitation)	0.0	202
342	$e + H_2(\upsilon = 1) \rightarrow H_2(\omega = 0) + e$	eV Process (de-excitation)	0.0	200
343	$e + H_2(\upsilon = 2) \rightarrow H_2(\omega = 0) + e$	eV Process (de-excitation)	0.0	200
344	$e + H_2(\upsilon = 3) \rightarrow H_2(\omega = 0) + e$	eV Process (de-excitation)	0.0	200
345	$e + H_2(\upsilon = 4) \rightarrow H_2(\omega = 0) + e$	eV Process (de-excitation)	0.0	202
346	$e + H_2(\upsilon = 5) \rightarrow H_2(\omega = 0) + e$	eV Process (de-excitation)	0.0	202

Table 4.5: EV reactions $\upsilon = 0,1,2$ to ω. Resonant excitation of hydrogen molecules through electron collisions.

No.	Reaction	Reaction process	Δ H (eV)	Ref.
347-349	$e + H_2(\upsilon = 0,1,2) \rightarrow H_2(\omega = 0) + e$ (via $B^1\Sigma_u^+$, $C^1\Pi_u$)	EV processes	0.0	203
350-352	$e + H_2(\upsilon = 0,1,2) \rightarrow H_2(\omega = 1) + e$ (via $B^1\Sigma_u^+$, $C^1\Pi_u$)	EV processes	0.0	203
353-355	$e + H_2(\upsilon = 0,1,2) \rightarrow H_2(\omega = 2) + e$ (via $B^1\Sigma_u^+$, $C^1\Pi_u$)	EV processes	0.0	203
356-358	$e + H_2(\upsilon = 0,1,2) \rightarrow H_2(\omega = 3) + e$ (via $B^1\Sigma_u^+$, $C^1\Pi_u$)	EV processes	0.0	203
359-361	$e + H_2(\upsilon = 0,1,2) \rightarrow H_2(\omega = 4) + e$ (via $B^1\Sigma_u^+$, $C^1\Pi_u$)	EV processes	0.0	203
362-364	$e + H_2(\upsilon = 0,1,2) \rightarrow H_2(\omega = 5) + e$ (via $B^1\Sigma_u^+$, $C^1\Pi_u$)	EV processes	0.0	203
365-367	$e + H_2(\upsilon = 0,1,2) \rightarrow H_2(\omega = 6) + e$ (via $B^1\Sigma_u^+$, $C^1\Pi_u$)	EV processes	0.0	203
368-370	$e + H_2(\upsilon = 0,1,2) \rightarrow H_2(\omega = 7) + e$ (via $B^1\Sigma_u^+$, $C^1\Pi_u$)	EV processes	0.0	203
371-373	$e + H_2(\upsilon = 0,1,2) \rightarrow H_2(\omega = 8) + e$ (via $B^1\Sigma_u^+$, $C^1\Pi_u$)	EV processes	0.0	203
374-376	$e + H_2(\upsilon = 0,1,2) \rightarrow H_2(\omega = 9) + e$ (via $B^1\Sigma_u^+$, $C^1\Pi_u$)	EV processes	0.0	203
377-379	$e + H_2(\upsilon = 0,1,2) \rightarrow H_2(\omega = 10) + e$ (via $B^1\Sigma_u^+$, $C^1\Pi_u$)	EV processes	0.0	203
380-382	$e + H_2(\upsilon = 0,1,2) \rightarrow H_2(\omega = 11) + e$ (via $B^1\Sigma_u^+$, $C^1\Pi_u$)	EV processes	0.0	203
383-385	$e + H_2(\upsilon = 0,1,2) \rightarrow H_2(\omega = 12) + e$ (via $B^1\Sigma_u^+$, $C^1\Pi_u$)	EV processes	0.0	203
386-388	$e + H_2(\upsilon = 0,1,2) \rightarrow H_2(\omega = 13) + e$ (via $B^1\Sigma_u^+$, $C^1\Pi_u$)	EV processes	0.0	203
389-391	$e + H_2(\upsilon = 0,1,2) \rightarrow H_2(\omega = 14) + e$ (via $B^1\Sigma_u^+$, $C^1\Pi_u$)	EV processes	0.0	203

Table 4.6: Production of negative ions through dissociative attachment from hydrogen $e + H_2(\upsilon) \rightarrow H + H^-$.

No.	Reaction	Reaction process	Δ H (eV)	Ref.
392	$e + H_2(\upsilon = 0) \rightarrow H + H^-$	Dissociative attachment	0.04	204
393	$e + H_2(\upsilon = 1) \rightarrow H + H^-$	Dissociative attachment	0.03	204
394	$e + H_2(\upsilon = 2) \rightarrow H + H^-$	Dissociative attachment	0.04	204
395	$e + H_2(\upsilon = 3) \rightarrow H + H^-$	Dissociative attachment	0.04	204
396	$e + H_2(\upsilon = 4) \rightarrow H + H^-$	Dissociative attachment	0.03	204
397	$e + H_2(\upsilon = 5) \rightarrow H + H^-$	Dissociative attachment	0.03	204
398	$e + H_2(\upsilon = 6) \rightarrow H + H^-$	Dissociative attachment	0.03	204
399	$e + H_2(\upsilon = 7) \rightarrow H + H^-$	Dissociative attachment	0.03	204
400	$e + H_2(\upsilon = 8) \rightarrow H + H^-$	Dissociative attachment	0.02	204
401	$e + H_2(\upsilon = 9) \rightarrow H + H^-$	Dissociative attachment	0.03	204
402	$e + H_2(\upsilon = 10) \rightarrow H + H^-$	Dissociative attachment	0.28	204
403	$e + H_2(\upsilon = 11) \rightarrow H + H^-$	Dissociative attachment	0.39	204
404	$e + H_2(\upsilon = 12) \rightarrow H + H^-$	Dissociative attachment	0.56	204
405	$e + H_2(\upsilon = 13) \rightarrow H + H^-$	Dissociative attachment	0.69	204
406	$e + H_2(\upsilon = 14) \rightarrow H + H^-$	Dissociative attachment	0.76	204

4.3.3.1 Elastic scattering reactions

In low temperature plasmas, electrons have a higher translational temperature than the neutral heavy particles, however the small mass of electrons compared to the heavy particles means the momentum of the heavy neutral species will be virtually unaffected by collisions with electrons. The cross section for elastic scattering from hydrogen molecules supplied to the HPEM is isotropic, however an energy dependent scattering parameter is added to the cross section that accounts for anisotropic scattering as the electron energy increases. This cross section and adjustment is assumed to be the same for all neutral hydrogen molecules, $H_2(\upsilon = 0 \text{ - } 14)$[196].

4.3.3.2 Inelastic and superelastic scattering

The inelastic scattering via eV processes has a threshold of between 0.516 eV and 2.26 eV and a relatively large cross section. These reactions are reversible and detailed balance has been carried out to calculate the equivalent superelastic collision using equation:

$$\sigma(\epsilon \ - \ \Delta\epsilon) = \sigma_0(\epsilon)\frac{\epsilon}{\epsilon \ - \ \Delta\epsilon}\frac{g*}{g} \tag{4.23}$$

where $g = g* = 1$, ϵ is the electron energy, and $\Delta\epsilon$ is the threshold energy for the inelastic process. The cross sections for cases where $\upsilon > 5$ have not been considered due to lack of data[51,200,202].

4.3.3.3 EV processes

As described in section 1.3, the EV process is a two step process where a electron collision excites the hydrogen molecule into an excited state, which then spontaneously decays into a excited vibrational level by the emission of a photon. This two step process means that detailed balance for the reverse process is not required[51].

4.3.3.4 Dissociative attachment process

The creation of negative ions in the bulk of a plasma is wholly due to the process of dissociative attachment. The cross section for these processes increases by 5 orders of magnitude from $\upsilon = 0$ to $\upsilon = 7$[19,205]. This means that the creation of highly vibrationally excited molecules is necessary for the creation of negative ions.

4.3.3.5 Dissociation processes

There are multiple processes that form hydrogen atoms. One important reaction is via dissociation through a triplet state excitation by electron impact:

$$e + H_2 \rightarrow e + H_2(b^3\Sigma_u^+, c^3\Pi_u, a^3\Sigma_g^+, d^3\Pi_u) \rightarrow e + H + H \tag{4.24}$$

Of these reactions, the $H_2(b^3\Sigma_u^+)$ excited state is repulsive, resulting in the creation of hydrogen atoms with kinetic energy[187].

Another process for atomic hydrogen production is through electron impact dissociation towards excited atoms. The density of these excited states is not tracked directly. The energy associated with their production and eventual decay to ground states through photon emission is assumed[51].

4.3.4 Ionisation

There are three ionisation processes, which include: dissociative ionisation, direct impact ionisation, and atomic ionisation. The molecular ionisation process is split between two processes, where H_2^+ and H^+ is produced. These processes have a branching ratio of 93% and 7% respectively, which is captured within the associated cross sections[51,140,187].

4.3.5 Plasma surface interactions

The surface interaction for plasma species with the walls of the reactor is modelled in the HPEM with three parameters. The first is the sticking probability, which determines the probability that an interaction of the species with the wall will occur. If a reaction is determined to take place, a probability for a specifc species being returned to the plasma is then calculated. This probability is defined by the return probability. The return species is returned to the plasma with a temperature given by the thermal accommodation coefficient which has been set to 0.4, as described in section 4.2. The sticking and return probabilities and are given in table 4.7.

Table 4.7: Plasma surface interactions. The sticking probability is the likelihood a species undergoes an interaction with the surface. The return probability is the probability of any interaction causing a return species to come from the surface.

Wall interaction	Sticking probability	Return probability	Ref.
$H_2 \rightarrow H_2$	0	0	[126]
$H \rightarrow H_2$	0.1	0.5	[126]
$H^+ \rightarrow H$	1.0	1.0	[126]
$H_2^+ \rightarrow H_2$	1.0	1.0	[126]
$H_3^+ \rightarrow H_2$ and H	1.0	1.0	[126]
$H^- \rightarrow H$	1.0	1.0	[126]
$H_2(\upsilon = 1 - 14) \rightarrow H_2(\upsilon = 0)$	0.02	1.0	[187]

4.3.6 Reaction exothermicity

The exothermicity of a reaction is calculated by taking the difference in the formation energy for the reactants and products. In the case of electron impact reactions, the threshold energy for the process is included to account for the activation energy of the reaction. The enthalpy change for the dissociative electron impact reactions (361 to 366) is set to zero due to the energy of formation for the atomic hydrogen being lost through photon emission of the excited hydrogen molecules, which is not followed in this reaction set. The exception to this is reaction 363 where the excitation state is $b^3\Sigma_u^+$ which is repulsive[51]. This means that the hydrogen atoms produced in this dissociation reaction are given kinetic energy equivalent to the difference in the energy of formation for the products and reactants[187]. The formation energy for each species is listed in table 4.8.

Table 4.8: Enthalpy of formation for each species in the model.

Species	Enthalpy of formation (eV)	Ref.
H_2	0	206,207
H	2.26	206,207
H^+	15.91	206,207
H_2^+	15.49	206,207
H_3^+	11.47	206,207
H^-	1.44	206,207
$H_2(\upsilon = 1)$	0.516	51
$H_2(\upsilon = 2)$	1.003	51
$H_2(\upsilon = 3)$	1.461	51
$H_2(\upsilon = 4)$	1.891	51
$H_2(\upsilon = 5)$	2.293	51
$H_2(\upsilon = 6)$	2.667	51
$H_2(\upsilon = 7)$	3.012	51
$H_2(\upsilon = 8)$	3.327	51
$H_2(\upsilon = 9)$	3.611	51
$H_2(\upsilon = 10)$	3.863	51
$H_2(\upsilon = 11)$	4.086	51
$H_2(\upsilon = 12)$	4.254	51
$H_2(\upsilon = 13)$	4.384	51
$H_2(\upsilon = 14)$	4.461	51

4.4 Comparison with experimental measurements

To build confidence in the simulations a comparison is made to previously published data from Ref. 208. The experimental reactor differs from the simulation data in the following ways. Firstly the electrode to dielectric spacing is 4 cm compared to 5 cm, the radius of the lower electrode is 5 cm compared to 8 cm and the inductive coil used to power the plasma is designed as a series of rings in the simulations but has a double spiral structure in the experiments.

Since a detailed treatment of the plasma surface interactions further to that described in section 4.3.5 is beyond the scope of this work, the comparisons are focused on the plasma measurements made within the bulk of the plasma. This is distinct from previous work with relatively high plasma surface to volume ratios[209] or where measurements are undertaken in the near-surface region[210].

4.4.1 Description of the simulation mesh

The geometry of the simulation mesh used in this study is shown in figure 4.2.

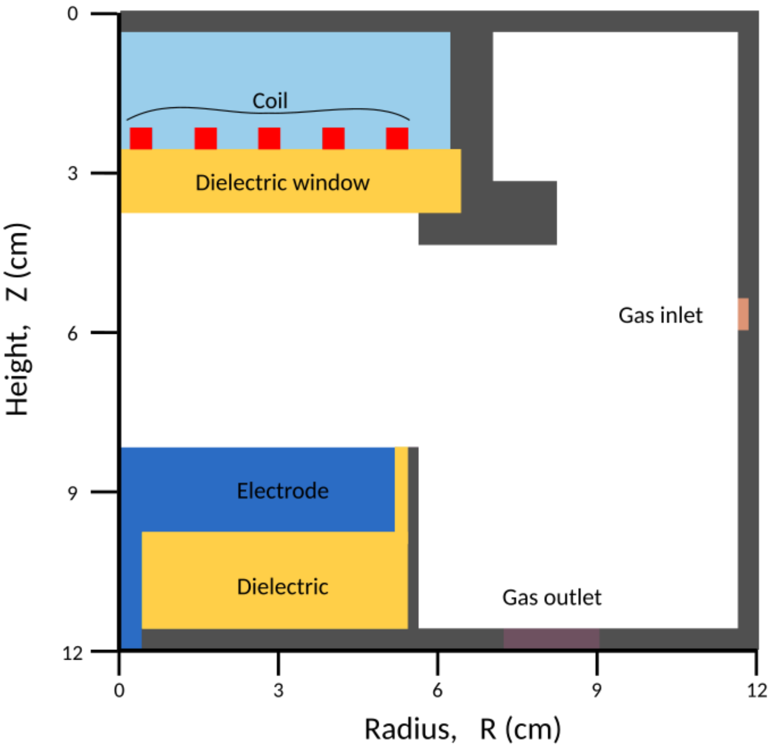

Figure 4.2: Schematic of the simulation geometry. The white space is the plasma volume. An air surrounded 5 turn coil is separated from the plasma volume by a quartz dielectric window. A grounded metal electrode is positioned below the dielectric window with a quartz dielectric spacer separating it from the rest of the grounded metal reactor walls. A gas inlet is positioned at the outer edge of the reactor and a gas outlet is positioned at the base of the reactor.

The simulation mesh represents an inductively coupled reactor similar in design to the Gaseous Electronics Conference reference cell (GEC) reactor[211]. This particular design has been chosen as a starting point for the development of these simulations due to technological relevance and previous experimental work carried out in similar reactors[208–210].

As shown in figure 4.2, the mesh represents a simulation space 12.0 cm in height and 12.0 cm in radius that is radially symmetric. A 5-turn planar coil of 10.8 cm diameter drives the plasma and is separated from the plasma region by a dielectric window with a thickness of 1.2 cm. The gap between this window and a metallic wafer holder electrode is 4.0 cm. The wafer holder is 5.0 cm across and extends over a gas outlet at the base of the reactor. A gas inlet at the side of the reactor injects ground state hydrogen into the system, whilst the gas pressure in the system is maintained by an outlet at the base of the reactor.

The conditions of the simulations are selected such that the discharge can be reasonably expected to be operating in the inductive H-mode.

4.4.2 Mesh resolution and temporal convergence of the simulations

The mesh of the simulation 0.2 cm in the R and Z dimensions. The underlying structure of the HPEM involves the process of iterating through the modular solvers, as described in section 4.2. One complete cycle through the solvers is considered to be one iteration. The system evolves from one iteration to the next towards a steady state solution[163]. The steady state solution is assumed to be found once the change between iterations for the reactor averaged species and properties of the plasma is less than 0.1%. An example of the convergence of a simulation for an applied power of 300 W and a gas pressure of 20 Pa is shown in figure 4.3

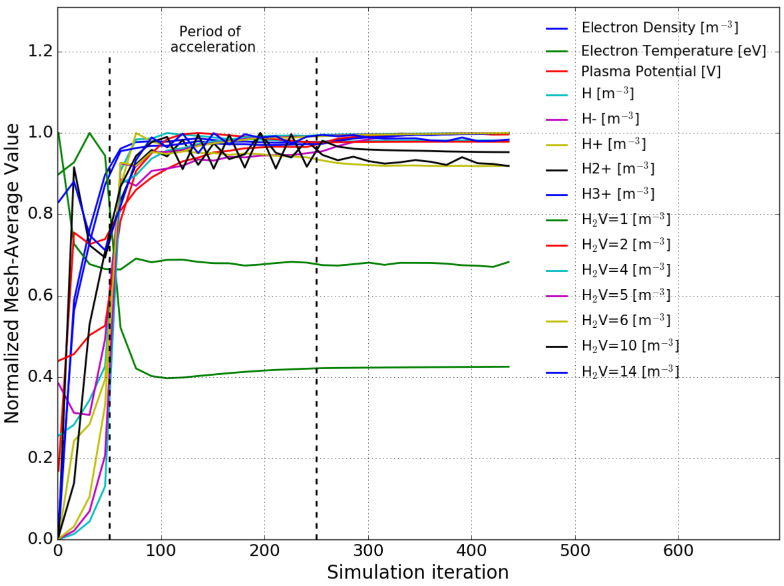

Figure 4.3: Iterative temporal convergence of the simulation of a GEC mesh geometry at a power of 300 W and 20 Pa.

Numerical acceleration is used to speed up the convergence rate of the FKPM module to decrease the run time of the simulations to practicable levels (approximately one month)[212]. The acceleration takes a specified averaging period and the densities of all of the species are linearly extrapolated. The acceleration is turned off prior to the end of the simulation to remove noise introduced into the simulations by the extrapolation process, as shown in figure 4.3.

4.4.3 Spatial profiles for electron density and temperature

The radial distribution of electron density and temperature is shown in figure 4.4 for the simulations and previously published experimental data of Ref. 208.

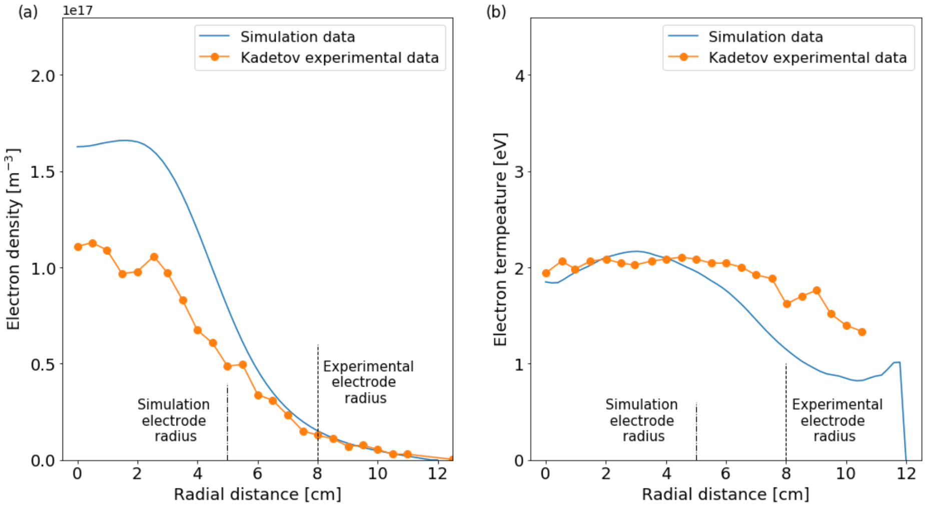

Figure 4.4: Comparison between experimental and simulation results for: (a) electron density and (b) electron temperature at 20 Pa. Experimental measurements taken by Kadetov in Ref. 208. Results compared at a spatial location 1.25 cm above the electrode in experiment and at Z = 6.8 cm in the simulations. Radius of the lower electrodes for the simulation and experimental data are shown. Applied power of 300 W and 20 Pa.

In figure 4.4 , the electron density is observed to be approximately 0.6 times higher than the experimentally measured electron density between a radial position of 0 cm and 5 cm.

The electron temperature across the reactor is shown in figure 4.4 (b). Qualitative agreement is observed between the simulation and the experiment. The smaller gap between the dielectric window and the electrode means that the power deposition to the plasma from the coil will be closer to the electrode, resulting in higher electron temperatures in this region[183,213,214].

Ref. 208 also includes measurements of the electron temperature, gas temperature and electron temperature from the centre of their GEC reactor. A comparison of these parameters with the simulation results under similar conditions is shown in figure 4.5.

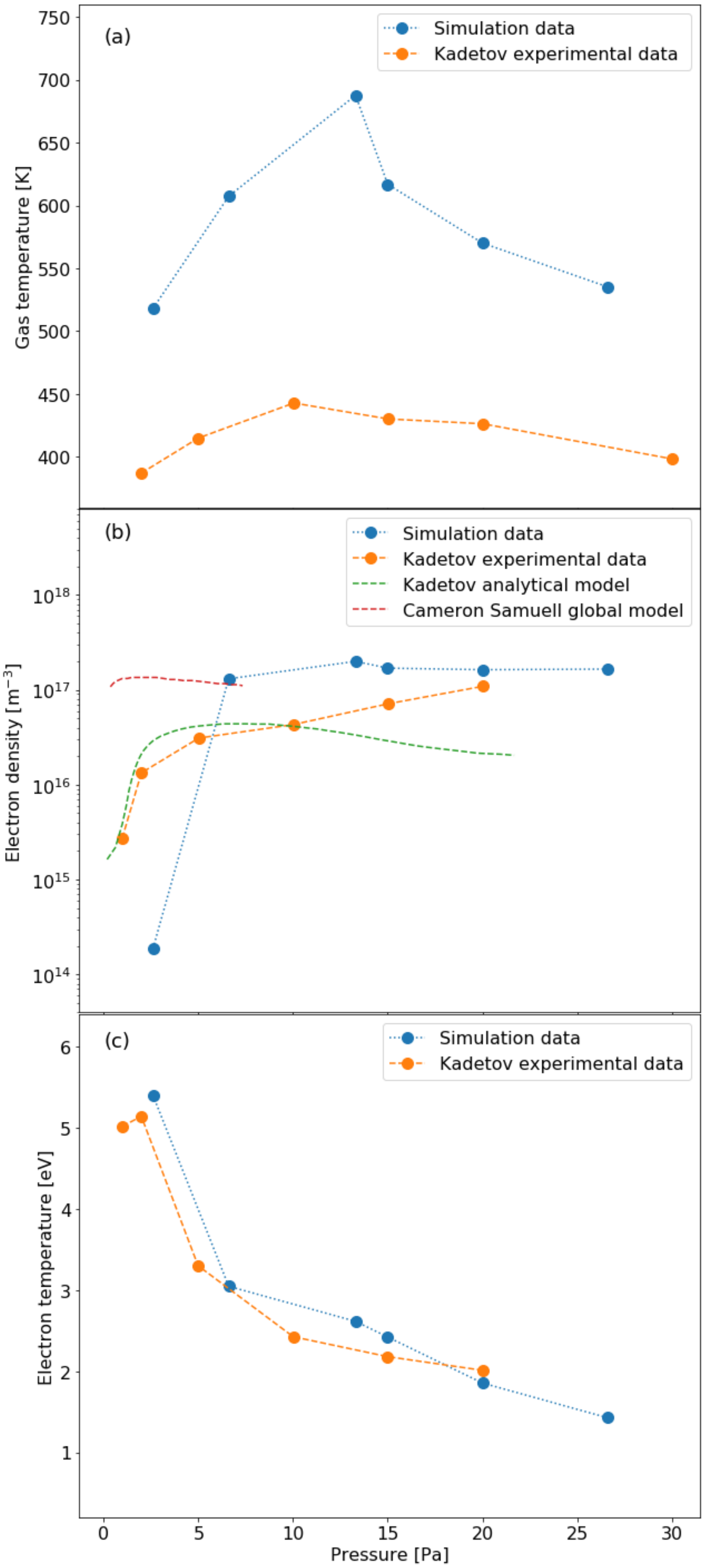

Figure 4.5: Electron density on axis at a position Z = 6.8 cm in the simulations and 1.25 cm above the electrode in the experimental data of Ref. 208, for (a) gas temperature (b) electron density and (c) electron temperature. Comparison data from an analytical model presented in Ref. 208 together with a 0D plasma chemistry (global) model from Ref. 48, are also included in (b). Dashed lines have been added to guide the eye.

It is observed in figure 4.5 (a) that the simulated gas temperature is higher than the experimentally observed gas temperature by a factor of approximately 0.75. The trends observed in the simulations appear to show an agreement to the experimental measurements. The gas temperature is observed to increase from 2 Pa to 13.3 Pa in the simulation and then to decrease as the pressure is increased from 13.3 Pa to 26.6 Pa. A similar trend is observed in the experimental measurements, where the gas temperature increases from 2 Pa to 10 Pa, and then decreases from 10 Pa to 30 Pa.

The effect of surfaces on the plasma properties is known to have a large influence on the plasma volume. Previous work has demonstrated that varying the thermal accommodation coefficient in HPEM simulations between 0.1 and 0.95 can cause the gas temperature in the bulk plasma to vary over almost one order of magnitude[186]. The simulations currently use an approximate thermal accommodation coefficient which is fixed for all materials and pressures. It is reasonable to suggest a better approximation of this value in the simulations for all materials may improve the agreement to the experimental measurements.

The electron density is shown in figure 4.5 (b) with two additional data sets, an analytical model created by Kadetov, and a global model produced by Samuell and Corr[48]. It is observed that in the global model and analytical model the electron density can be expected to increase from a low pressure to a peak density between 2 Pa and 7.5 Pa respectively, before decreasing as pressure is increased further. In the experiment, the electron density is observed to increase consistently from 2 Pa to 20 Pa.

The electron temperature is shown for increasing gas pressure in figure 4.5 (c). The electron temperature is observed to follow the trend observed in the experimental data. The maximum electron temperature is observed at 2.6 Pa, which decreases at a similar rate to the electron temperature observed in the experiment as the gas pressure increases.

In the simulations, it is observed in figure 4.5 that the electron density is higher than the experimental data. As the simulation domain is slightly different to the reactor geometry used in the simulations, with 1 cm (20% smaller) gap between the dielectric window and the electrode, the observation of a higher electron density is consistent with relatively high power density. The trend observed is consistent with that observed in the experimental data. An increase in the electron density is observed between 2.6 Pa and 6.6 Pa after which the electron density remains relatively constant as the pressure increases further.

Overall, a reasonable level of qualitative and quantitative agreement is observed for the simulation, as compared to previously published experimental, simulation and analytical results.

4.5 Chapter summary

In this chapter, the Hybrid Plasma Equipment Model is introduced as a means to model low temperature hydrogen plasmas in two dimensions, accounting for the full manifold of vibrational states and self-consistent treatment of spatial heating. The addition of gas temperature dependent reaction rates means the distribution of species in the plasma is influenced by the temperature of the background gas, which is of interest when studying the distribution of vibrational states. The radial distributions of electron density and the electron temperature are compared to previously published experimental measurements in a similar reactor, showing reasonably good qualitative and quantitative agreement.

Chapter 5

Effect of the gas pressure and spatially resolved gas heating on vibrational kinetics and negative ion production

Following the development of the hydrogen reaction set in chapter 4, the results of simulations in a GEC reactor are presented. The simulations resolve the spatial distribution of plasma parameters and vibrational states as they respond to gas heating, which is important for the production of negative ions. The impact of self consistently determining the spatial distribution of the gas temperature, as distinct from setting it as isothermal, is investigated.

5.1 Macroscopic plasma parameters

In the following sections, the spatial distribution of the electron density, electron temperature, plasma potential, and gas temperature are considered. This is followed by consideration of the atomic hydrogen and negative ion spatial distributions to obtain an overview of the plasma response at 6.6 Pa, 13.3 Pa, 15 Pa, and 20 Pa at 300 W applied power. These observations form the basis of the interpretation of the production of negative ions with respect to vibrational kinetics and gas temperature in section 5.2.

5.1.1 Electron density

Figure 5.1 shows the spatial distribution of electron density with respect to pressure.

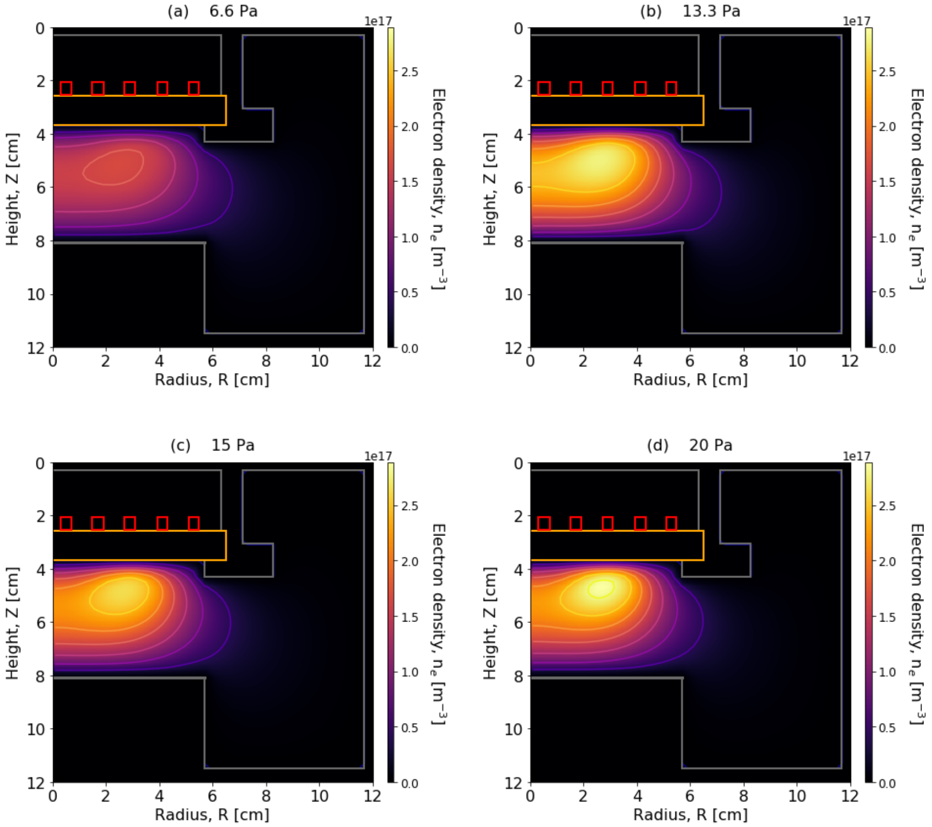

Figure 5.1: Electron density for gas pressures of (a) 6.6 Pa, (b) 13.3 Pa, (c) 15 Pa, and (d) 20 Pa at 300 W applied power.

As shown in figure 5.1, the electron density has a lobe structure with the maximum density positioned beneath the dielectric window, between R = 2.4 - 2.6 cm and Z = 5.0 - 5.2 cm. In figure 5.1 (a) for a pressure of 6.6 Pa, the maximum electron density is observed to be 1.6×10^{17} m^{-3}, this increases to 2.8×10^{17} m^{-3} at a pressure of 13.3 Pa in figure 5.1 (b) with very little observable change in the overall distribution of the plasma. The maximum electron density is observed to decrease from 13.3 Pa to 15 Pa in figure 5.1 (c) from 2.8×10^{17} m^{-3} to 2.6×10^{17} m^{-3}, after which the electron density increases again from 2.6×10^{17} m^{-3} at 15 Pa to 2.9×10^{17} m^{-3} at 20 Pa.

It is useful to consider the changes in electron density (n_e) and electron temperature (T_e) in terms of power and particle balance for variations in the pressure of a plasma. Under these electrical conditions the electrical energy from the coil can be reasonably expected to be primarily coupled to the electrons and the absorption of energy by the ions will be negligible[1]. At lower pressures, the production of electrons can be expected to be reduced due to a reduction of the number of gas particles available for ionisation. A reduction in the number of particles in the reactor means that the electrons have a longer mean free path and so more readily reach the walls of the reactor to be lost from the system. This means that a lower electron density can be expected at low pressures. In contrast to this, at higher pressures, the electron-neutral collision frequency increases and the mean free path decreases. This reduces the loss of electrons to the surfaces of the reactor. This means that the electron density can be expected to increase as the pressure is increased due to a reduction in the loss of electrons from the plasma volume to the walls. In combination with a reduction in the loss of electrons from the plasma to the walls, inelastic collisions between the electrons and the background neutral gas will increase as the pressure in the reactor increases. An increase in the inelastic collisions will reduce the average energy of the electrons. This will reduce the number of high energy electrons in the plasma. High energy electron are necessary to cause ionisation reactions in the plasma. This means that an increase in the electron density through a reduction in the loss of electrons to the walls of the reactor is offset by a reduction in the production of electrons through ionisation reactions[1]. Higher electron densities have previously been observed in this pressure range in the global model in Ref. 48 and the analytical model according to Ref. 208. In general, the lobed spatial distribution and increase in density is consistent with that observed in other simulations of planar coil ICPs[214–218].

5.1.2 Electron temperature

The spatial distribution of the electron temperature with respect to pressure is shown in figure 5.2.

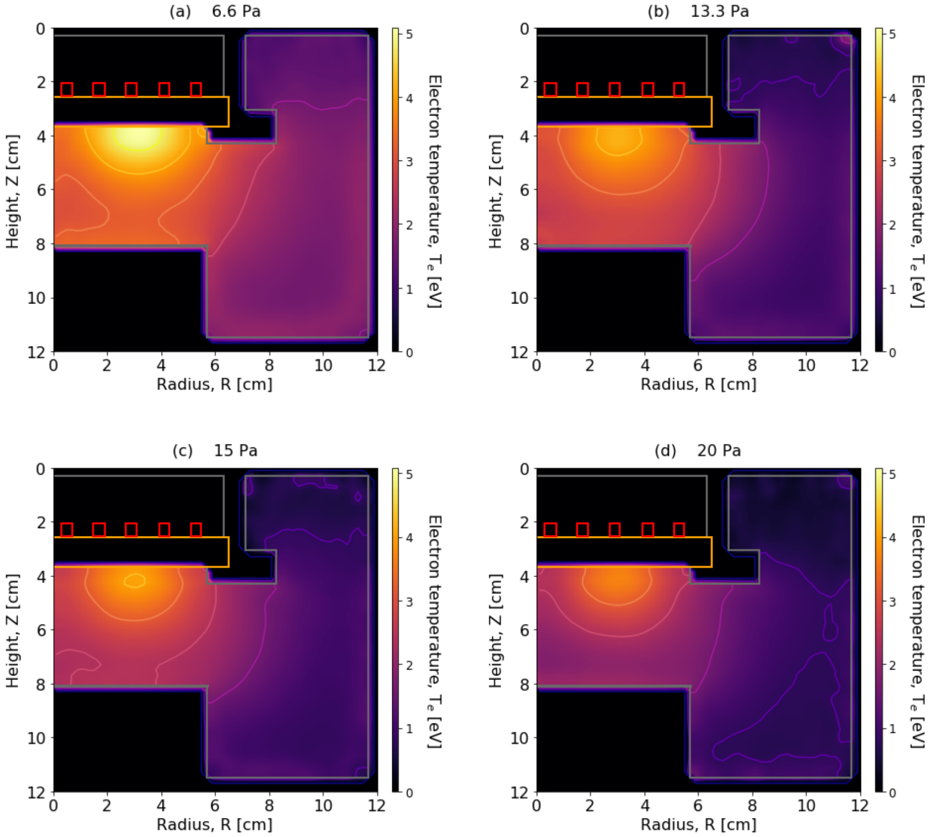

Figure 5.2: Electron temperature for gas pressures of (a) 6.6 Pa, (b) 13.3 Pa, (c) 15 Pa, and (d) 20 Pa at an applied power of 300 W.

In figure 5.2 we observe that the electron temperature peaks away from the axis of the reactor, at a radial position of R = 3 cm and axial height of Z = 4 cm. This is the location where power is deposited in the plasma and is similar to results in other work with a planar coil[183,213,214]. The electron temperature within the reactor is observed to decrease as pressure is increased. In figure 5.2 (a), the maximum electron temperature in the reactor is 5.1 eV, this decreases to 4.2 eV at 13.3 Pa in figure 5.2 (b), and again at 15 Pa in figure 5.2 (c) to 4.0 eV until at 20 Pa it reaches 3.7 eV in figure 5.2. As previously discussed in section 5.1.1, a higher gas pressure increases the likelihood of electrons colliding with neutral gas particles in the reactor, which decreases the mean free path of the electrons. More frequent inelastic collisions between the electrons and the background gas reduces the average energy of the electrons in the plasma, which is observed as a reduction in the electron temperature[1,2]. This appears to align with what is observed in the simulations, where the electron density increases gradually as the pressure is increased and the average electron temperature decreases as the pressure is increased.

5.1.3 Plasma potential

The plasma potential with respect to pressure is shown in figure 5.3.

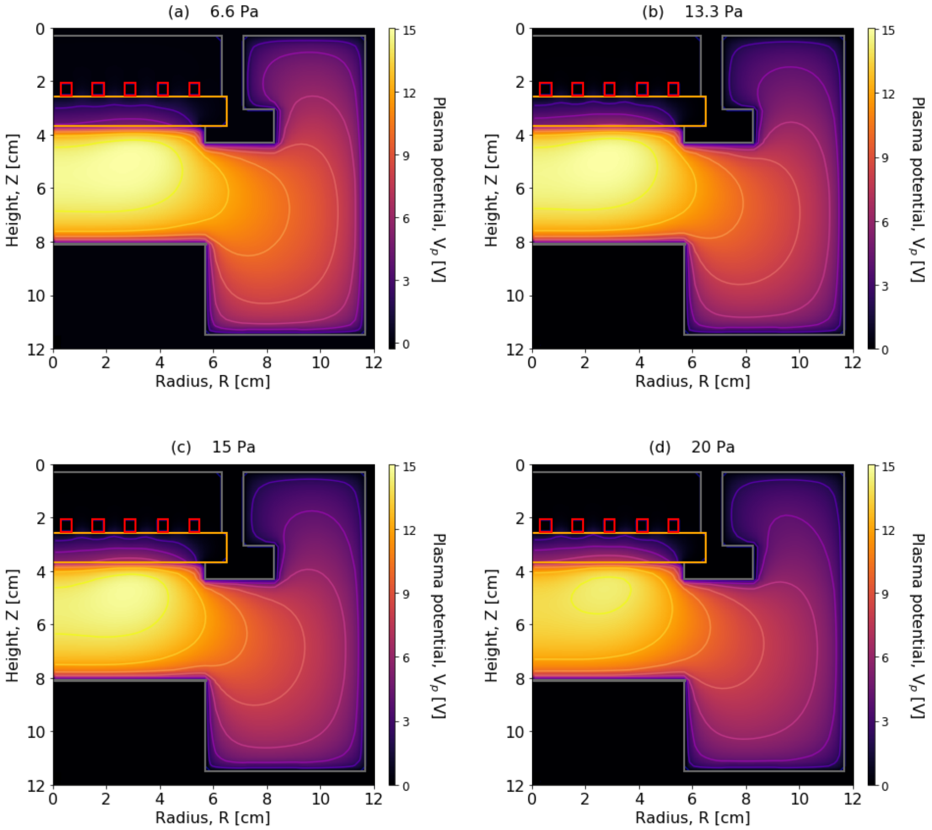

Figure 5.3: The plasma potential at gas pressures of (a) 6.6 Pa, (b) 13.3 Pa, (c) 15 Pa, and (d) 20 Pa for an applied power of 300 W.

The plasma potential in figure 5.3 is observed to be relatively constant as the pressure increases from 6.6 Pa to 20 Pa. In figure 5.3 (a) at 6.6 Pa, the maximum plasma potential is 15.0 V which decreases to 14.3 V in figure 5.3 (d) at 20 Pa. It is observed that the position of the maximum plasma potential changes as the pressure is increased. In figure 5.3 (a) at 6.6 Pa the position of the maximum is at $R = 2.4$ cm and $Z = 5.2$ cm, whilst in figure 5.3 (d) the position of maximum plasma potential is at $R = 2.6$ cm and $Z = 4.8$ cm. This movement in the maximum potential suggests that increasing the pressure confines the plasma closer to where the power is deposited and agrees with the increase in plasma density observed in figure 5.1.

5.1.4 Gas temperature

The spatial distributions of the gas temperature with respect to pressure is shown in figure 5.4.

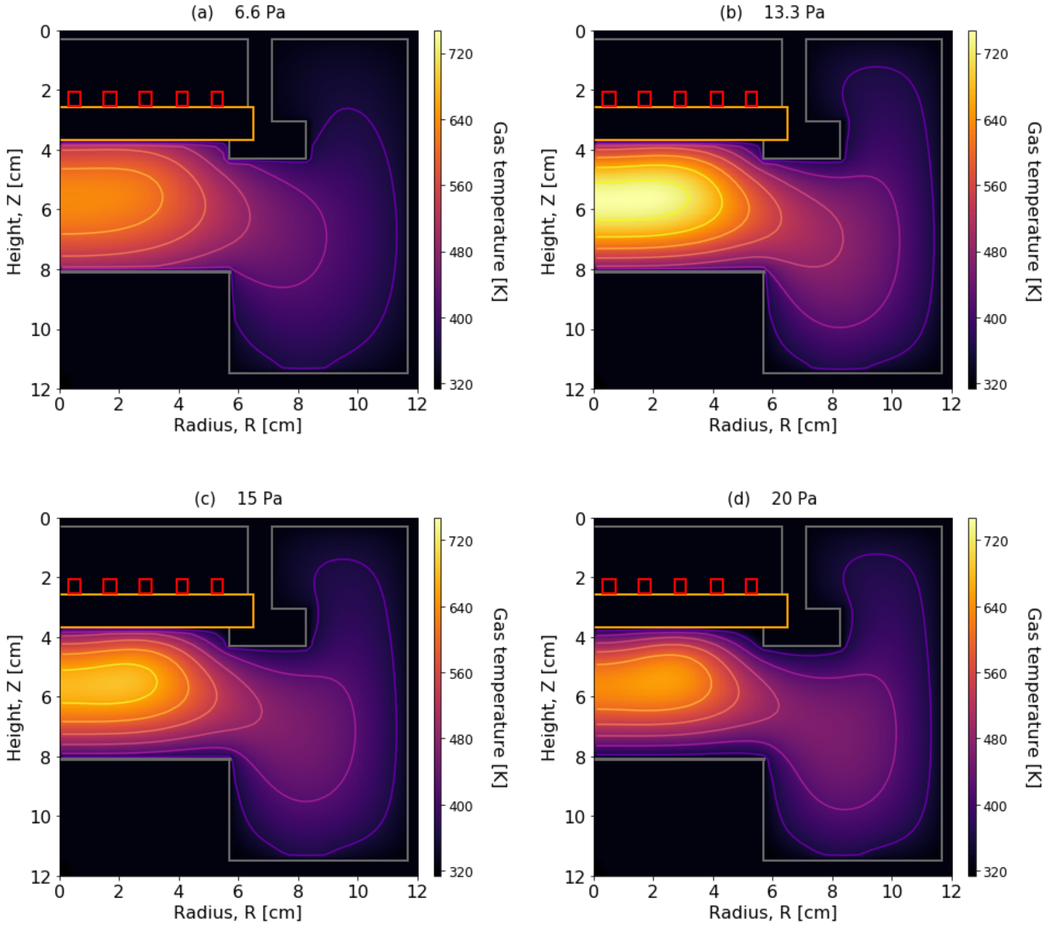

Figure 5.4: Gas temperature at a gas pressure of (a) 6.6 Pa, (b) 13.3 Pa, (c) 15 Pa, and (d) 20 Pa with an applied power of 300 W.

It is observed in figure 5.4 that the gas temperature within the reactor is at a maximum between the electrode and the dielectric window for all gas pressures. The gas temperature is observed to be at a maximum in figure 5.4 (b) for a gas pressure of 13.3 Pa, reaching approximately 750 K. The location of the maximum gas temperature moves as the pressure is increased. In figure 5.4 (a), the maximum is on axis at a height of $Z = 5.8$ cm. Increasing the pressure to 13.3 Pa in figure 5.4 (b), the position of the gas temperature maximum moves outwards to a radial position of $R = 1.2$ cm. Further increases in gas pressure in figure 5.4 (c) and figure 5.4 (d) increases the radial distance to $R = 1.8$ cm and $R = 2.2$ cm respectively. At all pressures the gas temperature is relatively hot in the centre of the plasma and decreases from the centre of the plasma to a temperature of approximately 450 K close to the walls of the reactor.

5.1.5 Atomic hydrogen

The spatial distributions of atomic hydrogen with respect to pressure is shown in figure 5.5.

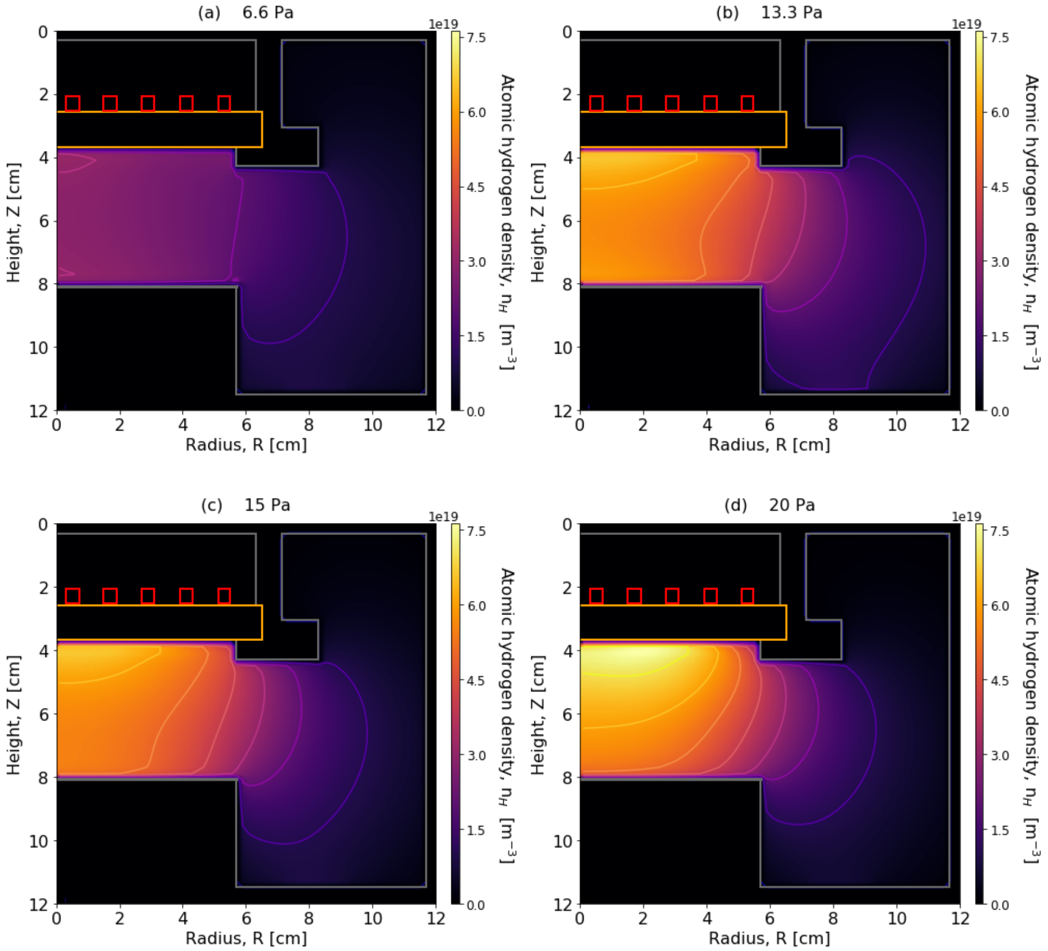

Figure 5.5: Atomic hydrogen density distribution for a gas pressure of (a) 6.6 Pa, (b) 13.3 Pa, (c) 15 Pa, and (d) 20 Pa at an applied power of 300 W.

As shown in figure 5.5, the maximum atomic hydrogen density increases as the pressure of the gas increases. The increase is from 3.1×10^{19} m^{-3} at 6.6 Pa in figure 5.5 (a) to 7.6×10^{19} m^{-3} at 20 Pa in figure 5.5 (d). This is consistent with an increase in the electron-neutral collision frequency for increasing pressure. The distribution of the atomic hydrogen is observed to be fairly uniform within the space between the electrode and dielectric window at pressure of 6.6 Pa and 13.3 Pa in figures 5.5 (a) and (b) respectively, whilst at 15 Pa and 20 Pa a peak in the density is observed closer to the dielectric window.

5.1.6 Dissociation degree

The dissociation degree is shown with respect to pressure in figure 5.6.

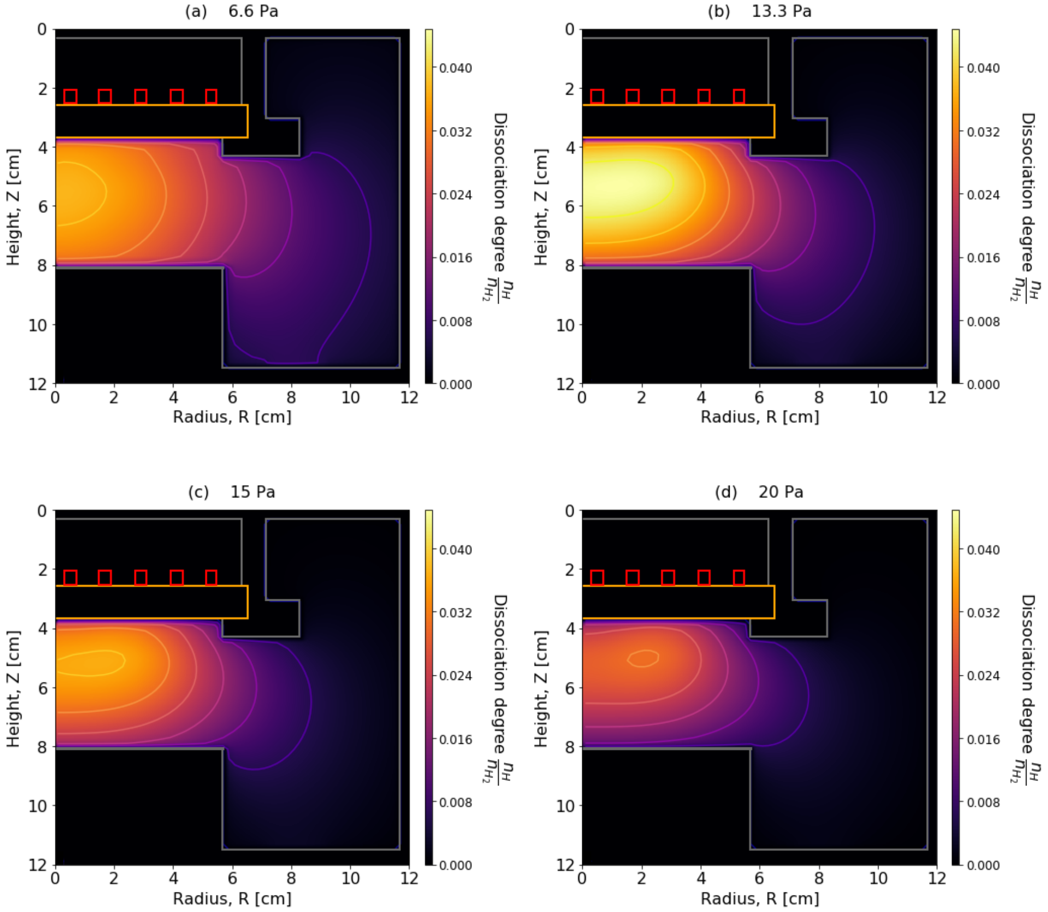

Figure 5.6: Dissociation degree at a gas pressure of (a) 6.6 Pa (b) 13.3 Pa (c) 15 Pa (d) 20 Pa for an applied power of 300 W.

The dissociation degree of hydrogen is observed as being highest closer to the centre of the reactor. This is not observed in the atomic hydrogen distribution. The dissociation degree is observed as being highest in figure 5.6 (b) at a pressure of 13.3 Pa. Comparing the dissociation degree to the gas temperature shown in figure 5.4, we observe that they are maximised in similar locations.

The observation of a higher dissociation at a pressure of 13.3 Pa is consistent with previous work in a similar GEC reactor. Here it was observed that the dissociation degree increased from 6.6 Pa to a maximum at 10 Pa after which it decreased as pressure is increased further[209].

5.1.7 Density of negative ions, n_{H^-}

Of particular relevance for this thesis is the distribution of negative ions within the plasma. As described in chapter 4, section 4.3, the production of negative ions in the simulations is solely via the two step process of vibrational excitement of molecular hydrogen, followed by dissociative attachment. The spatial distribution of negative ions is shown in figure 5.7.

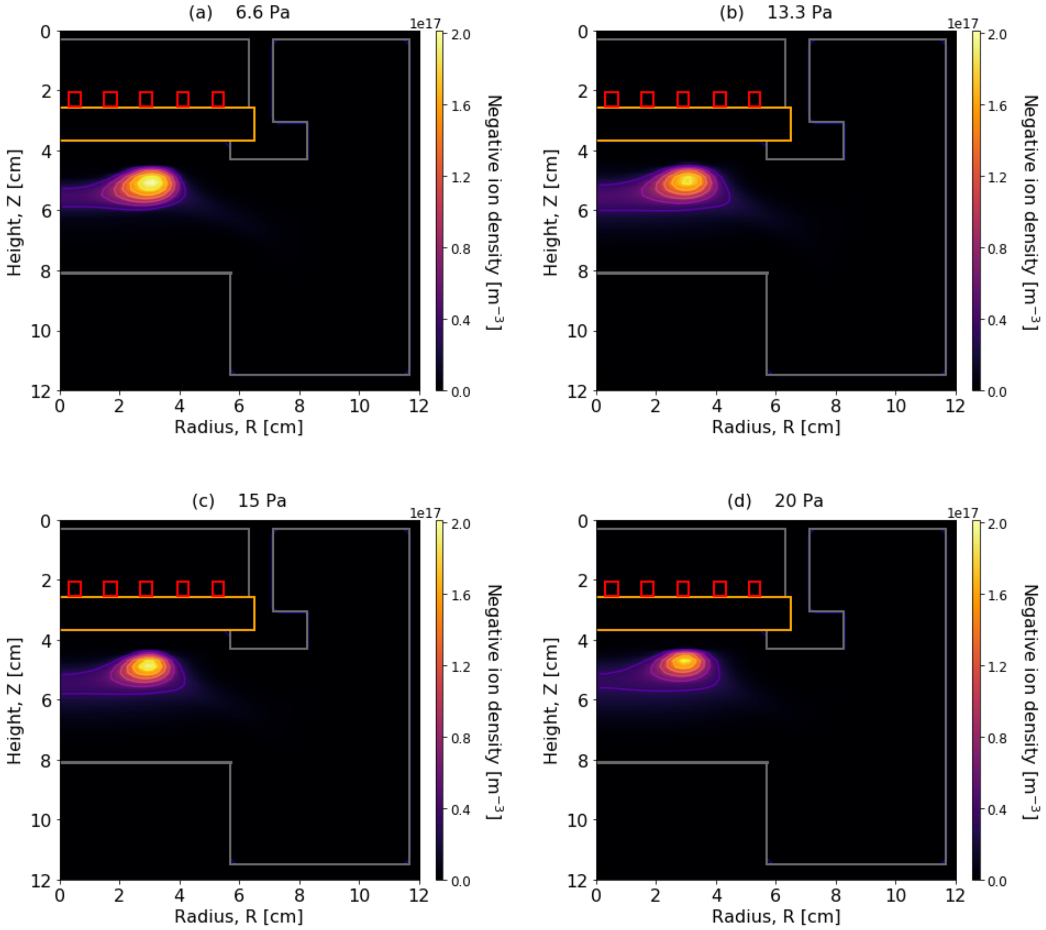

Figure 5.7: Negative atomic hydrogen ion density distributions at gas pressures of (a) 6.6 Pa, (b) 13.3 Pa, (c) 15 Pa, and (d) 20 Pa for an applied power of 300 W.

It is observed in figure 5.7 that the negative ion density is confined in the centre of the plasma between the dielectric window and electrode with a maximum density of $2{\times}10^{17}$ m^{-3} at a pressure of 6.6 Pa in figure 5.7 (a). The position of maximum density is the same for gas pressures of 6.6 Pa and 13.3 Pa in figures 5.7 (a) and (b), at a radial position of $R = 3$ cm and an axial height of $Z = 5.2$ cm. As the pressure is increased the position of maximum density is observed to move closer to the radial axis of the reactor and the dielectric window, with the radial position of the maximum moving to $R = 2.8$ cm and axial position of the maximum moving to $Z = 5$ cm and $Z = 4.8$ cm in figures 5.7 (c) and (d) at 15 Pa and 20 Pa, respectively.

As described in chapter 1, negative ions are confined to the centre of a plasma by the positive potential of the plasma. Comparing the position of the maximum negative ion density to the location of maximum plasma potential observed in figure 5.3, it is noted that the axial position of the maximum negative ion density is the same for each pressure, but the radial position of the maximum negative ion density is not.

5.1.8 Electronegativity of the hydrogen plasma, n_{H^-}/n_e

A measure of the influence negative ions have on the plasma as a whole can be given by taking a ratio of the negative ion density compared to the electron density within the plasma. This ratio is termed the electronegativity of the plasma. The spatial distribution of the electronegativity is shown in figure 5.8.

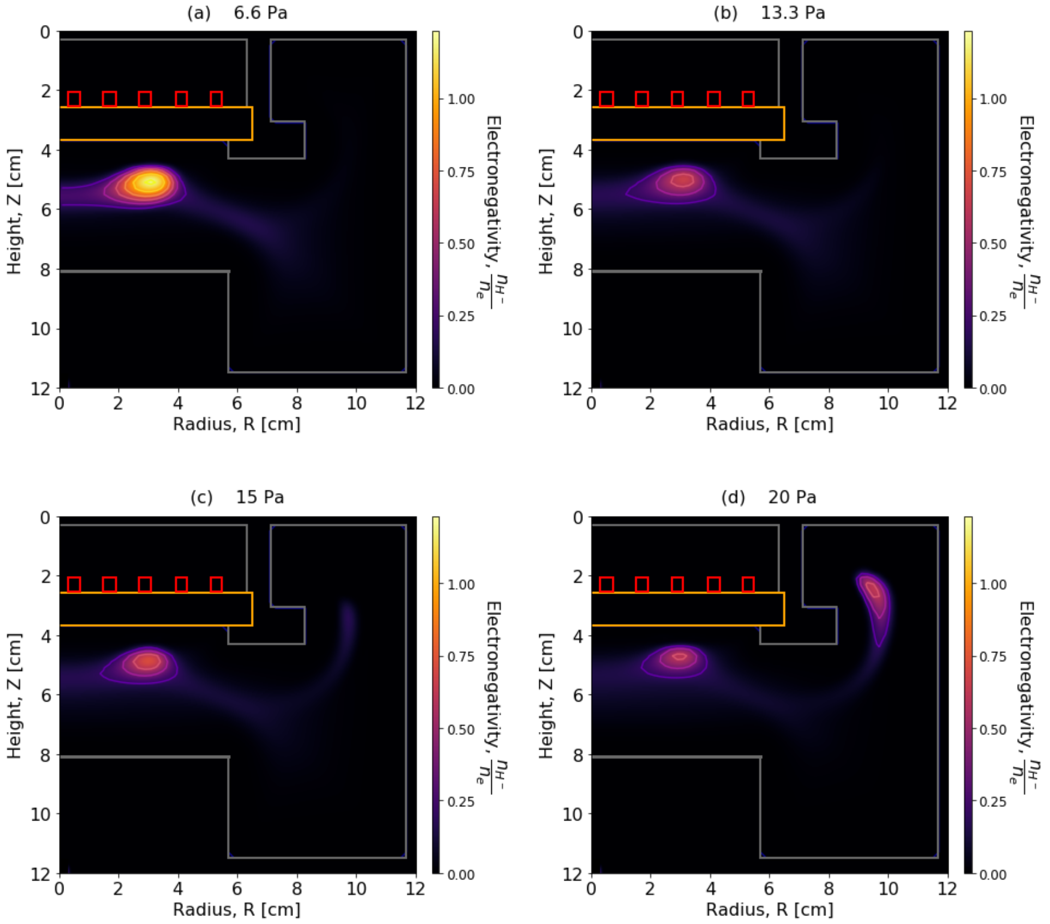

Figure 5.8: Electronegativity within the reactor at gas pressures of (a) 6.6 Pa, (b) 13.3 Pa, (c) 15 Pa, and (d) 20 Pa for an applied power of 300 W.

It is observed in figure 5.8 that the electronegativity has a maximum centred at all pressures between the electrode and dielectric window. At 6.6 Pa, in figure 5.8 (a), the electronegativity is at a maximum at R = 3 cm and Z = 5.2 cm, with a value of 1.23. A value above 1 for the electronegativity of the plasma suggests that the dominant behaviour of the negative charge within the plasma is determined by the properties of the negative ions[1]. It is observed in figure 5.8 (b) and (c) that the electronegativity at a similar location to figure 5.8 (a) decreases from 1.23 to 0.67 and 0.74 respectively as the pressure is increased. This is in line with the observation in figure 5.7 that the negative ion density decreases as the pressure in the reactor is increased, whilst the electron density observed in figure 5.1 is observed to increase as the pressure is increased. It is also observed in figure 5.8 (d), and to a smaller extent in figure 5.8 (c) that the electronegativity increases in the region outside of the gap between the electrode and the dielectric window. It is unclear why this is the case, but it is reasonable to suggest that the electrons do not diffuse to this region due to the higher gas pressure.

5.2 Spatial distribution of H_2 vibrational states

The mechanisms for the production of vibrational states within a hydrogen plasma has been extensively studied via both simulations and experiments[104–106,219]. The vibrational energy distribution in a hydrogen plasma has been shown to have a particular structure, with a superthermal plateau existing for the vibrational states $v = 3$ to $v = 10$ where electron energies are high enough to excite the hydrogen molecules. This plateau is caused by the interaction of EV reactions, which favour the production of higher vibrational levels between $v = 5$ and $v = 14$, and the suppression of these vibrational states by the atomic V-T reactions[60].

To investigate the impact of gas pressure on vibrational kinetics in the planar ICP, we focus on the maximum and minimum pressure cases, 6.6 Pa and 20 Pa. These are also the pressures where the maximum and minimum negative ion densities are observed in figure 5.7. As the distribution of vibrational states is low in the region outside of the gap between the dielectric window and the electrode, and this is the region where the negative ions are formed, a region of interest is focused upon. This is shown in figure 5.9

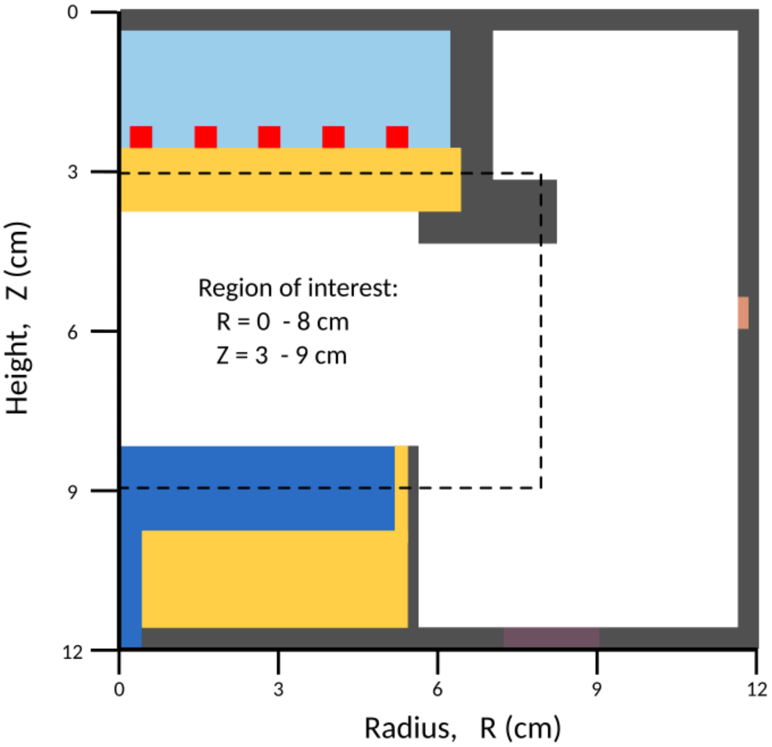

Figure 5.9: Schematic of the simulation domain, as shown previously in figure 4.2, identifying the region of interest for study of H_2 vibrational states. Region of interest encompasses an axial distance of $Z = 3$ cm to $Z = 9$ cm, and a radial distance $R = 0$ cm to $R = 8$ cm.

The vibrational states spatial distribution within the region of interest is shown in figure 5.10 for a pressure of 6.6 Pa and applied power of 300 W.

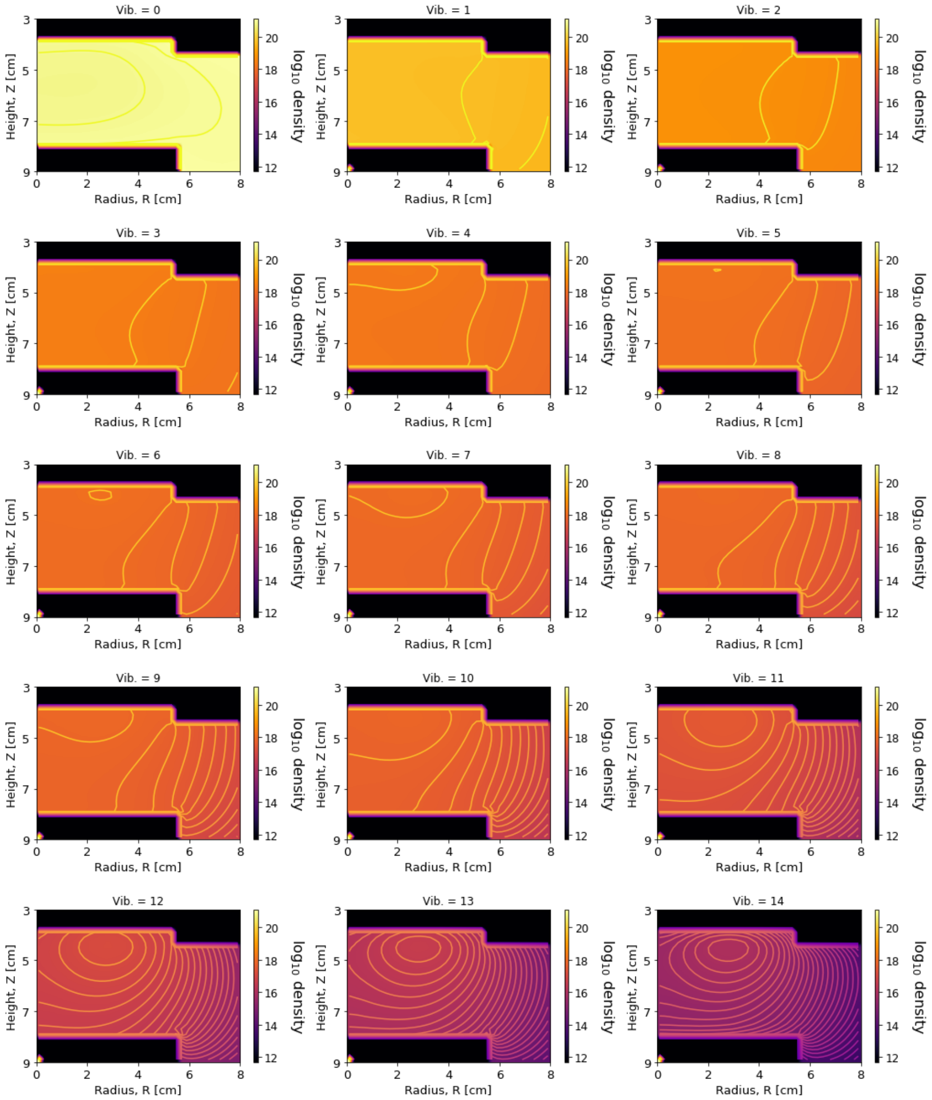

Figure 5.10: Vibrational density distributions for $v = 0$ and $v = 14$ at a gas pressure of 6.6 Pa and applied power of 300 W.

The distribution of vibrational states in figure 5.10 is observed to be almost uniform across the plasma for the first 5 vibrational states ($v = 0$ to $v = 5$). From $v = 0$ to $v = 2$, it is observed that the maximum vibrational density decreases by more than 2 orders of magnitude. At $v = 2$, the maximum density is observed to be on axis of the reactor and close to the dielectric window and the electrode. Going to the higher vibrational densities, between $v = 3$ and $v = 7$, the maximum vibrational density is observed to decrease by a factor of 0.4. It is also observed that the vibrational states appear to move towards the dielectric window in the region of interest. The density of the vibrational states at positions more than $R = 5$ cm are also observed to decrease as the vibrational energy is increased past $v = 7$. For $v = 3$, the vibrational density at a radial position $R = 6$ cm and axial height of $Z = 5$ cm is a factor 3 higher than the density observed for $v = 7$ at a similar location.

This suggests that the higher vibrational states do not diffuse as far as the lower vibrational states, or the rates of their production are not as high in this location. This is consistent with the observation of electron temperatures in figure 5.2 (a) being highest between the dielectric window and the electrode.

As the vibrational energy is increased past $v = 7$, the maximum density of the state decreases further. For $v = 7$ to $v = 10$ the maximum observed density decreases by a factor of 0.45 and then from $v = 10$ to $v = 14$ the maximum density decreases again by 2 orders of magnitude. For vibrational states above $v = 12$, the location of maximum vibrational density is observed to be at a position within the plasma volume. This is observed at a radial location of $R = 3.0$ cm and $Z = 4.6$ cm for $v = 14$. This location within the plasma is the same radial distance of the location of maximum negative ion density observed at a gas pressure of 6.6 Pa in figure 5.7 (a), but 0.6 cm nearer the dielectric window than the position of maximum negative ion density. This location for the maximum appears to be consistent with the position of maximum electron temperature, which was observed at a radial position of $R = 3.2$ cm and axial position of $Z = 3.8$ cm.

To contrast the low pressure case at 6.6 Pa, figure 5.11 shows the spatial distribution for a gas pressure of 20 Pa.

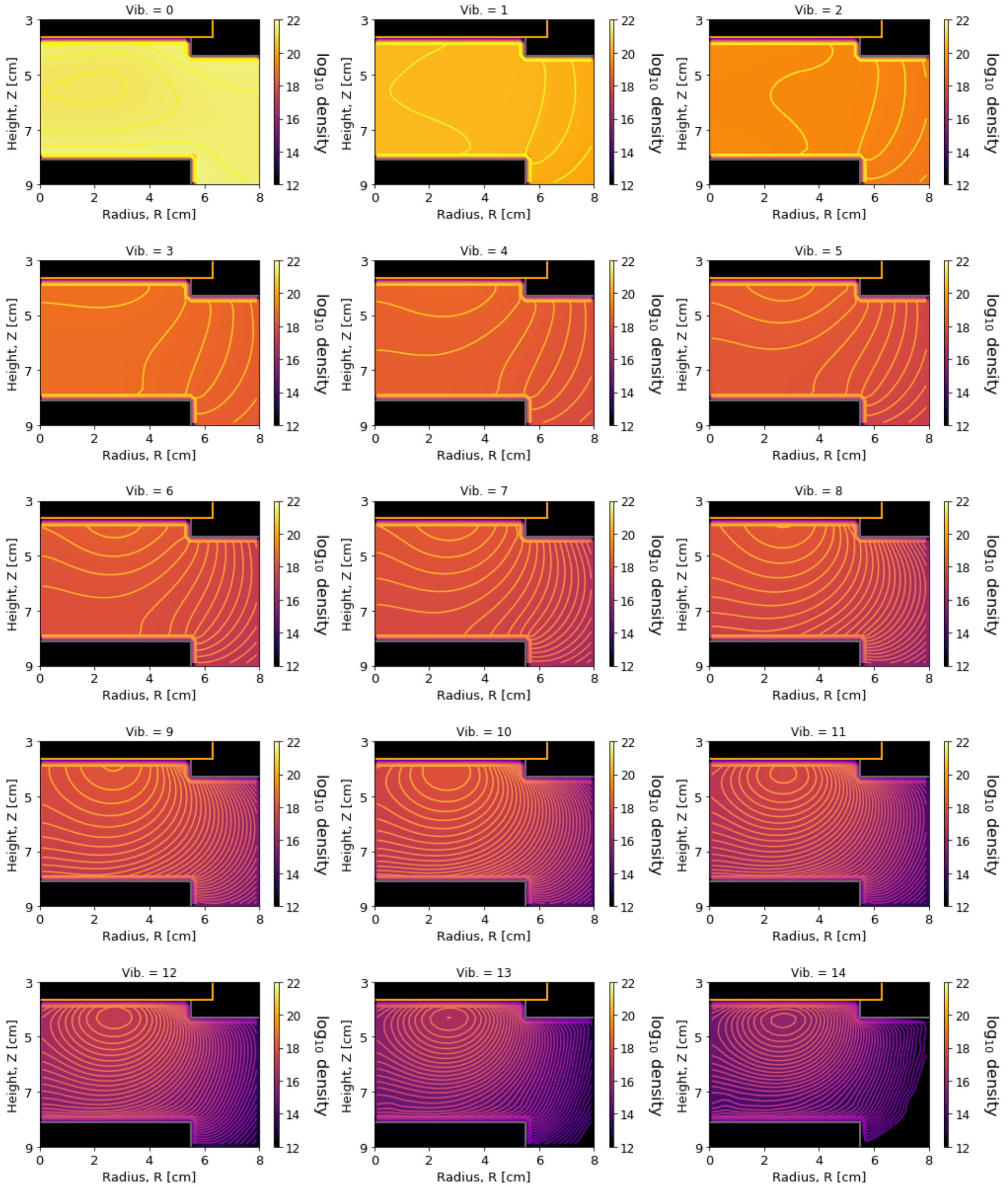

Figure 5.11: Vibrational density distributions for $v = 0$ and $v = 14$ at a gas pressure of 20 Pa and applied power of 300 W.

The distribution of vibrational states in figure 5.11 is observed to be relatively uniform, in a similar manner to 6.6 Pa across the region of interest, but instead of this being the case for the first 5 vibrational states, at 6.6 Pa, at 20 Pa the uniformity is only observed for the first 3 vibrational states ($v = 0$ to $v = 2$). Similarly to figure 5.10 at 6.6 Pa, from $v = 0$ to $v = 2$, it is observed that the vibrational density decreases by more than 2 orders of magnitude. At $v = 2$, the maximum density is observed to be on the axis of the reactor, close to the dielectric window and the electrode. Going to the higher vibrational densities, between $v = 3$ and $v = 7$, the maximum vibrational density is observed to decrease by a factor of 5. This is much larger than the observed decrease at a pressure of 6.6 Pa. The density of the higher vibrational states are also observed to decrease much more at the edges of the reactor at 20 Pa compared to 6.6 Pa. For $v = 3$, the vibrational density at a radial position $R = 6$ cm and axial height of $Z = 5$ cm is a factor 14 higher than the density observed for $v = 7$ at a similar location. This reduction is much larger at 20 Pa than at 6.6 Pa. This suggests that the higher vibrational states at higher pressures do not diffuse as far at lower pressures.

As the vibrational energy is increased past $v = 7$, the maximum density decreases further. For $v = 7$ to $v = 10$ the density decreases by a factor of 1.6 and then from $v = 10$ to $v = 14$ the maximum density decreases again by 2 orders of magnitude. Similarly to the case at 6.6 Pa, the vibrational states above $v = 11$ have a maximum within the plasma volume, as opposed to on the dielectric surface as observed for the other lower vibrational states. This is observed at a radial location of $R = 2.8$ cm and $Z = 4.4$ cm for $v = 14$ at 20 Pa. This location within the plasma is the same radial distance of the location of maximum negative ion density observed at a gas pressure of 20 Pa in figure 5.7 (d), and 0.4 cm closer to the dielectric.

Compared with figure 5.11, the vibrational states at 20 Pa have a larger gradient between the maximum density observed for each state and the edge. This suggests that the distribution of vibrational energy is more confined. It is reasonable to expect this as a higher gas pressure will increase the number of collisions between molecules that in general will decrease the population of vibrationally excited states via collisional quenching.

To help visualise how the vibrational states are distributed across the radial dimension of the reactor, i.e. that of particular interest for uniformity in plasma manufacturing, the radial plane at a height of $Z = 5$ cm is taken across the region of interest. This is shown for the minimum and maximum pressure cases, 6.6 Pa and 20 Pa, in figure 5.12.

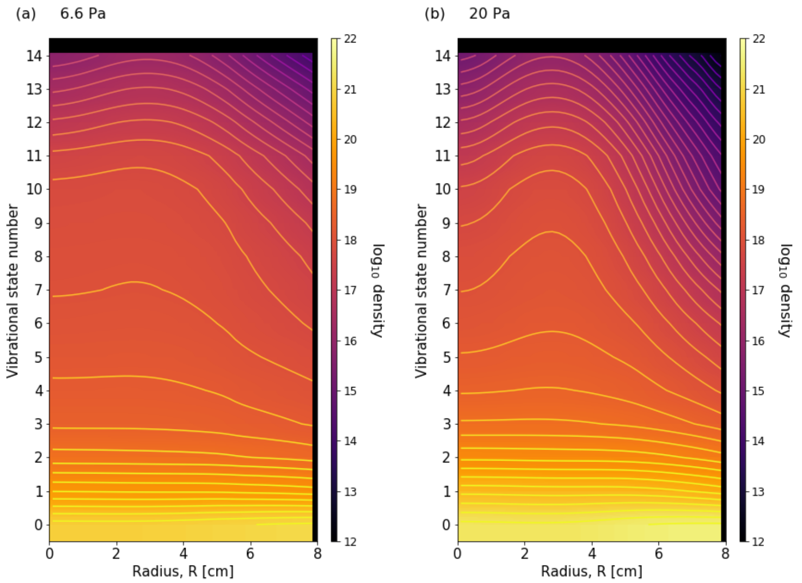

Figure 5.12: Vibrational density distributions between v = 0 and v = 14 at R = 3 cm for (a) 6.6 Pa and (b) 20 Pa with an applied power of 300 W.

The distribution of the vibrational states at 6.6 Pa in figure 5.12 (a) decrease from a maximum at $v = 0$ to a minimum at $v = 14$. The rate of this decrease is observed to be much slower at the vibrational states between $v = 4$ and $v = 10$, where it is observed that the contour lines are much further apart. Across the radius of the region of interest at 6.6 Pa it is observed that the density of the vibrational states stays constant from $R = 0$ cm to $R = 4$ cm ,before decreasing at $R > 4$ cm.

In contrast to this, at 20 Pa in figure 5.12 (b), the density of vibrational states at $R = 3$ cm from $v = 0$ to $v = 14$ is observed to be similar to 6.6 Pa, which suggests a similar rate of production, however, the distribution radially is observed to be quite different. The density of the vibrational states on axis is observed to be much lower than at 6.6 Pa, which increases as radial distance is increased to a maximum at $R = 3$ cm, before decreasing for $R > 3$ cm. It is also observed that the density of the higher vibrational states where $v > 8$ and $R > 7$ is lower than the density of any vibrational state density observed at 6.6 Pa.

The results in figure 5.12 highlight that the vibrational states are influenced by the gas pressure. It is reasonable to suggest that the higher pressure prevents the diffusion of the highest vibrational states to region away from where they are produced, which is the location with the highest electron temperature.

Figure 5.13 shows the vibrational density distribution for a fixed point in the reactor, at $R = 3$ cm and $Z = 5$ cm which is where the maximum vibrational density is observed for the highest vibrational states at 6.6 Pa and 20 Pa. Also shown is the vibrational density at $R = 6$ cm and $Z = 5$ cm which, in relation to figure 5.10 and figure 5.11, is where it was observed that there was a large change in the vibrational density distribution between 6.6 Pa and 20 Pa.

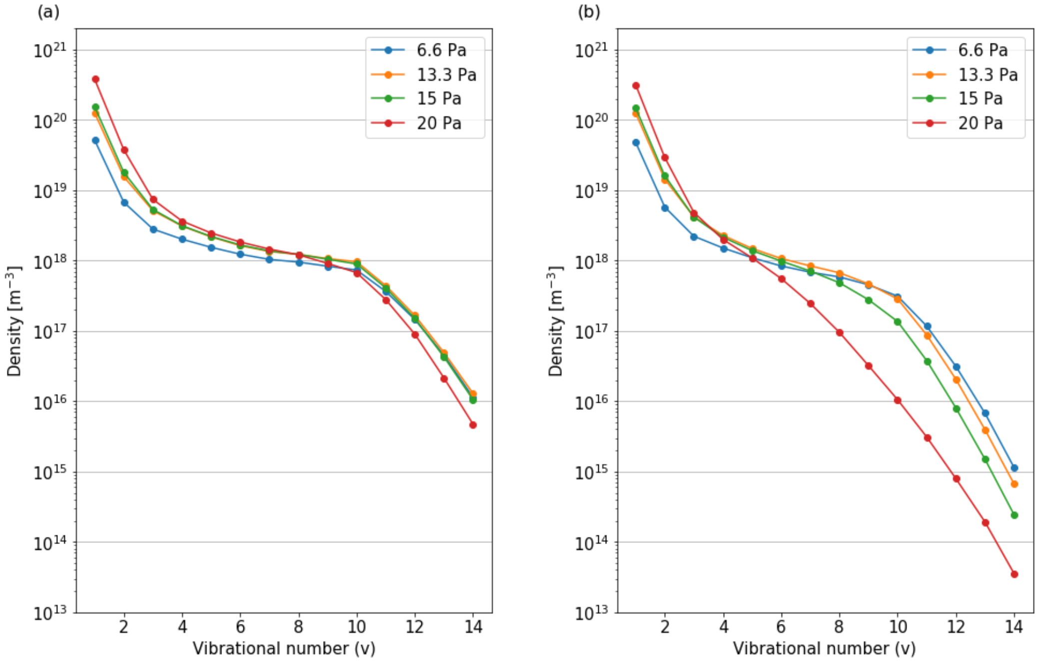

Figure 5.13: Vibrational density comparison at pressures of 6.6 Pa, 13.3 Pa, 15 Pa, and 20 Pa for (a) $R = 3$ cm and $Z = 5$ cm and (b) $R = 6$ cm and $Z = 5$ cm at an applied power of 300 W.

As described previously in this section, the distribution of vibrational energy in the plasma can create a superthermal plateau. In figure 5.13 (a), the distribution of vibrational energy at a location close to the maximum observed density for each state is shown. The superthermal distribution is clearly observed at all pressures. At the location $R = 3$ cm and $Z = 5$ cm and for a pressure of 20 Pa, it is observed that the density of the vibrational states between $v = 1$ and $v = 9$ is higher than the lower pressure cases. This is consistent with expectation because as the overall gas pressure increases, the gas density increases which will increase the number of molecules that can be excited. It is observed that the density of the highest vibrational states, from $v = 10$ to $v = 14$, is lower for 20 Pa. This is consistent with the expectation that a higher gas pressure will increase the rate of collisional quenching.

Figure 5.13 (b) shows the distribution of vibrational energy at $R = 6$ cm and $Z = 5$ cm. The vibrational energy distribution at this location is notably different to that of figure 5.13 (a), for which the vibrational density distribution was plotted at a location of maximum density within the region of interest. At this location, for the vibrational states $v = 1$ to $v = 3$ the density of the vibrational states is highest for a gas pressure of 20 Pa. However, where $v > 3$ the vibrational state density is highest for a pressure of 13.3 Pa between $v = 3$ and $v = 9$. For $v > 9$, the highest density observed is for a pressure of 6.6 Pa. Overall, the vibrational energy distributions have similar characteristics to that observed in figure 5.13 (a), but at a gas pressure of 20 Pa, the distribution begins to approach a Boltzmann distribution. This shift from a superthermal distribution to a Boltzmann like distribution has been commented on in previous work using a CCP reactor, but in this work it appears much more pronounced[190]. In the previous work, the spatial difference in the distributions was negligible across the 1D reactor, and the superthermal plateau was visible for all pressures, which is distinct from the present ICP results in 2D, where the spatial location of the maximum density of some vibrational states is observed to change as shown previously in figures 5.10 and 5.11.

Linking back to the negative ion densities in figure 5.7, the higher negative ion density observed in figure 5.7 (a) compared to figure 5.7 (d) can be correlated to a wider spatial distribution of relatvely high ($v = 6$ to $v = 14$) vibrational states observed in figure 5.13 (b). It may also be reasonable to suggest that the relatively small change in maximum negative ion density observed between 6.6 Pa and 20 Pa is linked to the fact that the maximum vibrational density is similar for all pressures, as observed in figure 5.13 (a).

5.3 Impact of calculating the spatially dependent gas temperature

As described in section 1.3, the spatial distribution of the neutral gas temperature is influential to the distribution of vibrational energy within the plasma. This section explores the impact that the use of an isothermal gas temperature has on the distribution of neutral species within the plasma compared to the case where the gas temperature is calculated. This is of importance, as many PIC and Monte-Carlo models of hydrogen assume an isothermal neutral species gas temperature[60,111,134,190]. Figure 5.14 shows the vibrational density distribution in the region of interest highlighted in section 5.2 using an isothermal neutral gas temperature at 450 K for a pressure of 20 Pa and applied power of 300 W.

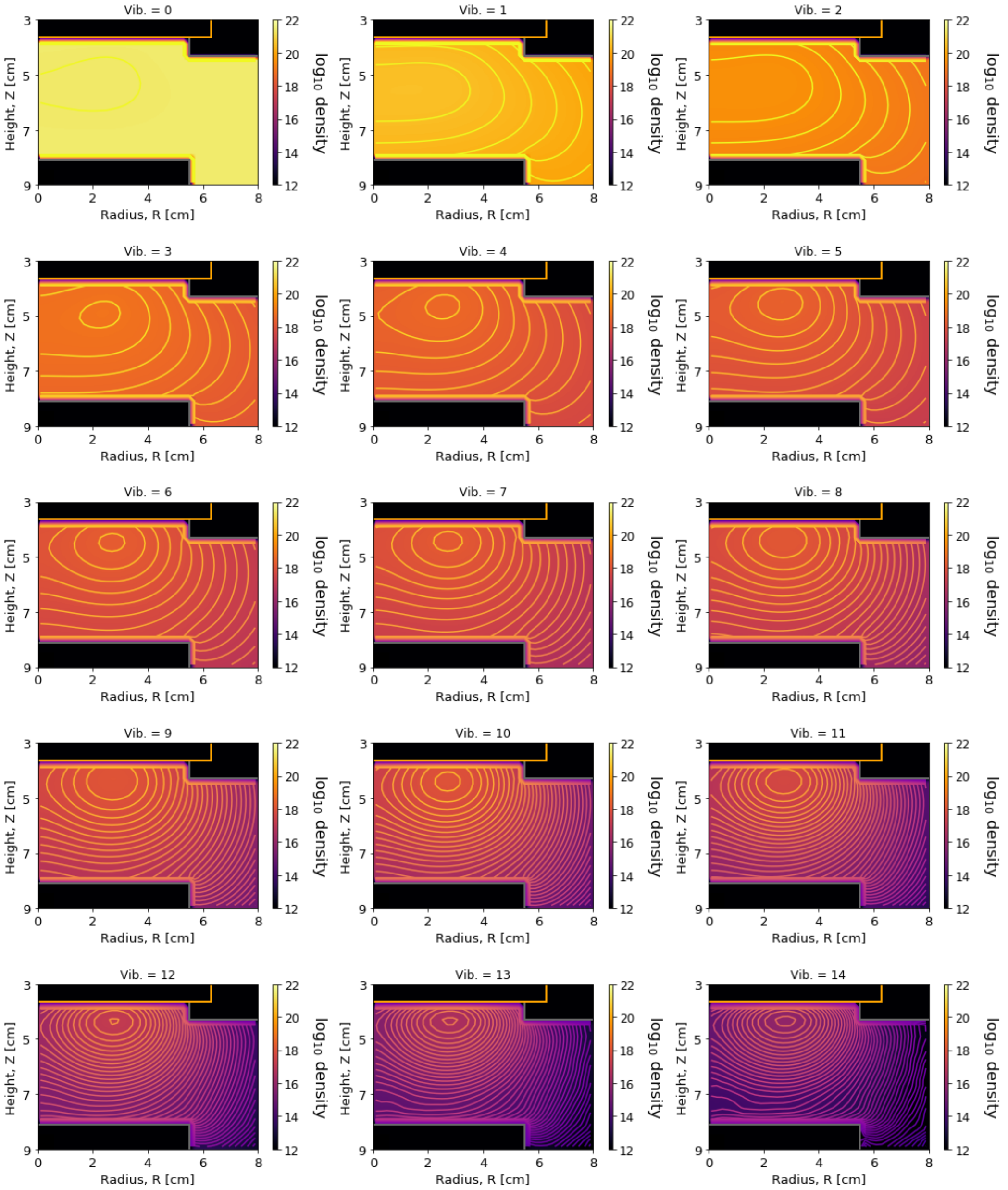

Figure 5.14: Vibrational density from $v = 0$ to $v = 14$ using an isothermal gas temperature at 450 K and 20 Pa with 300 W applied power.

The spatial distribution of vibrational states in figure 5.14 has some notable differences compared to the calculated case shown in figure 5.10.

The position of the maximum vibrational state density is observed at a position away from the surface of the dielectric window. This is unlike the case where the spatially resolved temperature of the neutral gas is determined self consistently as shown in figure 5.11. In this case, the maximum is observed to be close to the axis of the reactor and against the dielectric windows.

To study the quantitative impact of determining the spatially resolved gas temperature, the spatial and isothermal gas temperature cases are plotted in the radial plane of the maximum negative ion density, $Z = 5$ cm, for gas pressures of 20 Pa and 6.6 Pa as shown in figure 5.15 and figure 5.16, respectively.

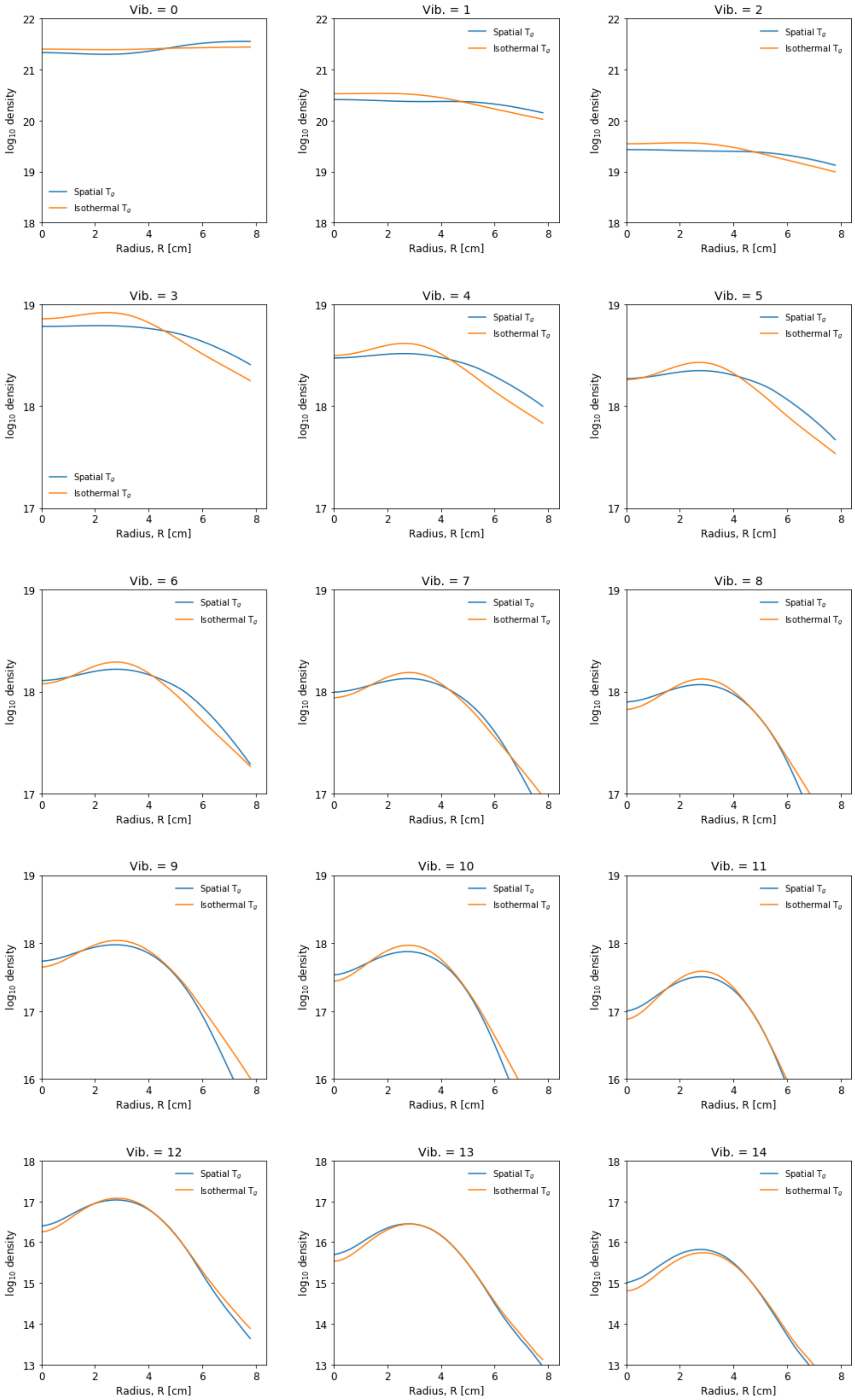

Figure 5.15: Radial distribution of vibrationally excited state densities for spatial and isothermal gas temperature gases at a pressure of 20 Pa. Data shown in the radial plane for $Z = 5$ cm with an applied power 300 W.

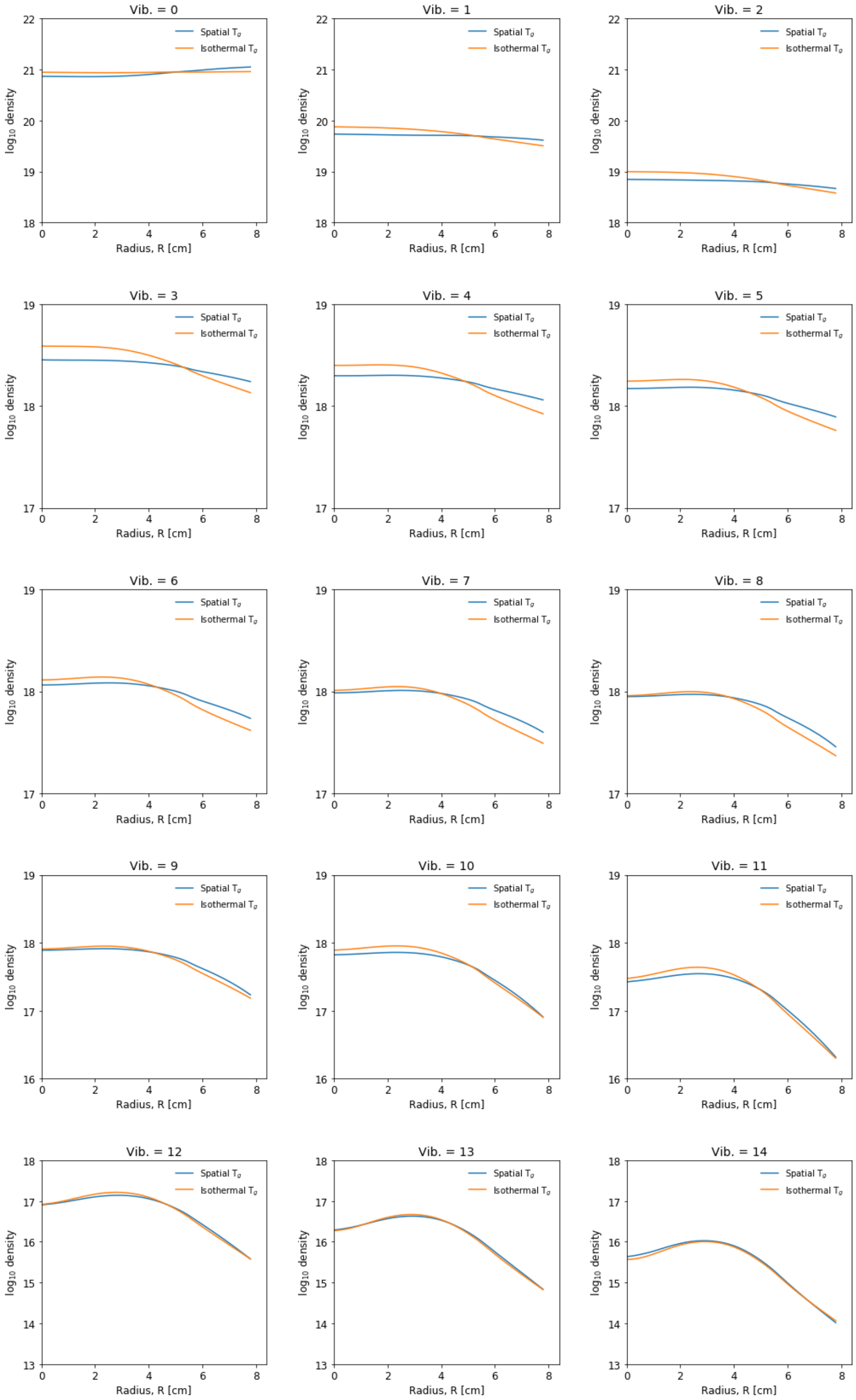

Figure 5.16: Radial distribution of vibrationally excited state densities for spatial and isothermal gas temperature gases at a pressure of 6.6 Pa. Data shown in the radial plane for $Z = 5$ cm with an applied power of 300 W.

Figure 5.15 highlights the difference in the distribution of vibrational states when using an isothermal gas temperature. The difference is more notable for the lower vibrational states between $v = 0$ and $v = 5$. For higher vibrational energies, the difference decreases. It is observed that for vibrational states higher than $v = 6$, the calculated gas temperature case approaches a distribution that is similar to the vibrational density distribution observed in the isothermal case. It is reasonable to suggest that at a pressure of 20 Pa, the diffusion of the higher vibrational states is lower.

The differences in the isothermal and spatially determined gas temperature case are broadly similar in figure 5.16 compared to figure 5.15. At lower energies, the vibrational densities are observed to be the most distinct between the isothermal and the calculated gas temperature case. As the vibrational energy increases the difference is reduced. For the case where $v = 12$ to $v = 14$, the difference in the vibrational density is observed to be small. This suggests that within the region of interest the use of an isothermal gas temperature influences the distribution of the intermediate vibrational states ($v = 3$ to $v = 6$) more than the lowest ($v = 0$ to $v = 2$) or the highest ($v = 4$ to $v = 14$).

5.3.1 Impact on the production of negative ions

As described in section 1.3, negative ions are produced in the bulk via dissociative attachment. This is underpinned by the production of vibrationally excited states. The distribution of vibrationally excited states shown in figures 5.15 and 5.16 can therefore be expected to have an impact on the production of negative ions. Figure 5.17 shows the negative ion density within the region of interest for the spatially resolved and isothermal gas temperature cases at pressures of 20 Pa and 6.6 Pa.

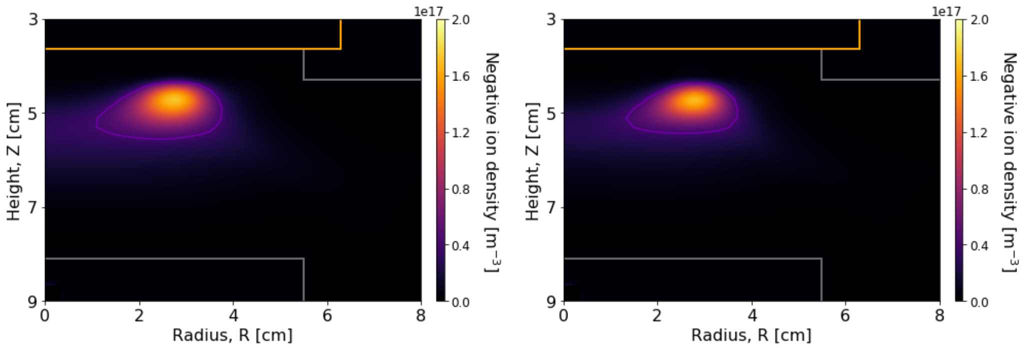
(a) 20 Pa, Spatial T_g (b) 20 Pa, Isothermal T_g

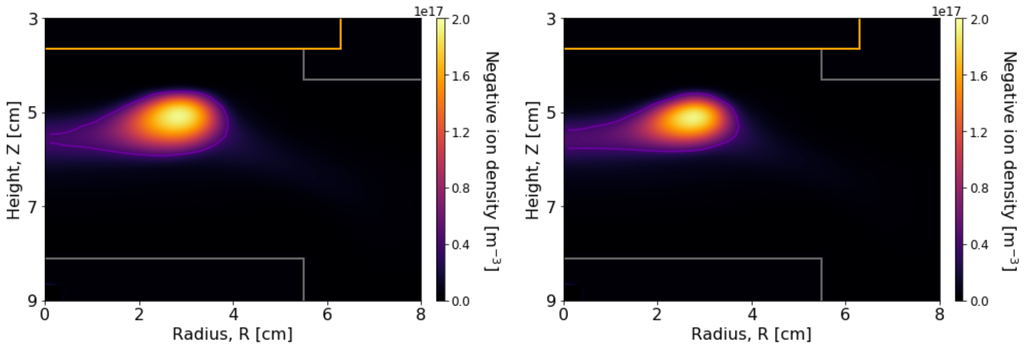
(c) 6.6 Pa, Spatial T_g (d) 6.6 Pa, Isothermal T_g

Figure 5.17: (a) and (c) show the negative ion density determined using a spatially determined gas temperature at 20 Pa and 6.6 Pa respectively. (b) and (d) show the negative ion density determined using a 450 K, isothermal gas temperature at 20 Pa and 6.6 Pa respectively. The single contour line highlights the location of negative ion densities of 0.6×10^{17} m^{-3}.

It is observed in figure 5.17 that the peak negative ion density is similarly positioned, at R = 2.8 cm and Z = 4.8 cm for a gas pressure of 20 Pa and for 6.6 Pa at R = 3 cm and Z = 5.2 cm, for an isothermal and calculated gas temperature case. Comparing figures 5.17 (a) and (b), the negative ion density is observed to be lower when using an isothermal gas temperature, with the peak density observed to be 1.85×10^{17} m^{-3} for the spatially resolved gas temperature and 1.83×10^{17} m^{-3} for the isothermal case.

In figure 5.17 (c) and (d), it is observed that the negative ion density is lower in the spatially resolved gas temperature case, compared to the isothermal case, with the peak density being 2.03×10^{17} m^{-3} and 2.01×10^{17} m^{-3} for each case respectively. The difference in maximum negative ion density is observed as being approximately 0.01%, which is likely to be smaller than overall uncertainty of the simulation, suggesting that any difference observed between the two gas temperature cases is too small to be resolved using these simulations.

It is observed that the distribution of negative ions within the plasma is different when using an isothermal gas temperature compared to a spatially resolved one. This is highlighted in figure 5.17 where the addition of a single contour line at the density 0.6×10^{17} m^{-3} shows that at both 20 Pa and 6.6 Pa, the density of negative ions is spatially larger in the Z axis by 0.15 cm when using a spatially resolved gas temperature compared to the isothermal gas temperature.

To observe correlations in the distribution of negative ions with respect to gas temperature, plasma potential, deposited power and the vibrational states v = 8, 10, 12, and 14; normalised radial distributions across the plasma on the Z = 5.8 cm axial plane are plotted in figure 5.18.

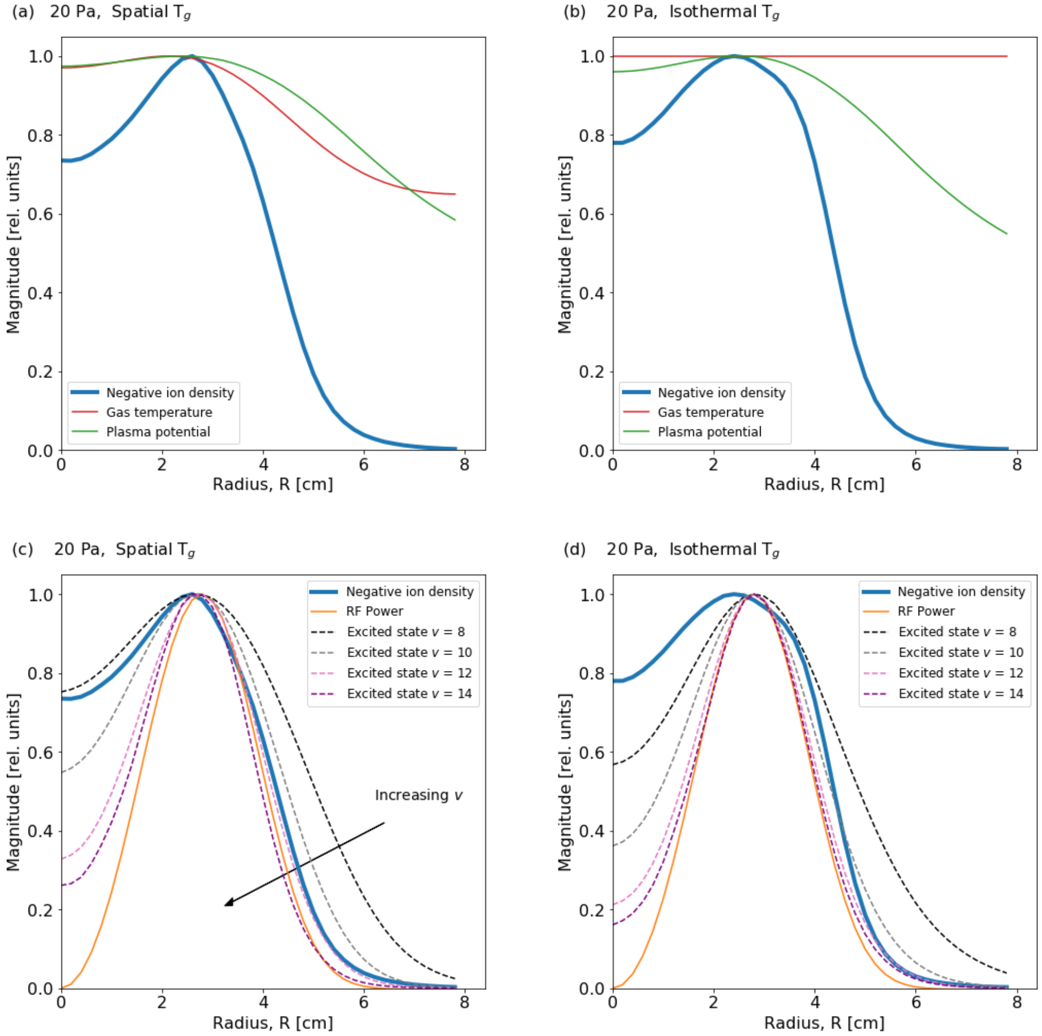

Figure 5.18: Radial distributions at Z = 5.8 cm for (a) and (c) spatially gas temperature (b) and (d) isothermal gas temperature at 20 Pa and an applied power of 300 W.

In figure 5.18 (a) the negative ion density is observed to be spatially distributed within the plasma with a peak in density at the location of maximum plasma potential. The gas temperature is also observed as being at a maximum where the negative ion density is at a maximum. In figure 5.18 (b) the negative ion density is observed to have a flatter peak compared to figure 5.18 (a).

The negative ion density is compared in figure 5.18 (c) with the power density and the vibrational states v = 8, 10, 12, and 14. It is observed that the vibrational densities correlate strongly with the location of power deposition and the location of maximum negative ion density. It is observed that as v is increased, the density of the vibrational states becomes increasingly confined to the location of maximum power deposition. This is also observed in figure 5.18 (d), where it is observed that the distribution of the higher level vibrational states is even more confined to the region of power deposition and appears to be consistent with the diffusion of vibrational states being higher when using a spatially resolved gas temperature.

Figure 5.18 demonstrates that multiple factors determine the distribution of negative ion density within the plasma. A strong correlation is observed between the plasma potential and the negative ion density, as well as between the power deposition and the vibrational states, with a weaker one observed between the lower vibrational states and the negative ion density at this axial plane.

5.4 Chapter summary

In this chapter, the results of the simulation introduced in chapter 4 are presented. Changes in the 2D distributions are described for a series of macroscopic plasma parameters. A particular feature of hydrogen plasma is the distribution of negative ions within the volume. In this work, the distribution of negative ions is simulated within the reactor, with a maximum density of negative ions observed at a pressure of 6.6 Pa. These negative ion distributions are influenced by the vibrational energy distributions. It is of interest to contrast the vibrational energy distributions for the case when the negative ion density is at a maximum and when it is at a minimum. No significant differences are observed in the distributions. However, the maximum density of the vibrational states within the reactor is observed to change as pressure is increased, with the higher energy vibrational states reducing in density as pressure is increased. One important aspect of an ICP reactor used in these simulations is that the gas is heated by the deposition of power into the reactor, resulting in the creation of spatial gas-temperature gradients. To investigate the impact of this, simulations with both spatially resolved and isothermal gas temperatures are compared. The vibrational distributions are observed to be distributed differently when using an isothermal gas temperature, with the highest densities observed within the bulk of the plasma compared to a spatially resolved gas temperature, where the highest densities were observed close to the dielectric window. For vibrational states above v = 9, the differences in the radial distribution of the vibrational states is similar when using an isothermal or a spatially resolved gas temperature. The differences in the spatial distribution of vibrational states appears to have only a small impact on the maximum observed negative ion density, but does have an impact on the distribution of negative ions in the plasma, where it is observed that the negative ion density distribution is larger when using a spatially resolved gas temperature compared to an isothermal gas temperature.

Chapter 6

Conclusions, future work and outlook

This thesis focuses on the physics of negative ion production in low-temperature plasmas. Using a combination of experimental and simulation techniques, the results address current research challenges in the context of surface production and volume production.

6.1 Conclusions

In the context of surface production of negative ions, a new technique is demonstrated for increasing the negative ion yield from diamond dielectrics via the incorporation of nitrogen dopant, dc and pulsed voltage biasing. The results demonstrate that the incorporation of nitrogen dopant can enhance the yield of negative ions from diamond. The results also show that the use of a pulsed bias can be used to mitigate the effect of high energy positive ion bombardment, and that the creation of a ratio of defects on diamond is of importance.

A new chemistry set is presented, built upon a previously established set used to study low-power 1D systems. This new chemistry set enables a detailed study of spatial gas heating and the impact this has on the vibrational kinetics and negative ion production in the bulk of high-power ICPs. The simulations are used to show the distribution of macroscopic plasma properties within an ICP reactor with respect to pressure. They are then used to demonstrate that the vibrational densities within the plasma are significantly influenced by the presence of temperature gradients and this has been observed to affect the distribution of negative ions within the bulk of the plasma.

6.2 Future work and outlook

Future studies into the surface production of negative ions from alternative materials is planned to investigate the results presented in this thesis in additional detail. The surface state of the samples undergoes a change during positive ion bombardment and it may be possible to resolve this change through in-situ surface measurements of the diamond during exposure to the plasma. Measurements of the sample surface before during and after exposure to the plasma within the reactor are also of interest. The observation that nitrogen doping of diamond can enhance negative ion yield opens up the possibility of using other dopants or a combination of dopants.

The choice of the HPEM for the simulation framework is in part based upon the built in features already available within the code to incorporate plasma-surface interactions. For example, surfaces are known to influence the vibrational energy distribution within hydrogen plasma through atomic recombination[210,220]. Surface recombination is also known to influence the gas temperature of the plasma[186]. These simulations can be used to gain insights into the role of surfaces and how this alters the distribution of vibrational states within the plasma.

The combination of the simulations with the work on nitrogen doped diamond is also of interest. Surface properties can be altered within the HPEM simulation framework to enable the production of negative ions from materials to be observed. This presents the prospect of further optimisation of the technological application of hydrogen plasma across a broad range of technological applications.

List of References

[1] P. Chabert and N. Braithwaite. *Physics of radio frequency plasmas*. Cambridge University Press, 2011. ISBN 978-0-521-76300-4.

[2] M. A. Lieberman and A. J. Lichtenberg. *Principles of plasma discharges and materials processing*. Wiley-interscience, 2nd edition, 2005. ISBN 0-471-72001-1.

[3] H. Conrads and M. Schmidt. Plasma generation and plasma sources. *Plasma Sources Science and Technology*, 9(September):441–454, 2000. ISSN 10986189. doi:10.1088/0963-0252/9/4/301.

[4] H. C. Lee. Review of inductively coupled plasmas: Nano-applications and bistable hysteresis physics. *Applied Physics Reviews*, 5(1), 2018. ISSN 19319401. doi:10.1063/1.5012001.

[5] U. R. Kortshagen, R. M. Sankaran, R. N. Pereira, S. L. Girshick, J. J. Wu, and E. S. Aydil. Nonthermal plasma synthesis of nanocrystals: Fundamental principles, materials, and applications. *Chemical Reviews*, 116(18):11061–11127, 2016. ISSN 15206890. doi:10.1021/acs.chemrev.6b00039.

[6] T. Okumura. Inductively coupled plasma sources and applications. *Physics Research International*, 2010(1), 2010. ISSN 1687689X. doi:10.1155/2010/164249.

[7] G. Franz. Low pressure plasmas and microstructuring technology. In *Low Pressure Plasmas and Microstructuring Technology*, pages 1–732. Springer, 2009. ISBN 9783540858485. doi:10.1007/978-3-540-85849-2.

[8] ITER. Iter website, 2017. URL `https://www.iter.org/`.

[9] A. M. Lietz and M.J. Kushner. Air plasma treatment of liquid covered tissue: Long timescale chemistry. *Journal of Physics D: Applied Physics*, 49(42), 2016. ISSN 13616463. doi:10.1088/0022-3727/49/42/425204.

[10] J. Ishikawa. Negative-ion source applications (invited). *Review of Scientific Instruments*, 79(2), 2008. ISSN 00346748. doi:10.1063/1.2814250.

[11] P Chabert and T E Sheridan. Kinetic model for a low-pressure discharge with negative ions. *Journal of Physics D: Applied Physics*, 1854, 2000.

[12] A. Meige, N. Plihon, G. J.M. Hagelaar, J. P. Boeuf, P. Chabert, and R. W. Boswell. Propagating double layers in electronegative plasmas. *Physics of Plasmas*, 14(5), 2007. ISSN 1070664X. doi:10.1063/1.2736946.

[13] N. Plihon and P. Chabert. Ion acoustic waves and double-layers in electronegative expanding plasmas. *Physics of Plasmas*, 18(8), 2011. ISSN 1070664X. doi:10.1063/1.3620405.

[14] N. D. Altieri, J. K-C. Chen, L. Minardi, and J. P. Chang. Review Article: Plasma–surface interactions at the atomic scale for patterning metals. *Journal of Vacuum Science and Technology A: Vacuum, Surfaces, and Films*, 35(5):05C203, 2017. ISSN 0734-2101. doi:10.1116/1.4993602.

[15] D. Rafalskyi and A. Aanesland. Brief review on plasma propulsion with neutralizer-free systems. *Plasma Sources Science and Technology*, 25(4):043001, 2016. ISSN 0963-0252. doi:10.1088/0963-0252/25/4/043001.

[16] T. Lafleur, D. Rafalskyi, and A. Aanesland. Alternate extraction and acceleration of positive and negative ions from a gridded plasma source. *Plasma Sources Science and Technology*, 24(1):015005, 2015. ISSN 0963-0252. doi:10.1088/0963-0252/24/1/015005.

[17] A. Aanesland, D. Rafalskyi, J. Bredin, P. Grondein, N. Oudini, P. Chabert, D. Levko, L. Garrigues, and G. Hagelaar. The PEGASES Gridded Ion – Ion Thruster Performance and Predictions. *IEEE Transactions of Plasma Science*, 43(1):321–326, 2015. doi:10.1109/TPS.2014.2369534.

[18] J. Peters. Negative ion sources for high energy accelerators (invited). *Review of Scientific Instruments*, 71(2):1069–1074, 2000. ISSN 0034-6748. doi:10.1063/1.1150388.

[19] M. Bacal and M. Wada. Negative hydrogen ion production mechanisms. *Applied Physics Reviews*, 2 (2):021305, 2015. ISSN 19319401. doi:10.1063/1.4921298.

[20] G. Colonna, G. Capitta, M. Capitelli, I. J. Wysong, and F. G. Kennedy. Model for ammonia solar thermal thruster. *Journal of Thermophysics and Heat Transfer*, 20(4):772–779, 2006. ISSN 15336808. doi:10.2514/1.18380.

[21] L. Blackhall and J. Khachan. A simple electric thruster based on ion charge exchange. *Journal of Physics D: Applied Physics*, 40(8):2491–2494, 2007. ISSN 00223727. doi:10.1088/0022-3727/40/8/011.

[22] R. Scrivens. Proton and Ion Sources for High Intensity Accelerators. *EPAC2004 Proceedings*, pages 103–107, 2004.

[23] A. Ueno, H. Oguri, K. Ikegami, Y. Namekawa, and K. Ohkoshi. Interesting experimental results in Japan Proton Accelerator Research Complex H$^-$ ion-source development (invited). *Review of Scientific Instruments*, 81(2):02A720, feb 2010. ISSN 0034-6748. doi:10.1063/1.3271243.

[24] D. P. Moehs, J. Peters, and J. Sherman. Negative hydrogen ion sources for accelerators. *IEEE Transactions on Plasma Science*, 33(6 I):1786–1798, 2005. ISSN 00933813. doi:10.1109/TPS.2005.860067.

[25] J. Lettry, D. Aguglia, P. Andersson, S. Bertolo, A. Butterworth, Y. Coutron, A. Dallocchio, E. Chaudet, J. Gil-Flores, R. Guida, J. Hansen, A. Hatayama, I. Koszar, E. Mahner, C. Mastrostefano, S. Mathot, S. Mattei, Midttun, P. Moyret, D. Nisbet, K. Nishida, M. O'Neil, M. Ohta, M. Paoluzzi, C. Pasquino, H. Pereira, J. Rochez, J. Sanchez Alvarez, J. Sanchez Arias, R. Scrivens, T. Shibata, D. Steyaert, N. Thaus, and T. Yamamoto. Status and operation of the Linac4 ion source prototypes. *Review of Scientific Instruments*, 85(2):02B122, 2014. ISSN 00346748. doi:10.1063/1.4848975.

[26] D. Faircloth and S. Lawrie. An overview of negative hydrogen ion sources for accelerators. *New Journal of Physics*, 20(2):025007, feb 2018. ISSN 1367-2630. doi:10.1088/1367-2630/aaa39e.

[27] R. F. Welton, A. V. Aleksandrov, V. G. Dudnikov, B. X. Han, Y. Kang, S. N. Murray, T. R. Pennisi, C. Piller, M. Santana, and M. P. Stockli. The status of the SNS external antenna ion source and spare RFQ test facility. *Review of Scientific Instruments*, 87(2):02B146, 2016. ISSN 10897623. doi:10.1063/1.4935236.

[28] A. J. Antolak, K. N. Leung, D. H. Morse, D. C. Donovan, J. M. Chames, J. A. Whaley, D. A. Buchenauer, A. X. Chen, P. A. Hausladen, and F. Liang. Negative ion-driven associated particle neutron generator. *Nuclear Instruments and Methods in Physics Research, Section A: Accelerators, Spectrometers, Detectors and Associated Equipment*, 806:30–35, 2016. ISSN 01689002. doi:10.1016/j.nima.2015.09.097.

[29] G. D. Alton. High-intensity, heavy negative ion sources based on the sputter principle (invited). *Review of Scientific Instruments*, 65(4):1141–1147, 1994. ISSN 00346748. doi:10.1063/1.1145040.

[30] R. Middleton. A survey of negative ion sources for tandem accelerators. *Nuclear Instruments and Methods*, 122(C):35–43, 1974. ISSN 0029554X. doi:10.1016/0029-554X(74)90469-8.

[31] L. Calcagnile, G. Quarta, and M. D'Elia. High-resolution accelerator-based mass spectrometry: Precision, accuracy and background. *Applied Radiation and Isotopes*, 62(4):623–629, 2005. ISSN 09698043. doi:10.1016/j.apradiso.2004.08.047.

[32] M. Yoneda, Y. Shibata, A. Tanaka, T. Uehiro, M. Morita, M. Uchida, T. Kobayashi, C. Kobayashi, R. Suzuki, K. Miyamoto, B. Hancock, C. Dibden, and J. Edmonds. AMS^{14}C measurement and preparative techniques at NIES-TERRA. *Nuclear Instruments and Methods in Physics Research, Section B: Beam Interactions with Materials and Atoms*, 223-224(SPEC. ISS.):116–123, 2004. ISSN 0168583X. doi:10.1016/j.nimb.2004.04.026.

[33] O. V. Vozniy and G. Y. Yeom. High-energy negative ion beam obtained from pulsed inductively coupled plasma for charge-free etching process. *Applied Physics Letters*, 94(23):2–5, 2009. ISSN 00036951. doi:10.1063/1.3152763.

[34] R. S. Hemsworth, D. Boilson, P. Blatchford, M. Dalla Palma, G. Chitarin, H P L de Esch, F. Geli, M. Dremel, J. Graceffa, D. Marcuzzi, G. Serianni, D. Shah, M. Singh, M. Urbani, and P. Zaccaria. Overview of the design of the ITER heating neutral beam injectors. *New Journal of Physics*, 19(2): 025005, feb 2017. ISSN 1367-2630. doi:10.1088/1367-2630/19/2/025005.

[35] R. S. Hemsworth, H. Decamps, J. Graceffa, B. Schunke, M. Tanaka, M. Dremel, A. Tanga, H. P. L. de Esch, F. Geli, J. Milnes, T. Inoue, D. Marcuzzi, P. Sonato, and P. Zaccaria. Status of the ITER heating neutral beam system. *Nuclear Fusion*, 49(4):45006, 2009. ISSN 0029-5515. doi:10.1088/0029-5515/49/4/045006.

[36] R. S. Hemsworth and T. Inoue. Positive and negative ion sources for magnetic fusion. *IEEE Transactions on Plasma Science*, 33(6):1799–1813, dec 2005. ISSN 00933813. doi:10.1109/TPS.2005.860090.

[37] U. Fantz, P. Franzen, and D. Wünderlich. Development of negative hydrogen ion sources for fusion: Experiments and modelling. *Chemical Physics*, 398:7–16, 2012. ISSN 0301-0104. doi:10.1016/j.chemphys.2011.05.006.

[38] T. Gans, V. Schulz-Von Der Gathen, and H. F. Döbele. Time dependence of rotational state populations of excited hydrogen molecules in an RF excited plasma reactor. *Plasma Sources Science and Technology*, 10(1):17–23, 2001. ISSN 09630252. doi:10.1088/0963-0252/10/1/303.

[39] T. Gans, Chun C. Lin, V. Schulz–von der Gathen, and H. F. Döbele. Phase-resolved emission spectroscopy of a hydrogen rf discharge for the determination of quenching coefficients. *Physical Review A - Atomic, Molecular, and Optical Physics*, 67(1):11, 2003. ISSN 10941622. doi:10.1103/PhysRevA.67.012707.

[40] P. Chabert, A. Rousseau, G. Gousset, and P. Leprince. On the influence of the gas velocity on dissociation degree and gas temperature in a flowing microwave hydrogen discharge. *Journal of Applied Physics*, 84(1):161–167, 1998. ISSN 00218979. doi:10.1063/1.368013.

[41] F. Gaboriau and J. P. Boeuf. Chemical kinetics of low pressure high density hydrogen plasmas: application to negative ion sources for ITER. *Plasma Sources Science and Technology*, 23(6):065032, 2014. ISSN 0963-0252. doi:10.1088/0963-0252/23/6/065032.

[42] D. O'Connell, R. Zorat, A. R. Ellingboe, and M. M. Turner. Comparison of measurements and particle-in-cell simulations of ion energy distribution functions in a capacitively coupled radio-frequency discharge. *Physics of Plasmas*, 14(10), 2007. ISSN 1070664X. doi:10.1063/1.2795634.

[43] R. Agnello, M. Barbisan, I. Furno, Ph Guittienne, A. A. Howling, R. Jacquier, R. Pasqualotto, G. Plyushchev, Y. Andrebe, S. Béchu, I. Morgal, and A. Simonin. Cavity ring-down spectroscopy to measure negative ion density in a helicon plasma source for fusion neutral beams. *Review of Scientific Instruments*, 89(10), 2018. ISSN 10897623. doi:10.1063/1.5044504.

[44] S. Dixon, C. Charles, J. Dedrick, T. Gans, D. O'Connell, and R. Boswell. Observations of a mode transition in a hydrogen hollow cathode discharge using phase resolved optical emission spectroscopy. *Applied Physics Letters*, 105(1), 2014. ISSN 00036951. doi:10.1063/1.4889916.

[45] C. Charles. Hydrogen ion beam generated by a current-free double layer in a helicon plasma. *Applied Physics Letters*, 84(3):332–334, 2004. ISSN 00036951. doi:10.1063/1.1643548.

[46] K. Oikawa, Y. Saito, S. Komizunai, K. Takahashi, and A. Ando. Radiofrequency hydrogen ion source with permanent magnets providing axial magnetic field. *Review of Scientific Instruments*, 85(2):12–15, 2014. ISSN 10897623. doi:10.1063/1.4849696.

[47] K. Takahashi, S. Takayama, A. Komuro, and A. Ando. Standing Helicon Wave Induced by a Rapidly Bent Magnetic Field in Plasmas. *Physical Review Letters*, 116(13):1–5, 2016. ISSN 10797114. doi:10.1103/PhysRevLett.116.135001.

[48] C. M. Samuell and C. S. Corr. Low-pressure hydrogen plasmas explored using a global model. *Plasma Sources Science and Technology*, 25(1), 2015. ISSN 13616595. doi:10.1088/0963-0252/25/1/015014.

[49] F. Prada. *Plasma Transport and Development of Plasma Kinetics in ARIS*. PhD thesis, Dublin City University, 2005.

[50] D O'Connell. *Investigations of high voltage plasma boundary sheaths in radio-frequency discharges operated with multiple frequencies*. PhD thesis, Dublin City University, 2004.

[51] R. K. Janev, D. Reiter, and U. Samm. Collision Processes in Low-Temperature Hydrogen Plasmas. *Sciences-New York*, page 190, 2003.

[52] A. A. Matveyev and V. P. Silakov. Kinetic processes in a highly-ionized non-equilibrium hydrogen plasma. *Plasma Sources Science and Technology*, 4(4):606–617, 1995. ISSN 09630252. doi:10.1088/0963-0252/4/4/012.

[53] C. Gorse and M. Capitelli. Progress in the non-equilibrium vibrational kinetics of hydrogen in magnetic multicusp H^- ion sources. *Chemical Physics*, 117:177–195, 1987.

[54] J. Loureiro and C. M. Ferreira. Electron and vibrational kinetics in the hydrogen positive column. *Journal of Physics D: Applied Physics*, 22(11):1680–1691, 1989. ISSN 13616463. doi:10.1088/0022-3727/22/11/017.

[55] V. A. Shakhatov and Y. A. Lebedev. Kinetics of populations of singlet and triplet states in non-equilibrium hydrogen plasma. *Journal of Physics D: Applied Physics*, 51(21), 2018. ISSN 13616463. doi:10.1088/1361-6463/aab8ca.

[56] P. Diomede, B. Bruneau, S. Longo, E. Johnson, and J. P. Booth. Capacitively coupled hydrogen plasmas sustained by tailored voltage waveforms: Vibrational kinetics and negative ions control. *Plasma Sources Science and Technology*, 26(7), 2017. ISSN 13616595. doi:10.1088/1361-6595/aa752c.

[57] T. E. Cravens. Vibrationally excited molecular hydrogen in the upper atmosphere of Jupiter. *Journal of Geophysical Research*, 92(A10):11083, 1987. ISSN 0148-0227. doi:10.1029/ja092ia10p11083.

[58] M. Capitelli, I. Armenise, D. Bruno, M. Cacciatore, R. Celiberto, G. Colonna, O. De Pascale, P. Diomede, F. Esposito, C. Gorse, K. Hassouni, A. Laricchiuta, S. Longo, D. Pagano, D. Pietanza, and M. Rutigliano. Non-equilibrium plasma kinetics: A state-to-state approach. *Plasma Sources Science and Technology*, 16(1), 2007. ISSN 09630252. doi:10.1088/0963-0252/16/1/S03.

[59] G. Colonna, G. D'Ammando, and L. D. Pietanza. The role of molecular vibration in nanosecond repetitively pulsed discharges and in DBDs in hydrogen plasmas. *Plasma Sources Science and Technology*, 25(5), 2016. ISSN 13616595. doi:10.1088/0963-0252/25/5/054001.

[60] P. Diomede, S. Longo, and M. Capitelli. Vibrational excitation and negative ion production in radio frequency parallel plate H_2 plasmas. *European Physical Journal D*, 33(2):243–251, 2005. ISSN 14346060. doi:10.1140/epjd/e2005-00037-5.

[61] A. Parashar, S. Kumar, J. Gope, C. M. S. Rauthan, P. N. Dixit, and S. A. Hashmi. Influence of argon dilution on growth and properties of hydrogenated nanocrystalline silicon films. *Solar Energy Materials and Solar Cells*, 94(5):892–899, 2010. ISSN 09270248. doi:10.1016/j.solmat.2010.01.014.

[62] I. Solomon, B. Drévillon, H. Shirai, and N. Layadi. Plasma deposition of microcrystalline silicon: the selective etching model. *Journal of Non-Crystalline Solids*, 164-166(PART 2):989–992, 1993. ISSN 00223093. doi:10.1016/0022-3093(93)91164-X.

[63] G. Cartry, D. Kogut, K. Achkasov, J. Layet, F. Thomas, A. Gicquel, J. Achard, O. Brinza, B. Thomas, H. Khemliche, P. Roncin, and A. Simonin. Alternative solutions to caesium in negative-ion sources: a study of negative-ion surface production on diamond in H_2/D_2 plasmas. *New Journal of Physics*, 19 (4):025010, 2017. doi:10.1088/1367-2630/aa5f1f.

[64] A. G. Borisov and V. A. Esaulov. Negative ion formation in the scattering of atoms and ions from dielectric surfaces. *Journal of Physics Condensed Matter*, 12(13):177–206, 2000. ISSN 09538984. doi:10.1088/0953-8984/12/13/201.

[65] R. Brako and D. M. Newns. Theory of electronic processes in atom scattering from surfaces. *Reports on Progress in Physics*, 52(6):655–697, 1989. ISSN 00344885. doi:10.1088/0034-4885/52/6/001.

[66] J. Los and J. J. C. Geerlings. Charge exchange in atom-surface collisions. *Physics Report*, 3(3):133–190, 1990. doi:10.1016/0370-1573(90)90104-A.

[67] M. Bacal. Physics aspects of negative ion sources. *Nuclear Fusion*, 46(6):S250–S259, 2006. ISSN 0029-5515. doi:10.1088/0029-5515/46/6/S05.

[68] D. Marinov, Z. el Otell, M. D. Bowden, and N. St. J. Braithwaite. Extraction and neutralization of positive and negative ions from a pulsed electronegative inductively coupled plasma. *Plasma Sources Science and Technology*, 2015. doi:doi:10.1088/0963-0252/24/6/065008.

[69] U. Fantz, D. Wünderlich, R. Riedl, B. Heinemann, and F. Bonomo. Achievement of the ITER NBI ion source parameters for hydrogen at the test facility ELISE and present Status for deuterium. *Fusion Engineering and Design*, 156(March):111609, 2020. ISSN 09203796. doi:10.1016/j.fusengdes.2020.111609.

[70] V. G. Dudnikov. The method for negative ion production - USSR patent, 1971.

[71] M. Bacal. Negative hydrogen ion production in fusion dedicated ion sources. *Chemical Physics*, 398(1):3–6, 2012. ISSN 03010104. doi:10.1016/j.chemphys.2011.04.002.

[72] U. Fantz, P. Franzen, W. Kraus, M. Berger, S. Christ-Koch, M. Fröschle, R. Gutser, B. Heinemann, C. Martens, P. McNeely, R. Riedl, E. Speth, and D. Wünderlich. Negative ion RF sources for ITER NBI: status of the development and recent achievements. *Plasma Physics and Controlled Fusion*, 49 (12B):B563, 2007. ISSN 0741-3335. doi:10.1088/0741-3335/49/12B/S53.

[73] Y. Takeiri. Negative ion source development for fusion application (invited). In *Review of Scientific Instruments*, volume 81, 2010. ISBN 1089-7623 (Electronic)0̊034-6748 (Linking). doi:10.1063/1.3274806.

[74] B. Heinemann, U. Fantz, W. Kraus, L. Schiesko, C. Wimmer, D. Wünderlich, F. Bonomo, M. Fröschle, R. Nocentini, and R. Riedl. Towards large and powerful radio frequency driven negative ion sources for fusion. *New Journal of Physics*, 19(1), 2017. ISSN 13672630. doi:10.1088/1367-2630/aa520c.

[75] R. S. Hemsworth and D. Boilson. Research, Design, and Development Needed to Realise a Neutral Beam Injection System for a Fusion Reactor. *IntechOpen*, i(Fusion Energy):13, 2019. doi:http://dx.doi.org/10.5772/intechopen.88724.

[76] A. Ahmad, C. Pardanaud, M. Carrère, J. Layet, A. Gicquel, P. Kumar, D. Eon, C. Jaoul, R. Engeln, and G. Cartry. Negative-ion production on carbon materials in hydrogen plasma: influence of the carbon hybridization state and the hydrogen content on H^- yield. *Journal of Physics D: Applied Physics*, 47 (8):085201, 2014. ISSN 0022-3727. doi:10.1088/0022-3727/47/8/085201.

[77] L. Schiesko, M. Carrère, J. M. Layet, and G. Cartry. Negative ion surface production through sputtering in hydrogen plasma. *Applied Physics Letters*, 95(19):191502, 2009. ISSN 00036951. doi:10.1063/1.3258352.

[78] L. Schiesko, M. Carrere, J. Layet, and G. Cartry. A comparative study of H^- and D^- production on graphite surfaces in H_2 and D_2 plasmas. *Plasma Sources Sci. Technol.*, 19(4):45016, 2010. ISSN 0963-0252. doi:10.1088/1367-2630/aa5f1f.

[79] M. Sasao, R. Moussaoui, D. Kogut, J. Ellis, G. Cartry, M. Wada, K. Tsumori, and H. Hosono. Negative-hydrogen-ion production from a nanoporous $12CaO{\cdot}7Al_2O_3$ electride surface. *Applied Physics Express*, 11:066201, 2018. doi:10.7567/APEX.11.066201.

[80] U. Kurutz, R. Friedl, and U. Fantz. Investigations on Cs-free alternatives for negative ion formation in a low pressure hydrogen discharge at ion source relevant parameters. *Plasma Physics and Controlled Fusion*, 59(7):075008, 2017. ISSN 0741-3335. doi:10.1088/1361-6587/aa7120.

[81] P. Kumar, A. Ahmad, C. Pardanaud, M. Carrère, J. M. Layet, G. Cartry, F. Silva, A. Gicquel, and R. Engeln. Enhanced negative ion yields on diamond surfaces at elevated temperatures. *Journal of Physics D: Applied Physics*, 44(37):372002, sep 2011. ISSN 0022-3727. doi:10.1088/0022-3727/44/37/372002.

[82] D. Kogut, R. Moussaoui, Ning Ning, J B Faure, J M Layet, T. Farley, J. Achard, A. Gicquel, and G. Cartry. Impact of positive ion energy on carbon-surface production of negative ions in deuterium plasmas. *Journal of Physics D: Applied Physics*, 52(43):435201, oct 2019. ISSN 0022-3727. doi:10.1088/1361-6463/ab34f1.

[83] K. Achkasov, R. Moussaoui, D. Kogut, E. Garabedian, J. M. Layet, A. Simonin, A. Gicquel, J. Achard, A. Boussadi, and G. Cartry. Pulsed DC bias for the study of negative-ion production on surfaces of insulating materials in low pressure hydrogen plasmas. *Journal of Applied Physics*, 125(3):033303, 2019. ISSN 10897550. doi:10.1063/1.5054607.

[84] D. Kogut, K. Achkasov, J. P. Dubois, R. Moussaoui, J. B. Faure, J. M. Layet, A. Simonin, and G. Cartry. Reconstruction of energy and angle distribution function of surface-emitted negative ions in hydrogen plasmas using mass spectrometry. *Plasma Sources Science and Technology*, 26(4):045006 (14pp), 2017. ISSN 13616595. doi:10.1088/1361-6595/aa5d7b.

[85] J. Dubois, K. Achkasov, D. Kogut, A. Ahmad, J. Layet, A. Simonin, and G. Cartry. Negative-ion surface production in hydrogen plasmas: Determination of the negative-ion energy and angle distribution function using mass spectrometry. *Journal of Applied Physics*, 119(19):193301, 2016. ISSN 10897550. doi:10.1063/1.4948949.

[86] G. J. Smith, J. Ellis, R. Moussaoui, C. Pardanaud, C. Martin, J. Achard, R. Issaoui, T. Gans, J. P. Dedrick, and G. Cartry. Enhancing surface production of negative ions using nitrogen doped diamond in a deuterium plasma. *Journal of Physics D: Applied Physics*, 53(46):465204, nov 2020. ISSN 0022-3727. doi:10.1088/1361-6463/aba6b6.

[87] A. Heiler, K. Waetzig, M. Tajmar, R. Friedl, R. Nocentini, and U. Fantz. Work function performance of a C12A7 electride surface exposed to low pressure low temperature hydrogen plasmas. *Journal of Vacuum Science and Technology A*, 39(1):013002, jan 2021. ISSN 0734-2101. doi:10.1116/6.0000749.

[88] H. Hosono and M. Kitano. Advances in Materials and Applications of Inorganic Electrides. *Chemical Reviews*, 2021. ISSN 15206890. doi:10.1021/acs.chemrev.0c01071.

[89] A. G. Borisov and V. A. Esaulov. Negative ion formation in the scattering of atoms and ions from dielectric surfaces. *Journal of Physics Condensed Matter*, 12(13):19–22, 2000. ISSN 09538984. doi:10.1088/0953-8984/12/13/201.

[90] A. G. Borisov, V. Sidis, and H. Winter. Diabatic Energy Level Confluence: The Mechanism of Negative Ion Conversion of Neutral Atoms in Grazing Scattering from Insulator Surfaces. *Physical Review Letters*, 77(9):1893–1896, aug 1996. ISSN 0031-9007. doi:10.1103/PhysRevLett.77.1893.

[91] J. J. Gracio, Q. H. Fan, and J. C. Madaleno. Diamond growth by chemical vapour deposition. *Journal of Physics D: Applied Physics*, 43(37), 2010. ISSN 00223727. doi:10.1088/0022-3727/43/37/374017.

[92] M. Schwander and K. Partes. A review of diamond synthesis by CVD processes. *Diamond and Related Materials*, 20(9):1287–1301, 2011. ISSN 09259635. doi:10.1016/j.diamond.2011.08.005.

[93] J. E. Shigley and S. Eaton-Magaña. Observations on CVD-grown synthetic diamonds: a review. *Gems and Gemoloy*, 52(3), 2016.

[94] L. Diederich, O. M. Küttel, P. Aebi, and L. Schlapbach. Electron affinity and work function of differently oriented and doped diamond surfaces determined by photoelectron spectroscopy. *Surface Science*, 418 (1):219–239, 1998. ISSN 00396028. doi:10.1016/S0039-6028(98)00718-3.

[95] Y. Liu, Y. Zhang, K. Cheng, X. Quan, X. Fan, Y. Su, S. Chen, H. Zhao, Y. Zhang, H. Yu, and M. R. Hoffmann. Selective Electrochemical Reduction of Carbon Dioxide to Ethanol on a Boron- and Nitrogen-Co-doped Nanodiamond. *Angewandte Chemie - International Edition*, 56(49):15607–15611, 2017. ISSN 15213773. doi:10.1002/anie.201706311.

[96] T. Tachibana, Y. Ando, A. Watanabe, Y. Nishibayashi, K. Kobashi, T. Hirao, and K. Oura. Diamond films grown by a 60-kW microwave plasma chemical vapor deposition system. *Diamond and Related Materials*, 10(9-10):1569–1572, 2001. ISSN 09259635. doi:Doi 10.1016/S0925-9635(01)00410-1.

[97] A. Scholze, W. Schmidt, and F. Bechstedt. Structure of the diamond (111) surface: Single-dangling-bond versus triple-dangling-bond face. *Physical Review B - Condensed Matter and Materials Physics*, 53(20):13725–13733, 1996. ISSN 1550235X. doi:10.1103/PhysRevB.53.13725.

[98] V. Baranauskas, B. B. Li, A. Peterlevitz, M. C. Tosin, and S. F. Durrant. Nitrogen-doped diamond films. *Journal of Applied Physics*, 85(10):7455–7458, 1999. ISSN 00218979. doi:10.1063/1.369378.

[99] Z. Yiming, F. Larsson, and K. Larsson. Effect of CVD diamond growth by doping with nitrogen. *Theoretical Chemistry Accounts*, 133(2):1–12, 2014. ISSN 1432881X. doi:10.1007/s00214-013-1432-y.

[100] L. Diederich, O. M. Kuttel, P. Aebi, and L. Schlapbach. Electron emission and NEA from differently terminated, doped and oriented diamond surfaces. *Diamond and Related Materials*, 8(2):743–747, 1999. ISSN 09259635. doi:10.1016/S0925-9635(98)00339-2.

[101] P. Abbott, E. D. Sosa, and D. E. Golden. Effect of average grain size on the work function of diamond films. *Applied Physics Letters*, 79(17):2835–2837, 2001. ISSN 00036951. doi:10.1063/1.1412825.

[102] D. C. Faircloth. Negative Ion Sources: Magnetron and Penning. *CERN Yellow Report CERN-2013-007, pp.285-310*, 2014. doi:10.5170/CERN-2013-007.285.

[103] E. Stoffels, W. W. Stoffels, and G. M.W. Kroesen. Plasma chemistry and surface processes of negative ions. *Plasma Sources Science and Technology*, 10(2):311–317, 2001. ISSN 09630252. doi:10.1088/0963-0252/10/2/321.

[104] M. Capitelli, M. Cacciatore, R. Celiberto, O. De Pascale, P. Diomede, F. Esposito, A. Gicquel, C. Gorse, K. Hassouni, A. Laricchiuta, S. Longo, D. Pagano, and M. Rutigliano. Vibrational kinetics, electron dynamics and elementary processes in H_2 and D_2 plasmas for negative ion production: Modelling aspects. *Nuclear Fusion*, 46(6), 2006. ISSN 00295515. doi:10.1088/0029-5515/46/6/S06.

[105] E. E. Nikitin and J. Troe. 70 Years of Landau-Teller theory for collisional energy transfer. Semiclassical three-dimensional generalizations of the classical collinear model. *Physical Chemistry Chemical Physics*, 10(11):1483–1501, 2008. ISSN 14639076. doi:10.1039/b715095d.

[106] M. Capitelli, C. M. Ferreira, B. F. Gordiets, and I. V. Osipov. *Plasma kinetics in atmospheric gases*. Springer, 2010. ISBN 978-3-642-08683-0.

[107] H. Abada, P. Chabert, J. P. Booth, J. Robiche, and G. Cartry. Gas temperature gradients in a CF_4 inductive discharge. *Journal of Applied Physics*, 92(8):4223–4230, 2002. ISSN 00218979. doi:10.1063/1.1505683.

[108] B. Gordiets, C. M. Ferreira, M. J. Pinheiro, and A. Ricard. Self-consistent kinetic model of low-pressure N_2-H_2 flowing discharges: II. Surface processes and densities of N, H, NH_3 species. *Plasma Sources Science and Technology*, 7(3):379–388, 1998. ISSN 09630252. doi:10.1088/0963-0252/7/3/016.

[109] M. Capitelli, R. Celiberto, F. Esposito, A. Laricchiuta, K. Hassouni, and S. Longo. Elementary processes and kinetics of H_2 plasmas for different technological applications. *Plasma Sources Science and Technology*, 11(3 A), 2002. ISSN 09630252. doi:10.1088/0963-0252/11/3A/302.

[110] T. Mosbach. Population dynamics of molecular hydrogen and formation of negative hydrogen ions in a magnetically confined low temperature plasma. *Plasma Sources Science and Technology*, 14(3):610–622, 2005. ISSN 09630252. doi:10.1088/0963-0252/14/3/026.

[111] W. Yang, H. Li, F. Gao, and Y. N. Wang. Hybrid simulations of solenoidal radio-frequency inductively coupled hydrogen discharges at low pressures. *Physics of Plasmas*, 23(12), 2016. ISSN 10897674. doi:10.1063/1.4971807.

[112] W. Yang, S. N. Averkin, A. V. Khrabrov, I. D. Kaganovich, Y. N. Wang, S. Aleiferis, and P. Svarnas. Benchmarking and validation of global model code for negative hydrogen ion sources. *Physics of Plasmas*, 25(11), 2018. ISSN 10897674. doi:10.1063/1.5050029.

[113] F. Gao, Y. R. Zhang, H. Li, Y. Liu, and Y. N. Wang. Spatial distributions of plasma parameters in inductively coupled hydrogen discharges with an expansion region. *Physics of Plasmas*, 24(7), 2017. ISSN 10897674. doi:10.1063/1.4989704.

[114] J. P. Boeuf, G. J.M. Hagelaar, P. Sarrailh, G. Fubiani, and N. Kohen. Model of an inductively coupled negative ion source: II. Application to an ITER type source. *Plasma Sources Science and Technology*, 20(1), 2011. ISSN 09630252. doi:10.1088/0963-0252/20/1/015002.

[115] G. J. M. Hagelaar, G. Fubiani, and J. P. Boeuf. Model of an inductively coupled negative ion source: I. General model description. *Plasma Sources Science and Technology*, 20(1):015001, feb 2011. ISSN 0963-0252. doi:10.1088/0963-0252/20/1/015001.

[116] G. Fubiani, L. Garrigues, G. Hagelaar, N. Kohen, and J. P. Boeuf. Modeling of plasma transport and negative ion extraction in a magnetized radio-frequency plasma source. *New Journal of Physics*, 19, 2017. ISSN 13672630. doi:10.1088/1367-2630/19/1/015002.

[117] F. Taccogna and P. Minelli. PIC modeling of negative ion sources for fusion. *New Journal of Physics*, 19(1), 2017. ISSN 13672630. doi:10.1088/1367-2630/aa5305.

[118] S. Lishev, L. Schiesko, D. Wünderlich, C. Wimmer, and U. Fantz. Fluid-model analysis on discharge structuring in the RF-driven prototype ion-source for ITER NBI. *Plasma Sources Science and Technology*, 27(12), 2018. ISSN 13616595. doi:10.1088/1361-6595/aaf536.

[119] A. Hatayama, S. Nishioka, K. Nishida, S. Mattei, J. Lettry, K. Miyamoto, T. Shibata, M. Onai, S. Abe, S. Fujita, S. Yamada, and A. Fukano. Present status of numerical modeling of hydrogen negative ion source plasmas and its comparison with experiments: Japanese activities and their collaboration with experimental groups. *New Journal of Physics*, 20(6), 2018. ISSN 13672630. doi:10.1088/1367-2630/aac0c6.

[120] S. Mattei, K. Nishida, M. Onai, J. Lettry, M. Q. Tran, and A. Hatayama. A fully-implicit Particle-In-Cell Monte Carlo Collision code for the simulation of inductively coupled plasmas. *Journal of Computational Physics*, 350:891–906, 2017. ISSN 10902716. doi:10.1016/j.jcp.2017.09.015.

[121] K. Nishida, S. Mattei, S. Mochizuki, J. Lettry, and A. Hatayama. Kinetic modeling of E-to-H mode transition in inductively coupled hydrogen plasmas. *Journal of Applied Physics*, 119(23), 2016. ISSN 10897550. doi:10.1063/1.4953647.

[122] Z. Donkó, J. Schulze, S. Müller, and U. Czarnetzki. Kinetic simulation of a nanosecond-pulsed hydrogen microdischarge. *Applied Physics Letters*, 98(25):96–99, 2011. ISSN 00036951. doi:10.1063/1.3601486.

[123] Y. Zhang, X. Xu, A. Bogaerts, and Y. Wang. Fluid simulation of the phase-shift effect in hydrogen capacitively coupled plasmas: II. Radial uniformity of the plasma characteristics. *Journal of Physics D: Applied Physics*, 45(1):015203, 2012. ISSN 0022-3727. doi:10.1088/0022-3727/45/1/015203.

[124] S. Longo and I. D. Boyd. Nonequilibrium dissociation of hydrogen in a parallel-plate radio frequency discharge. *Chemical Physics*, 238(3):445–453, 1998. doi:10.1016/S0301-0104(98)00357-7.

[125] S. Longo and A. Milella. A one-dimensional, self-consistent model of charged particle transport and vibrational kinetics in weakly ionized hydrogen. *Chemical Physics*, 274(2-3):219–229, 2001. ISSN 03010104. doi:10.1016/S0301-0104(01)00511-0.

[126] P. Diomede. *Non equilibrium hydrogen plasmas: chemical kinetics and Monte Carlo models of charged particle transport*. PhD thesis, Universita' degli studi di Bari, 2004.

[127] P. Diomede, S. Longo, D. J. Economou, and M. Capitelli. Hybrid simulation of a dc-enhanced radio-frequency capacitive discharge in hydrogen. *Journal of Physics D: Applied Physics*, 45(17), 2012. ISSN 00223727. doi:10.1088/0022-3727/45/17/175204.

[128] P. Diomede, A. Michau, M. Redolfi, W. Morscheidt, K. Hassouni, S. Longo, and M. Capitelli. Fluid and kinetic models of the low temperature H_2 plasma produced by a radio-frequency reactor. *Physics of Plasmas*, 15(10), 2008. ISSN 1070664X. doi:10.1063/1.3006152.

[129] P. Diomede and S. Longo. Velocity distribution of H^- ions in low temperature hydrogen plasma. *IEEE Transactions on Plasma Science*, 36(4 PART 2):1600–1606, 2008. ISSN 00933813. doi:10.1109/TPS.2008.927273.

[130] S. Longo, P. Diomede, and M. Capitelli. Multispecies particle simulation of the hydrogen plasma sheath region. *Contributions to Plasma Physics*, 46(7-9):763–768, 2006. ISSN 08631042. doi:10.1002/ctpp.200610075.

[131] S. Longo and P. Diomede. Modeling of capacitively coupled RF plasmas in H_2. *Plasma Processes and Polymers*, 6(5):370–379, 2009. ISSN 16128850. doi:10.1002/ppap.200800219.

[132] B. Bruneau, P. Diomede, D. J. Economou, S. Longo, T. Gans, D. O'Connell, A. Greb, E. Johnson, and J. P. Booth. Capacitively coupled hydrogen plasmas sustained by tailored voltage waveforms: Excitation dynamics and ion flux asymmetry. *Plasma Sources Science and Technology*, 25(4), 2016. ISSN 13616595. doi:10.1088/0963-0252/25/4/045019.

[133] P. Diomede, B. Bruneau, S. Longo, E. Johnson, and J-P. Booth. Capacitively coupled hydrogen plasmas sustained by tailored voltage waveforms: vibrational kinetics and negative ions control. *Plasma Sources Science and Technology*, 26(7):075007, jun 2017. ISSN 1361-6595. doi:10.1088/1361-6595/aa752c.

[134] Ts. Paunska, A. Shivarova, Kh. Tarnev, and Ts. Tsankov. Negative hydrogen ion maintenance in small radius discharges: Two-dimensional modeling. *Physics of Plasmas*, 18(2), 2011. ISSN 1070664X. doi:10.1063/1.3553463.

[135] P. Diomede, S. Longo, D. J. Economou, and M. Capitelli. Hybrid simulation of a dc-enhanced radio-frequency capacitive discharge in hydrogen. *Journal of Physics D: Applied Physics*, 45(17):175204, 2012. ISSN 0022-3727. doi:10.1088/0022-3727/45/17/175204.

[136] C. D. Pintassilgo, V. Guerra, O. Guaitella, and A. Rousseau. Study of gas heating mechanisms in millisecond pulsed discharges and afterglows in air at low pressures. *Plasma Sources Science and Technology*, 23(2), 2014. ISSN 13616595. doi:10.1088/0963-0252/23/2/025006.

[137] C. D. Pintassilgo and V. Guerra. On the different regimes of gas heating in air plasmas. *Plasma Sources Science and Technology*, 24(5), 2015. ISSN 13616595. doi:10.1088/0963-0252/24/5/055009.

[138] A. Ahmad, J. Dubois, T. Pasquet, M. Carrère, J. M. Layet, J. B. Faure, G. Cartry, P. Kumar, T. Minéa, S. Mochalskyy, A. Simonin, and A. Pasquet. Negative-ion surface production in hydrogen plasmas: modeling of negative-ion energy distribution functions and comparison with experiments. *Plasma Sources Science and Technology*, 22(2):025006, 2013. ISSN 0963-0252. doi:10.1088/0963-0252/22/2/025006.

[139] L. Schiesko, M. Carrère, G. Cartry, and J. M. Layet. H^- production on a graphite surface in a hydrogen plasma. *Plasma Sources Science and Technology*, 17(3):35023, 2008. ISSN 0963-0252. doi:10.1088/0963-0252/17/3/035023.

[140] A. V. Phelps. Cross Sections and Swarm Coefficients for H^+, H_2^+, H_3^+, H, H_2, and H^- in H_2 for Energies from 0.1eV to 10keV. *Journal of Physical and Chemical Reference Data*, 19(3):653–675, may 1990. ISSN 0047-2689. doi:10.1063/1.555858.

[141] K. Achkavsov. *Study of negative ion surface production in cesium-free*. Thesis, Universite d'Aix Marseille, 2015.

[142] T. Babkina, T. Gans, and U. Czarnetzki. Energy analysis of hyperthermal hydrogen atoms generated through surface neutralisation of ions. *Europhysics Letters*, 72(2):235–241, 2005. ISSN 02955075. doi:10.1209/epl/i2005-10220-2.

[143] F. Silva, K. Hassouni, X. Bonnin, and A. Gicquel. Microwave engineering of plasma-assisted CVD reactors for diamond deposition. *Journal of Physics Condensed Matter*, 21(36), 2009. ISSN 09538984. doi:10.1088/0953-8984/21/36/364202.

[144] F. Silva and A. Gicquel. Structural characteristics of CVD diamond films versus nitrogen impurities coupled to other deposition parameters. *Proceedings of the fifth-International Symposium on Diamond Materials, Journal of Electrochemical Society*, 97-32:99–125, 1998.

[145] J. Mossbrucker and T. A. Grotjohn. Determination of local crystal orientation of diamond using polarized Raman spectra. *Diamond and Related Materials*, 5(11):1333–1343, 1996. ISSN 09259635. doi:10.1016/0925-9635(96)00547-X.

[146] S. Prawer and R. J. Nemanich. Raman spectroscopy of diamond and doped diamond. *Phil. Trans. R. Soc. Lond. A*, 362(1824):2537–2565, 2004. doi:10.1098/rsta.2004.1451.

[147] R. Kumar, S. J. Yoon, K. G. Lee, P. Pal, R. P. Pant, C. K. Suman, S. R. Dhakate, R. Kumar, D. K. Avasthi, and D. K. Singh. Purification method dependent fluorescence from nitrogen-vacancy (NV) centers of nano-diamonds. *RSC Advances*, 6(52):47164–47173, 2016. ISSN 20462069. doi:10.1039/c6ra01510g.

[148] E. Smith and G. Dent. *Modern Raman Spectroscopy – A Practical Approach*. John Wiley and Sons, Ltd, 2005. ISBN 0-471-49794-0.

[149] J. Achard, F. Silva, O. Brinza, A. Tallaire, and A. Gicquel. Coupled effect of nitrogen addition and surface temperature on the morphology and the kinetics of thick CVD diamond single crystals. *Diamond and Related Materials*, 16(4-7):685–689, apr 2007. ISSN 09259635. doi:10.1016/j.diamond.2006.09.012.

[150] A. Tallaire, A. T. Collins, D. Charles, J. Achard, R. Sussmann, A. Gicquel, M. E. Newton, A. M. Edmonds, and R. J. Cruddace. Characterisation of high-quality thick single-crystal diamond grown by CVD with a low nitrogen addition. *Diamond and Related Materials*, 15(10):1700–1707, 2006. ISSN 09259635. doi:10.1016/j.diamond.2006.02.005.

[151] P. K. Chu and L. Li. Characterization of amorphous and nanocrystalline carbon films. *Materials Chemistry and Physics*, 96(2-3):253–277, 2006. ISSN 02540584. doi:10.1016/j.matchemphys.2005.07.048.

[152] A. Merlen, J. Buijnsters, and C. Pardanaud. A guide to and review of the use of multiwavelength Raman spectroscopy for characterizing defective aromatic carbon solids: From graphene to amorphous carbons. *Coatings*, 7:153, 2017. ISSN 20796412. doi:10.3390/coatings7100153.

[153] R. Samlenski, J. Schmälzlin, R. Brenn, C. Wild, W. Müller-Sebert, and P. Koidl. Characterization of homoepitaxial diamond films by nuclear methods. *Diamond and Related Materials*, 4(4):503–507, 1995. ISSN 09259635. doi:10.1016/0925-9635(94)05238-7.

[154] S. Satoh, H. Sumiya, K. Tsuji, and S. Yazu. Difference in Nitrogen Concentration and Aggregation among (111) and (100) Growth Sectors of Large Synthetic Diamonds. In *Science and Technology of New Diamond*, pages 351–355. KTK Scientific Publishers, Tokyo, 1990. ISBN 4-87677-104-9.

[155] Y. Zhao, C. Li, J. Liu, K. An, X. Yan, L. Hei, L. Chen, J. Wei, and F. Lu. The interface and mechanical properties of a CVD single crystal diamond produced by multilayered nitrogen doping epitaxial growth. *Materials*, 12(15):2492, 2019. ISSN 19961944. doi:10.3390/ma12152492.

[156] S. Al-Riyami, S. Ohmagari, and T. Yoshitake. Nitrogen-doped ultrananocrystalline diamond/hydrogenated amorphous carbon composite films prepared by pulsed laser deposition. *Applied Physics Express*, 3(11):5–8, 2010. ISSN 18820778. doi:10.1143/APEX.3.115102.

[157] S. Bhattacharyya, O. Auciello, J. Birrell, J. A. Carlisle, L. A. Curtiss, A. N. Goyette, D. M. Gruen, A. R. Krauss, J. Schlueter, A. Sumant, and P. Zapol. Synthesis and characterization of highly-conducting nitrogen-doped ultrananocrystalline diamond films. *Applied Physics Letters*, 79(10):1441–1443, 2001. ISSN 00036951. doi:10.1063/1.1400761.

[158] M. N. R. Ashfold, J. P. Goss, B. L. Green, P. W. May, M. E. Newton, and C. V. Peaker. Nitrogen in Diamond. *Chemical Reviews*, 120(12):5745–5794, 2020. ISSN 15206890. doi:10.1021/acs.chemrev.9b00518.

[159] M. B. Hopkins. Langmuir Probe Measurements in the Gaseous Electronics Conference RF Reference Cell. *Journal of Research of the National Institute of Standards and Technology*, 100(4):415–425, 1995.

[160] G. Cartry, L. Schiesko, C. Hopf, A. Ahmad, M. Carrère, J. M. Layet, P. Kumar, and R. Engeln. Production of negative ions on graphite surface in H_2/D_2 plasmas: Experiments and srim calculations. *Physics of Plasmas*, 19(6):063503, jun 2012. ISSN 1070-664X. doi:10.1063/1.4725188.

[161] J. Roth and C. García-Rosales. Analytic description of the chemical erosion of graphite by hydrogen ions. *Nuclear Fusion*, 36(12):1647–1659, 1996. ISSN 00295515. doi:10.1088/0029-5515/36/12/I05.

[162] A. Bogaerts and L. L. Alves. Special issue on numerical modelling of low-temperature plasmas for various applications — part II: Research papers on numerical modelling for various plasma applications. *Plasma Processes and Polymers*, 14(4-5):2016–2017, 2017. ISSN 16128869. doi:10.1002/ppap.201790041.

[163] M. J. Kushner. Hybrid modelling of low temperature plasmas for fundamental investigations and equipment design. *Journal of Physics D: Applied Physics*, 42(19):194013, 2009. ISSN 0022-3727. doi:10.1088/0022-3727/42/19/194013.

[164] I. Adamovich, S. D. Baalrud, A. Bogaerts, P. J. Bruggeman, M. Cappelli, V. Colombo, U. Czarnetzki, U. Ebert, J. G. Eden, P. Favia, D. B. Graves, S. Hamaguchi, G. Hieftje, M. Hori, I. D. Kaganovich, U. Kortshagen, M. J. Kushner, N. J. Mason, S. Mazouffre, S. Mededovic Thagard, H-R Metelmann, A. Mizuno, E. Moreau, A. B. Murphy, B A Niemira, G S Oehrlein, Z Lj Petrovic, L C Pitchford, Y-K Pu, S Rauf, O Sakai, S Samukawa, S Starikovskaia, J Tennyson, K Terashima, M M Turner, M C M van de Sanden, and A Vardelle. The 2017 Plasma Roadmap: Low temperature plasma science and technology. *Journal of Physics D: Applied Physics*, 50(32):323001, 2017. ISSN 0022-3727. doi:10.1088/1361-6463/aa76f5.

[165] M. M. Turner. Computer Simulation in Low-Temperature Plasma Physics: Future Challenges. *Plasma Processes and Polymers*, 14(1-2):1–11, 2017. ISSN 16128869. doi:10.1002/ppap.201600121.

[166] D. Vender and R. W. Boswell. Numerical Modeling of Low-Pressure RF Plasmas. *IEEE Transactions on Plasma Science*, 18(4):725–732, 1990. ISSN 19399375. doi:10.1109/27.57527.

[167] A. Sun, M. M. Becker, and D. Loffhagen. PIC/MCC simulation of capacitively coupled discharges: Effect of particle management and integration. *Computer Physics Communications*, 206:35–44, 2016. ISSN 00104655. doi:10.1016/j.cpc.2016.05.003.

[168] A. R. Gibson, Z. Donkó, L. Alelyani, L. Bischoff, G. Hübner, J. Bredin, S. Doyle, I. Korolov, K. Niemi, T. Mussenbrock, P. Hartmann, J. P. Dedrick, J. Schulze, T. Gans, and D. O'Connell. Disrupting the spatio-temporal symmetry of the electron dynamics in atmospheric pressure plasmas by voltage waveform tailoring. *Plasma Sources Science and Technology*, 28(1), jan 2019. ISSN 13616595. doi:10.1088/1361-6595/aaf535.

[169] S. W. Hwang, H. J. Lee, and H. J. Lee. Effect of electron Monte Carlo collisions on a hybrid simulation of a low-pressure capacitively coupled plasma. *Plasma Sources Science and Technology*, 23(6), 2014. ISSN 13616595. doi:10.1088/0963-0252/23/6/065040.

[170] S. H. Song and M. J. Kushner. Control of electron energy distributions and plasma characteristics of dual frequency, pulsed capacitively coupled plasmas sustained in Ar and $Ar/CF_4/O_2$. *Plasma Sources Science and Technology*, 21(5), 2012. ISSN 09630252. doi:10.1088/0963-0252/21/5/055028.

[171] A. Hurlbatt, A. R. Gibson, Sandra Schröter, Jérôme Bredin, Alexander Paul Stuart Foote, Pascaline Grondein, Deborah O'Connell, and Timo Gans. Concepts, Capabilities, and Limitations of Global Models: A Review. *Plasma Processes and Polymers*, 14(1-2):1–21, 2017. ISSN 16128869. doi:10.1002/ppap.201600138.

[172] P. Grondein, T. Lafleur, P. Chabert, and A. Aanesland. Global model of an iodine gridded plasma thruster. *Physics of Plasmas*, 23(3), 2016. ISSN 10897674. doi:10.1063/1.4944882. URL `http://dx.doi.org/10.1063/1.4944882`.

[173] S. Schröter, J. Bredin, A. R. Gibson, A. West, J. P. Dedrick, E. Wagenaars, K. Niemi, T. Gans, and D. O'Connell. The formation of atomic oxygen and hydrogen in atmospheric pressure plasmas containing humidity: Picosecond two-photon absorption laser induced fluorescence and numerical simulations. *arXiv*, 2020. ISSN 23318422.

[174] T. Body, S. Cousens, J. Kirby, and C. Corr. A volume-averaged model of nitrogen-hydrogen plasma chemistry to investigate ammonia production in a plasma-surface-interaction device. *Plasma Physics and Controlled Fusion*, 60(7), 2018. ISSN 13616587. doi:10.1088/1361-6587/aab740.

[175] O. Fukumasa, R. Italani, and S. Saeki. Numerical simulation of hydrogen ion species in the steady-state plasma of a low-pressure ion source. *Journal of Physics D: Applied Physics*, 18(12):2433–2449, 1985. ISSN 00223727. doi:10.1088/0022-3727/18/12/012.

[176] S. R. Sun, H. X. Wang, and A. Bogaerts. Chemistry reduction of complex CO_2 chemical kinetics: Application to a gliding arc plasma. *Plasma Sources Science and Technology*, 29(2), 2020. ISSN 13616595. doi:10.1088/1361-6595/ab540f.

[177] A. T. Hjartarson, E. G. Thorsteinsson, and J. T. Gudmundsson. Low pressure hydrogen discharges diluted with argon explored using a global model. *Plasma Sources Science and Technology*, 19(6), 2010. ISSN 09630252. doi:10.1088/0963-0252/19/6/065008.

[178] A. Greb, K. Niemi, D. O'Connell, G. J. Ennis, N. Macgearailt, and T. Gans. Improved fluid simulations of radio-frequency plasmas using energy dependent ion mobilities. *Physics of Plasmas*, 20(5), 2013. ISSN 1070664X. doi:10.1063/1.4804280.

[179] L. L. Alves and L. Marques. Fluid modelling of capacitively coupled radio-frequency discharges: A review. *Plasma Physics and Controlled Fusion*, 54(12), 2012. ISSN 07413335. doi:10.1088/0741-3335/54/12/124012.

[180] J. Van Dijk, G. M.W. Kroesen, and A. Bogaerts. Plasma modelling and numerical simulation. *Journal of Physics D: Applied Physics*, 42(19), 2009. ISSN 00223727. doi:10.1088/0022-3727/42/19/190301.

[181] G. Chen and L. L. Raja. Fluid modeling of electron heating in low-pressure, high-frequency capacitively coupled plasma discharges. *Journal of Applied Physics*, 96(11):6073–6081, 2004. ISSN 00218979. doi:10.1063/1.1818354.

[182] J. Van Dijk, G. M.W. Kroesen, and A. Bogaerts. Plasma modelling and numerical simulation. *Journal of Physics D: Applied Physics*, 42(19), 2009. ISSN 00223727. doi:10.1088/0022-3727/42/19/190301.

[183] D. J. Economou. Hybrid Simulation of Low Temperature Plasmas: A Brief Tutorial. *Plasma Processes and Polymers*, 14(1-2):1–16, 2017. ISSN 16128869. doi:10.1002/ppap.201600152.

[184] S. J. Doyle, A. R. Gibson, J. Flatt, T. S. Ho, R. W. Boswell, C. Charles, P. Tian, M. J. Kushner, and J. Dedrick. Spatio-temporal plasma heating mechanisms in a radio frequency electrothermal microthruster. *Plasma Sources Science and Technology*, 27(8):1–37, 2018. ISSN 13616595. doi:10.1088/1361-6595/aad79a.

[185] A. Greig, C. Charles, N. Paulin, and R. W. Boswell. Volume and surface propellant heating in an electrothermal radio-frequency plasma micro-thruster. *Applied Physics Letters*, 105(5), 2014. ISSN 00036951. doi:10.1063/1.4892656.

[186] A. R. Gibson, M. Foucher, D. Marinov, P. Chabert, T. Gans, M. J. Kushner, and J. P. Booth. The role of thermal energy accommodation and atomic recombination probabilities in low pressure oxygen plasmas. *Plasma Physics and Controlled Fusion*, 59(2), 2017. ISSN 13616587. doi:10.1088/1361-6587/59/2/024004.

[187] A. Panarese, P. Diomede, and S. Longo. Kinetic modelling of atom production and thermalization in CCRF discharges in H_2. *Plasma Sources Science and Technology*, 22(4), 2013. ISSN 09630252. doi:10.1088/0963-0252/22/4/045017.

[188] Xi Chen and E. Pfender. Effect of the Knudsen number on heat transfer to a particle immersed into a thermal plasma. *Plasma Chemistry and Plasma Processing*, 3(1):97–113, 1983. ISSN 02724324. doi:10.1007/BF00566030.

[189] W. Steckelmacher. Knudsen flow 75 years on: The current state of the art for flow of rarefied gases in tubes and systems. *Reports on Progress in Physics*, 49(10):1083–1107, 1986. ISSN 00344885. doi:10.1088/0034-4885/49/10/001.

[190] P. Diomede, S. Longo, and M. Capitelli. Negative-ion yield in low-pressure radio frequency discharges in hydrogen: Particle modeling and vibrational kinetics. *Review of Scientific Instruments*, 77(3):1–4, 2006. ISSN 00346748. doi:10.1063/1.2151891.

[191] T. Šimko, V. Martišovitš, J. Bretagne, and G. Gousset. Computer simulations of H^+ and H_3^+ transport parameters in hydrogen drift tubes. *Physical Review E*, 56(5):5908–5919, 1997. ISSN 1063-651X. doi:10.1103/physreve.56.5908.

[192] V. A. Eletskii. Handbook of Physical Quantities. In I.V. Grigoriev and E. Z. Meilikhov, editors, *Elementary processes in gases and plasmas*, pages 489 – 518. Boca Raton CRC Press, 1997.

[193] C. Gorse, R. Celiberto, M. Cacciatore, A. Laganá, and M. Capitelli. From dynamics to modeling of plasma complex systems: negative ion (H^-) sources. *Chemical Physics*, 161(1-2):211–227, 1992. ISSN 03010104. doi:10.1016/0301-0104(92)80188-2.

[194] NIST chemistry webook - Hydrogen. URL `https://webbook.nist.gov/cgi/cbook.cgi?ID=C1333740&Mask=1000#Dia118`.

[195] S. Biagi. Magboltz - transport of electrons in gas mixtures.

[196] M. Hayashi. Monte Carlo Simulation of Electron Avalanche in Hydrogen. *Le Journal de Physique Colloques*, 40(C7):C7–45–C7–46, 1979. ISSN 0449-1947. doi:10.1051/jphyscol:1979722.

[197] P. Banks. Collision frequencies and energy transfer ions. *Planetary and Space Science*, 14(11):1105–1122, 1966. ISSN 00320633. doi:10.1016/0032-0633(66)90025-0.

[198] Y. Itikawa. Effective collision frequency of electrons in atmospheric gases. *Planetary and Space Science*, 19(8):993–1007, 1971. ISSN 00320633. doi:10.1016/0032-0633(71)90149-8.

[199] Y. K. Kim and M. E. Rudd. Binary-encounter-dipole model for electron-impact ionization. *Physical Review A*, 50(5):3954–3967, 1994. ISSN 10502947. doi:10.1103/PhysRevA.50.3954.

[200] H. Ehrhardt, L. Langhans, F. Linder, and H. S. Taylor. Resonance scattering of slow electrons from H2 and CO angular distributions. *Physical Review*, 173(1):222–230, 1968. ISSN 0031899X. doi:10.1103/PhysRev.173.222.

[201] S. J. Buckman and A. V. Phelps. Vibrational excitation of D_2 by low energy electrons. *The Journal of Chemical Physics*, 82(11):4999–5011, 1985. ISSN 00219606. doi:10.1063/1.448673.

[202] R. Celiberto, R. K. Janev, V. Laporta, J. Tennyson, and J. M. Wadehra. Electron-impact vibrational excitation of vibrationally excited H_2 molecules involving the resonant 2Σg+ Rydberg-excited electronic state. *Physical Review A - Atomic, Molecular, and Optical Physics*, 88(6):1–11, 2013. ISSN 10502947. doi:10.1103/PhysRevA.88.062701.

[203] R. Celiberto, M. Capitelli, J.M. Wadehra, R.K. Janev, A. Laricchiuta, and D.E. Atems. Cross Section Data for Electron-Impact Inelastic Processes of Vibrationally Excited Molecules of Hydrogen and Its Isotopes. *Atomic Data and Nuclear Data Tables*, 77(2):161–213, 2003. ISSN 0092640X. doi:10.1006/adnd.2000.0850.

[204] I. I. Fabrikant, J. M. Wadhera, and Y. Xu. Resonance processes in e - H_2 collisions: Dissociative attachment and dissociation from vibrationally and rotationally excited states. *Physica Scripta T*, 96: 45–51, 2002. ISSN 02811847. doi:10.1238/physica.topical.096a00045.

[205] P. Diomede, K. Hassouni, S. Longo, and M. Capitelli. Self-consistent modeling of the effect of wall-neutral reactions on parallel plate radio frequency discharge plasma in pure hydrogen. *IEEE Transactions on Plasma Science*, 35(5 I):1241–1246, 2007. ISSN 00933813. doi:10.1109/TPS.2007.901899.

[206] B. Ruscic, R. E. Pinzon, M. L. Morton, G. Von Laszevski, S. J. Bittner, S. G. Nijsure, K. A. Amin, M. Minkoff, and A. F. Wagner. Introduction to active thermochemical tables: Several "Key" enthalpies of formation revisited. *Journal of Physical Chemistry A*, 108(45):9979–9997, 2004. ISSN 10895639. doi:10.1021/jp047912y.

[207] B. Ruscic, R. E. Pinzon, G. Von Laszewski, D. Kodeboyina, A. Burcat, D. Leahy, D. Montoy, and A. F. Wagner. Active Thermochemical Tables: Thermochemistry for the 21st century. *Journal of Physics: Conference Series*, 16(1):561–570, 2005. ISSN 17426596. doi:10.1088/1742-6596/16/1/078.

[208] V. A. Kadetov. *Diagnostics and modeling of an inductively coupled radio frequency discharge in hydrogen*. PhD thesis, Ruhr-Universitat Bochum, 2004.

[209] M. Abdel-Rahman, V. Schulz-Von Der Gathen, T. Gans, K. Niemi, and H. F. Döbele. Determination of the degree of dissociation in an inductively coupled hydrogen plasma using optical emission spectroscopy and laser diagnostics. *Plasma Sources Science and Technology*, 15(4):620–626, 2006. ISSN 09630252. doi:10.1088/0963-0252/15/4/005.

[210] J. Ellis, J. Branson, K. Niemi, E. Wagenaars, and T. Gans. Influence of surface materials on the volume production of negative ions in a radio-frequency driven hydrogen plasma. *Journal of Physics D: Applied Physics*, 53, 2020. ISSN 23318422.

[211] J. K. Olthoff and K. E. Greenberg. The Gaseous Electronics Conference RF Reference Cell—An Introduction. *Journal of Research of the National Institute of Standards and Technology*, 100(4):327–339, 1995. ISSN 1044677X. doi:10.6028/jres.100.025.

[212] P. Tian. *Controlling Photon and Ion Fluxes in Low Pressure Low Temperature Plasmas*. PhD thesis, University of Michigan, 2018.

[213] P. Tian and M. J. Kushner. Controlling VUV photon fluxes in low-pressure inductively coupled plasmas. *Plasma Sources Science and Technology*, 24(3):034017, 2015. ISSN 0963-0252. doi:10.1088/0963-0252/24/3/034017.

[214] Y. Takao, N. Kusaba, K. Eriguchi, and K. Ono. Two-dimensional particle-in-cell Monte Carlo simulation of a miniature inductively coupled plasma source. *Journal of Applied Physics*, 108(9), 2010. ISSN 00218979. doi:10.1063/1.3506536.

[215] L. J. Mahoney, A. E. Wendt, E. Barrios, C. J. Richards, and J. L. Shohet. Electron-density and energy distributions in a planar inductively coupled discharge. *Journal of Applied Physics*, 76(4):2041–2047, 1994. ISSN 00218979. doi:10.1063/1.357672.

[216] P. L. G. Ventzek. Two-dimensional modeling of high plasma density inductively coupled sources for materials processing. *Journal of Vacuum Science and Technology B: Microelectronics and Nanometer Structures*, 12(1):461, 1994. ISSN 0734211X. doi:10.1116/1.587101.

[217] M. J. Grapperhaus. *Multi scale transport phenomena in low-pressure plasmas*. PhD thesis, University of Illinois at Urbana-Champaign, 1998.

[218] S. Mouchtouris and G. Kokkoris. A hybrid model for low pressure inductively coupled plasmas combining a fluid model for electrons with a plasma-potential-dependent energy distribution and a fluid-Monte Carlo model for ions. *Plasma Sources Science and Technology*, 25(2), 2016. ISSN 13616595. doi:10.1088/0963-0252/25/2/025007.

[219] M. Capitelli, O. De Pascale, P. Diomede, A. Gicquel, C. Gorse, K. Hassouni, S. Longo, and D. Pagano. Twenty five years of vibrational kinetics and negative ion production in H_2 plasmas: Modelling aspects. *AIP Conference Proceedings*, 763:66–80, 2005. ISSN 0094243X. doi:10.1063/1.1908284.

[220] S. Markelj and I. Ade. Production of vibrationally excited hydrogen molecules by atom recombination on Cu and W materials. *Journal of Chemical Physics*, 134(12), 2011. ISSN 00219606. doi:10.1063/1.3569562.